Transition dans les couches limites supersoniques : simulations numériques directes et contrôle par stries

Muhittin Celep

To cite this version:

Muhittin Celep. Transition dans les couches limites supersoniques : simulations numériques directes et contrôle par stries. Fluids mechanics [physics.class-ph]. Normandie Université, 2024. English. NNT : 2024NORMIR15 . tel-04719901

HAL Id: tel-04719901
https://theses.hal.science/tel-04719901v1

Submitted on 3 Oct 2024

THÈSE

Pour obtenir le diplôme de doctorat

Spécialité **MECANIQUE DES FLUIDES, ENERGETIQUE, THERMIQUE, COMBUSTION, ACOUSTIQUE**

Préparée au sein de l'**INSA Rouen Normandie**

Transition dans les couches limites supersoniques: simulations numériques directes et contrôle par stries

Présentée et soutenue par

MUHITTIN CELEP

Thèse soutenue le 01/07/2024
devant le jury composé de :

M. ABDELLAH HADJADJ	PROFESSEUR DES UNIVERSITÉS - INSA de Rouen Normandie	Directeur de thèse
M. HUGO SAFDARI SHADLOO	MAITRE DE CONFERENCES DES UNIVERSITES HDR - INSA Rouen Normandie	Co-directeur de thèse
M. LUC VERVISCH	PROFESSEUR DES UNIVERSITÉS - INSA de Rouen Normandie	Président du jury
MME TARANEH SAYADI	CHARGE DE RECHERCHE - Institut Jean Le Rond d'Alembert	Membre
M. OLIVIER CHAZOT	PROFESSEUR - Institut von Karman de dynamique des fluides	Rapporteur
M. GUILLAUME LEHNASCH	MAITRE DE CONFERENCES DES UNIVERSITES HDR - École Nationale Supérieure de Mécanique et d'Aérotechnique	Rapporteur

Thèse dirigée par **ABDELLAH HADJADJ** (COMPLEXE DE RECHERCHE INTERPROFESSIONNEL EN AEROTHERMOCHIMIE) et **HUGO SAFDARI SHADLOO** (COMPLEXE DE RECHERCHE INTERPROFESSIONNEL EN AEROTHERMOCHIMIE)

Normandie Université

DISSERTATION

Submitted in the partial fulfillment for the award of Doctor of Philosophy

Specialized in : Mechanics and Energy

From CORIA, UMR 6614 CNRS.

Insights into Transitional Supersonic Boundary Layers: DNS Investigations and Streak Control Strategies

by

MUHİTTİN CELEP

Thesis defended publicly on the 1^{st} July, 2024
in front of the jury comprising of:

Olivier CHAZOT	Professor, The von Karman Institute for Fluid Dynamics	Reviewer
Guillaume LEHNASCH	Associate Professor HDR, ISAE-ENSMA	Reviewer
Taraneh SAYADI	Researcher, Jean le Rond ∂'Alembert Institute	Examiner
Luc VERVISCH	Professor, INSA of Rouen	Examiner
Markus KLOKER	Associate Professor, University of Stuttgart	Invited examiner
Mostafa S. SHADLOO	Associate Professor HDR, INSA of Rouen	Co-supervisor
Abdellah HADJADJ	Professor, INSA of Rouen	Supervisor

Supervised by Prof. Abdellah HADJADJ
Co-supervised by Dr. Mostafa Safdari SHADLOO
TASC Department, CORIA Laboratory UMR-6614, CNRS

INSA INSTITUT NATIONAL DES SCIENCES APPLIQUÉES ROUEN NORMANDIE

ED 591 PSIME

UMR 6614 CORIA COMPLEXE DE RECHERCHE INTERPROFESSIONNEL EN AEROTHERMOCHIMIE

Abstract

In high-speed flows, elevated viscous drag and thermal loads are inherent outcomes over aerodynamic bodies. These effects escalate substantially during the transition phase when the boundary layer becomes turbulent. To mitigate potential mechanical damage and fatigue-related failures, thermal protection systems are integrated into vehicles, adding complexity to the technical and economic aspects of design. The solution lies in gaining a comprehensive understanding of transition mechanisms and developing control systems to prolong laminar boundary layer along the vehicle's surface. Numerous active and passive control techniques can be employed for transition control, with the streak employment method emerging as a particularly promising approach. This method involves generating narrowly spaced streaks in the spanwise direction, creating alternating high and low-speed regions in the flow field. Although the method has only recently been tested in supersonic flows, demonstrating its effectiveness in delaying transition, its suitability needs to be assessed further. In this research work, direct numerical simulations are performed in supersonic and near-hypersonic regimes. Streaks are introduced through a blowing/suction strip placed at the wall prior to that of the perturbation which is used to trigger transition in a "controlled" fashion, forced by a single frequency and wavenumber disturbance. The investigation at Mach 2.0 confirms that streaks with five times the fundamental wavenumber are most beneficial for transition control. Additionally, cooling enhances the method's effectiveness, while heating severely deteriorates the capability of control streaks. The isothermal wall condition does not alter the comparable stabilizing impact of the mean flow deformation (MFD) and the 3-D part of the control at Mach 2.0. However, at Mach 4.5, both the type of instability and the characteristics of the streaks change significantly. The stabilizing impact of the MFD becomes nearly absent, and the 3-D part of the control predominates, with the characteristics of the streaks no longer considered independent of their initial disturbance amplitude.

Keywords:

Boundary layer instabilities, Direct numerical simulation, Laminar breakdown, Linear stability analysis, Stanton number, Supersonic boundary layer, Reynolds analogy, Transition, Transition control, Streak employment.

Résumé

Dans les écoulements à haute vitesse, une traînée visqueuse élevée et des charges thermiques importantes sont des conséquences inhérentes sur les corps aérodynamiques. Ces effets augmentent de manière significative pendant la phase de transition lorsque la couche limite devient turbulente. Afin de réduire les risques de dommages mécaniques et de défaillances liées à la fatigue, des systèmes de protection thermique sont intégrés aux véhicules, ajoutant de la complexité aux aspects techniques et économiques de la conception. La solution réside dans l'acquisition d'une compréhension approfondie des mécanismes de transition et le développement de systèmes de contrôle pour prolonger la couche limite laminaire le long de la surface du véhicule. De nombreuses techniques de contrôle actives et passives peuvent être utilisées pour le contrôle de la transition, parmi lesquelles la méthode de l'emploi de stries émerge comme une approche particulièrement prometteuse. Cette méthode consiste à générer des stries étroitement espacées dans la direction de l'envergure, créant des zones alternées de haute et basse vitesse dans le champ d'écoulement. Bien que la méthode ait été testée récemment dans des écoulements supersoniques, démontrant son efficacité pour retarder la transition, sa pertinence doit être évaluée plus avant. Dans ce travail de recherche, des cas de DNS sont réalisés dans des régimes supersoniques et près-hypersoniques. Les stries sont introduites à l'aide d'une bande de soufflage/aspiration placée sur la paroi avant celle de la perturbation qui est utilisée pour déclencher la transition de manière "contrôlée", forcée par une perturbation à une seule fréquence et longueur d'onde. L'enquête à Mach 2.0 confirme que les stries avec cinq fois la longueur d'onde fondamentale sont les plus bénéfiques pour le contrôle de la transition. De plus, le refroidissement améliore l'efficacité de la méthode, tandis que le chauffage détériore considérablement la capacité de contrôle des stries. La condition murale isotherme n'altère pas l'impact stabilisateur comparable de la déformation du flux moyen (DFM) et de la partie 3D du contrôle à Mach 2.0. Cependant, à Mach 4.5, tant le type d'instabilité que les caractéristiques des stries changent de manière significative. L'impact stabilisateur de la DFM devient presque absent, et la partie 3D du contrôle prédomine, les caractéristiques des stries n'étant plus considérées comme indépendantes de leur amplitude de perturbation initiale.

Mots clés:

Analogie de Reynolds, Analyse de stabilité linéaire, Couche limite supersonique, Contrôle de transition, Dégradation laminaire, Emploi de stries, Nombre de Stanton, Instabilités de couche limite, Simulation numérique directe, Transition.

Acknowledgements

With the happiness of reaching this page, I can finally write without the need for giving references. There is a lot to say, but I will try not to be too lavish and add a maximum of two pages to my manuscript. My Ph.D. started a bit rocky; however, my supervisors, Abdellah and Mostafa, were always there to look after me, which helped me to put everything back on track. Their engineering-minded approach to overcoming hindrances thought me important lessons. Entering the field as a rookie, the discussions I had with them increased my understanding of the numerical world and my capacity to elaborate on mathematical grounds. Meanwhile, my informal supervisor Markus has been an immense help for me in laying a foundation of transition mechanisms in my mind through all our insightful discussions. Working with him made me realize how ignorant I was about the literal meaning of the words “elaboration” and “diligence”. For all this and his resilience to my everlasting (still have some) questions, I am uttermost grateful.

Seneler boyunca, imkanlarım ölçüsünde, farklı ülkelerde yaşama fırsatı buldum ve gittiğim her yerde pek çok insanla tanışma imkanı edindim. Türkiye’de yaşayan ve çocukluğumu birlikte geçirdiğim kardeşlerim Pıtır, Seco ve Şişko, hayatımın yarısından fazlasında benimle birliktelerdi ve bana adeta bir aile gibi oldular. Bununla birlikte, aynı dönemde tanışmış olsak da, samimiyetimizin üniversite zamanlarında arttığı Kumru ve Okaço’nun da yeri benim için çok ayrıdır. Hayatımın geneli ve bu önemli dönüm noktasında bana verdikleri sınırsız destek için onlara minnettarım.

Insa and this lovely (yes, contrary to counter-opinions) city of Rouen have been places with a high circulation, allowing me to meet some cool people. Vivre en colocation dans un autre pays a été une expérience enrichissante. C’était comme s’immerger dans la culture française et être bombardé par chaque coloc pour les differents aspects. J’apprécie vraiment leur patience, particulièrement celle de Julien, avec mes compétences en français qui s’améliorent à un rythme d’escargot, ce qui a apporté des souvenirs mémorables mais inappropriés à mentionner ici. Both the working place and the daily life would not have been as enjoyable without the presence of my folks Rezvan (I am still traumatized by the one-day-round-trip in Germany), Skylar, Chethan, Raji, Anand, Matthieu, Laure, Claudius, and all the others who stopped by at INSA some time in their lives. I will miss our gatherings, explorations of Rouen’s bar and restaurants, as well as our thought-provoking discussions. The last year of my Ph.D. was particularly exciting (maybe not so much for Abdellah and Mostafa) given that the provisional defense date gradually shifted from December to July every month. During this time, I also started bouldering, for which I now feel a bit resentful that I resisted for so long, as I enjoyed it enormously after joining the small team in the lab.

Outside the city, my life has been encoloured by the small Poitiers’ gang of KsKo with controversial perspectives, BBC Gabi with all the gossips, Gi Bao with his head spread all around the world by now, Mama’s boy Ciccio and smasher-chef Haffner. It was a great idea to gather at different places every once in a while. I appreciate each meeting and looking forward to the next one.

Son olarak, hayatlarının en güzel yıllarında beni büyük bir özveriyle yetiştiren ve en zor zamanlarımda hep yanımda olan annem ve babama sonsuz teşekkür ederim.

Contents

Symbols

A	Disturbance amplitude
a	Speed of sound (m/s)
C	Chapman-Rubesin parameter
c_r	Phase speed of disturbance (m/s)
c_g	Group velocity (m/s)
C_h	Stanton number
C_f	Skin-friction coefficient
C_p	Specific heat capacity at constant pressure $(J/kg.K^{-1})$
E	Total energy (m^2/s^2)
f	Frequency (Hz)
f_s	Sampling frequency (Hz)
f_t	Flow through time (s)
h	Integer multiple of frequency
k	Integer multiple of wavenumber
H	Shape factor
$\mathcal{H}$	Enthalpy (m^2/s^2)
L_x, L_y, L_z	Domain lengths in the cartesian coordinate (m)
M	Mach number
$\dot{m}$	Transverse mass flux $(kg/m^2.s^{-1})$
N_x, N_y, N_z	Number of nodes in the cartesian coordinate
N	Integrated growth rate
Pr	Prandtl number
p	Static pressure (Pa)
$\dot{q}$	Heat diffusion flux (W/m^2)
R	Radius (m)
$\mathcal{R}$	Gas constant for air $(J/kg.K^{-1})$
Re	Reynolds number
Re_u	Unit Reynolds number $(1/m)$

R_q	Heating/cooling rate
r	Recovery factor
T	Temperature (K)
t	Time (s)
u, v, w	Velocity components (m/s)
U	Velocity magnitude (m/s)
w_c	Streamwise width of the control strip (m)
x, y, z	Cartesian coordinates (m)

Greeks

α	Complex eigenvalue: $\alpha_r + i\alpha_i$
α_r	Streamwise wavenumber ($1/m$)
α_i	Spatial growth rate of disturbance ($1/m$)
β	Spanwise wavenumber ($1/m$)
γ	Heat capacity ratio
Δt	Time step (s)
$\Delta x, \Delta y, \Delta z$	grid spacing (m)
δ	Boundary-layer thickness (m)
$\delta^\star$	Displacement thickness (m)
δ_{ij}	Kronecker symbol
ϵ	Small number
η	Similarity parameter
Θ	Phase angle (°)
θ	Momentum thickness (m)
κ	Grid stretching parameter
λ	Disturbance wavelength (m) and thermal conductivity ($W/m.K^{-1}$)
μ	Dynamic viscosity ($kg/m.s^{-1}$)
ν	Kinematic viscosity (m^2/s)
ρ	Density (kg/m^3)
τ	Viscous stress tensor
Ψ	Wave angle (°)
ω	Angular frequency (rad/s)
$\omega_x, \omega_y, \omega_z$	Vorticity in the cartesian coordinate (Hz)

Subscripts

0	fundamental value for disturbances
1	beginning

2	end
aw	adiabatic value
c	control
$crit$	critical
eq	equidistant
in	inlet value
i, j, k	Einstein notation, i: streamwise, j: wall-normal and k: spanwise direction
max	maximum value
min	minimum value
ob	oblique breakdown
out	outlet value
r, ref	reference value
rec	value at recovery condition
str	stretched
w	wall value
δ_e, e	boundary-layer edge value
η	value at self-similar coordinate
∞	freestream flow variable
τ	friction variable

Superscripts

$^{+}$	wall-units normalized variable
*	nondimensional variable

Operators

$\boldsymbol{\varphi}$	vector notation
$\overline{\varphi}$	time and spatial averaging quantity
φ'	disturbance quantity
φ''	Favre fluctuation
$\widetilde{\varphi}$	Favre averaging quantity
$\widehat{\varphi}$	Fourier transform quantity

Abbreviations

2-D	Two Dimensional
3-D	Three Dimensional
BL	Boundary Layer
CFL	Courant-Friedrichs-Lewy

CHOC-WAVES	Compressible High-Order Code using Weno Adaptive Stencils
CO_2	Carbon-dioxide
DNS	Direct Numerical Simulations
DRP	Dispersion-Relation-Preserving
ENO	Essentially Non-Oscillatory
EVP	Eigenvalue Problem
FFT	Fast Fourier Transformation
FPG	Favorable-Pressure-Gradient
GIP	Generalized Inflection Point
GRA	Generalized Reynolds Analogy
HDF	Hierarchical Data Format
HIFiRE	Hypersonic International Flight Research Experimentation
IBM	Immersed Boundary Method
ICAO	International Civil Aviation Organization
ICCT	International Council on Clean Transportation
IO	Input/Output
LES	Large-Eddy Simulations
LF	Lax-Friedrichs
LSA	Linear Stability Analysis
LST	Linear Stability Theory
MBF	Modified-Base-Flow
MFD	Mean-Flow-Deformation
MPI/OMP	Message Passing Interface/Open Multi-Processing
NASA	National Aeronautics and Space Administration
NS	Navier Stokes
NSE	Navier Stokes Equations
OB	Oblique Breakdown
PSE	Parabolized Stability Equations
RANS	Reynolds Averaged Navier Stokes
RD	Renard-Deck
RK	Runge Kutta
SAF	Sustainable Aviation Fuels
SST	Supersonic Transport
TS	Tollmien-Schlichting
TVD	Total-Variation-Diminishing
WENO	Weighted-Essentially Non-Oscillatory
ZPG	Zero-Pressure Gradient

List of Figures

List of Tables

Chapter 1

Introduction

Contents

A supersonic transport (SST) or a supersonic airliner is a civilian supersonic aircraft designed to transport passengers at speeds greater than the speed of sound. To date, the only SSTs to see regular service have been Concorde and the Tupolev Tu-144. The last passenger flight of the Tu-144 and Concorde was in June 1978 and Octover 2003, respectively. Following the permanent cessation of flying by Concorde, there are no remaining SSTs in commercial service.

However, the desire for a second-generation supersonic aircraft has remained within the aviation industry, following nearly 60 years of advancement in aerodynamics, material science and propulsion systems. Eventually, a half a dozen ongoing concepts have emerged since the retirement of Concorde. In March 2016, Boom Technology revealed a 40-passenger supersonic jet flying at Mach 1.7, claiming to be flying quiter than Concorde (Vance, 2016). It is planned to go into service in 2029 with 130 pre-orders (Scanlan, 2024). Spike Aeropsace presented an SST design of 18 passengers named Spike S-512 aiming to cruise at Mach 1.6 (Supersonic transport, 2024). In June 2019, Lockheed Martin unveiled the Quiet Supersonic Technology Airliner, a Mach 1.8, transpacific airliner concept for 40 passenger (Risen, 2019). In 2019, Exosonic was created with the goal of developing a 70-passenger supersonic jet capable of flying Mach 1.8 and with a range of 9,300 km. The company aims to introduce the jet commercially in the 2030s (Exosonic, 2024). Also, in August 2020, a twinjet delta wing aircraft that can accommodate 19 passengers and fly at Mach 3.0 has been unveiled by Virgin Galactic and Rolls-Royce (Gohd, 2020). Moreover, the partnership between Boeing, Northrop Grumman and National Aeronautics and Space Administration (NASA) works on concepts capable of flying at Mach 4 (Newbacher, 2023).

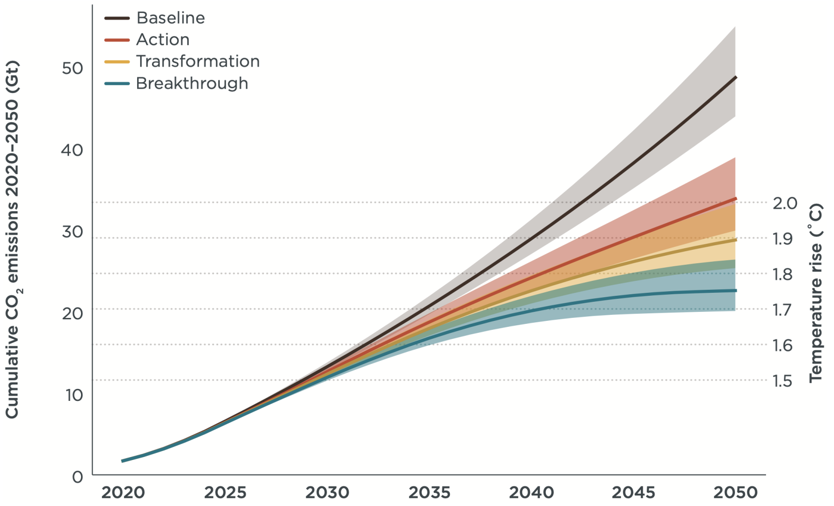

Figure 1.1: Well-to-wake global aviation CO_2 emissions by scenario and traffic forecast, 2020-2050 (Graver et al., 2022).

Noise generated by the sonic boom is considered to be the major problem, currently prohibiting commercial airplanes from flying at supersonic speeds above the lands governed by the United States due to negative impacts on the humans and animal populations (Aeronautics and Administration, 2018). However, another challenge for the SST comes due to environmental concerns, leading delegates from 196 countries to gather in Paris to sign an agreement with the objective of limiting anthropogenic global warming to below 2°C, with a preferred target of 1.5°C, compared to pre-industrial levels in 2015 (United Nations Climate Change, 2024). Various industry associations and governments have come up with technology roadmaps to assess the feasibility of achieving carbon neutrality in different industrial sectors by the middle of this century. Transportation, which accounts for one-quarter of the global carbon dioxide (CO_2) worldwide emissions, had also its share from the agreement (Scanlan, 2023). Commercial aviation was found to be the second major contributor to the transportation-related emission with around 12% after road travel constituting of three-quarter (Ritchie, 2020). According to (Graver et al., 2020), commercial airlines released approximately 920 million tonnes of carbon dioxide into the atmosphere in 2019, equivalent to the combined emissions of the German and Dutch economies (Crippa et al., 2019). Meanwhile, International Civil Aviation Organization (ICAO) (Graver et al., 2022) analyzed three decarbonization scenarios for the commercial aviation, involving six primary parameters: traffic, aircraft technology, operations, zero-emission planes, sustainable aviation fuels (SAF), and economic incentives. Figure 1.1 represents the carbon emission of the aviation sector for different scenarios in terms of the level of intervention to curb the emissions where the baseline stands for the continuation of the status quo, whereas the breakthrough adopts the most aggressive approach for achieving complete zero-carbon sector by 2050. The analysis further indicated that the relative share by the previously stated six parameters remain similar regardless of the investigated scenario. In all three scenarios, SAF accounts for the largest share of CO_2 reduction potential, varying between 59% and 64%. On the other hand, improvements in aircraft technical and operational efficiency contribute an additional one-third of CO_2 mitigation, or approximately 16% each. While SAF targets the chemical composition of the fuel, the technical and operational efficiency aim at reducing the fuel consumption.

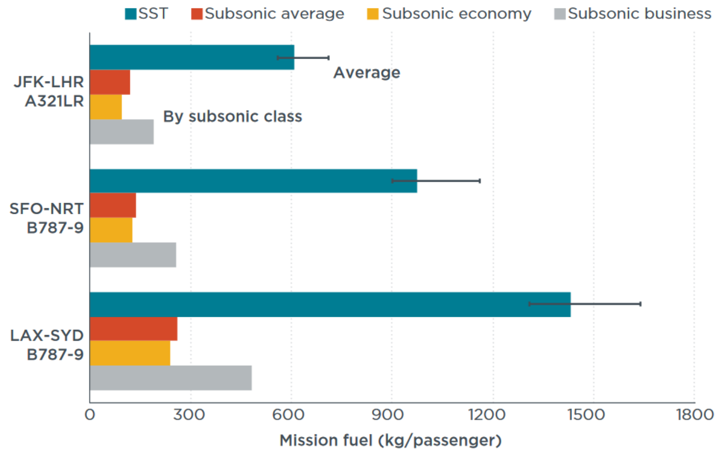

Figure 1.2: One-way mission fuel consumption per passenger by route and class (Kharina et al., 2018).

Regarding the feasibility of SSTs in the market, an analysis by the International Council on Clean Transportation (ICCT) estimates that a SST would burn 5 to 7 times as much fuel per passenger (Kharina et al., 2018). As depicted in figure 1.2, a supersonic flight from New York to London would require over double the fuel consumption per passenger compared to subsonic business-class, six times more than economy class, and three times more than subsonic business for a flight from Los Angeles to Sydney. Given these findings and the stringent regulations imposed by aviation authorities, the prospects for SSTs to achieve operational viability appear challenging.

In high-speed flows, aerodynamic bodies are naturally subjected to high viscous drag, which become more severe when the flow transits from laminar to turbulent regime (Anderson, 2000). The transition gives rise to the skin-friction coefficient *i.e.* up to one order

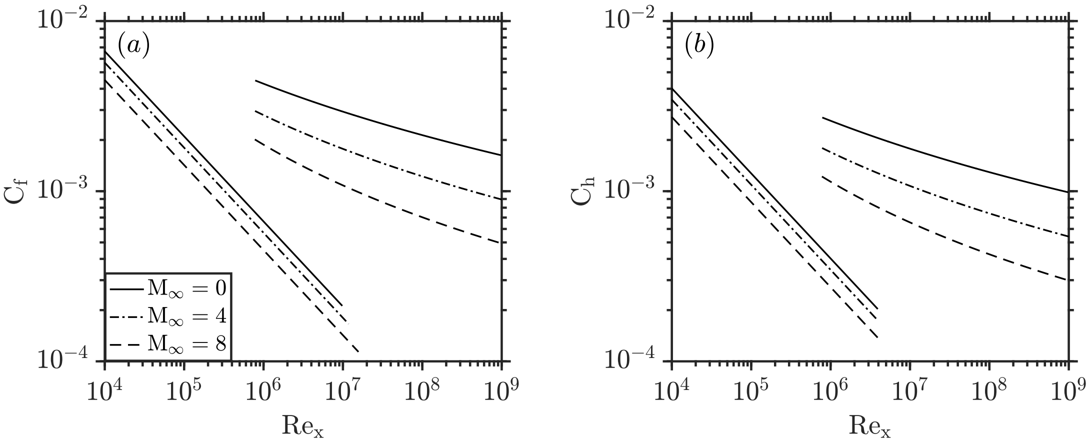

Figure 1.3: Theoretical (a) skin-friction coefficient and (b) Stanton number for adiabatic flow (White and Corfield, 2006).

higher depending on the transition onset location as indicated in fig. 1.3. This increased skin-friction coefficient causes high viscous drag and leads to higher fuel consumption. Additionally, as the Mach number increases, aerodynamic heating, arising from the kinetic energy dissipating and transforming into internal energy near the surface of the vehicle becomes significant. The resulting thermal load may cause significant mechanical damage and possible fatigue-related failures. To prevent such impacts, thermal protection systems must be integrated into the vehicle's design, which can pose technical and economic complications (Malik, 2003). To mitigate all these potential risks as well as to lower the fuel consumption, increase the payload, and the flight range, maintaining the laminar flow around the vehicle is crucial. Transition control, which involves managing the transition of the boundary layer from laminar to turbulent flow along the vehicle's surface, emerges as a promising approach targeting the aforementioned technical improvement for reducing the emissions. For a conceptual hypersonic vehicle, the contribution of the viscous boundary layer to the total drag accounts for 30% in fully turbulent flow, while it is only around 10% in fully laminar flow (Reed et al., 1997). It is also stated that retaining a fully laminar boundary layer on an aircraft, designed for a single-stage-to-orbit mission, would allow carrying double the payload-to-gross-weight compared to the fully turbulent scenario (Whitehead, 1989). The present discussion has evolved around supersonic/near-hypersonic applications. However, it should also be reminded that any improvement in flow control systems might also be integrated to other applications such as fighter jets, missiles, and re-entry vehicles.

1.1 Transition

Transition is a process of a laminar, including regular and traceable structures, flow becoming turbulent, statistically coherent, and chaotic structures. The phenomenon that carries a vital importance has been investigated by researchers and engineers for over a century as it poses fundamental challenges in engineering applications *i.e.* flow separation in nozzles, long-distance fuel transportation, lift/drag optimization of airfoil, modeling blood flow in veins for medical practices.

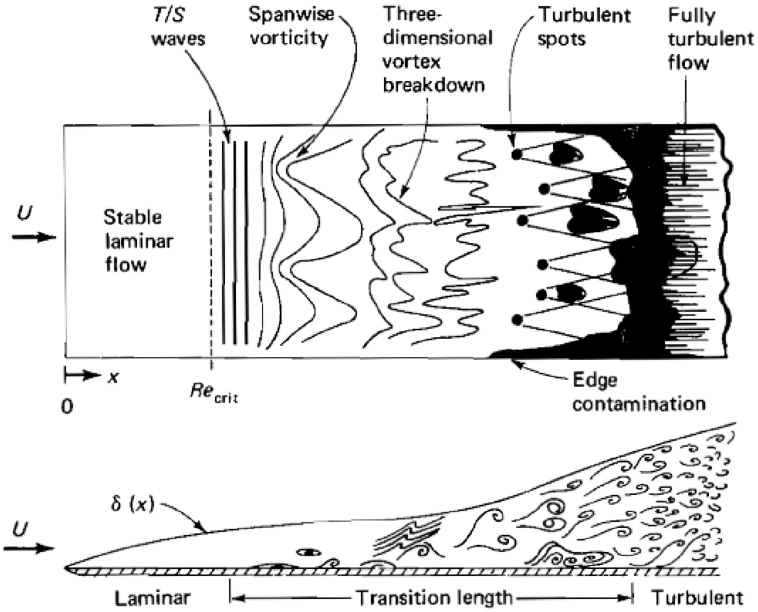

Figure 1.4: Boundary layer transition over a flat plate (White and Corfield, 2006).

Figure 1.4 illustrates the successive stages of flow transition over a smooth surface with relatively low initial perturbations. Low-amplitude sinusoidal waves form in the wake of the stable laminar flow once a threshold Reynolds number is achieved. Then, the amplification of two-dimensional (2-D) waves results in generating three-dimensional (3-D) unstable waves and hairpin eddies which break down in the vicinity of the shear layer. The interaction of the shear layer and the mean flow results in three-dimensional random fluctuations that are followed by turbulent spots. The coalescence of these spots ends up generating a fully-turbulent flow.

In nature, one often encounters transition scenarios that involve the simultaneous appearance of various types of instabilities. There exist numerous parameters influencing their occurrence and evolution such as sweep angle, wall curvature, roughness, and initial conditions (Saric et al., 2002). The geometries are usually not as simple as in the fundamental studies and free-stream conditions differ drastically from the on-ground experimental facilities. Despite all these complications, years of research have revealed the underlying physics of several instabilities and identified certain paths to transition. Some of the reviews, presenting the historical evolution of the research in this field, have been given by Reshotko (1976); Reed and Saric (1989); Kachanov (1994); Saric et al. (2002, 2003); Fedorov (2011); Lee and Jiang (2019).

1.1.1 Paths to transition

Prior to analyzing the possible paths to turbulence, instabilities that are categorized, based on the local stability problem, in two classes should be distinguished, see Huerre and Monkewitz (1985). Absolute instability is defined as a disturbance that grows in amplitude in time, spreading to the entire domain both in $x \to \infty$ and $x \to -\infty$. The instability does not leave the domain as the group velocity of the disturbances, $c_g \leq 0$. Convective instabilities, where $c_g > 0$, on the other hand, leave the domain for $t \to \infty$ following the initial disturbance, the level of which leads to various transition paths. The current study deals only with the convective instabilities in 2-D boundary layers over flat plates.

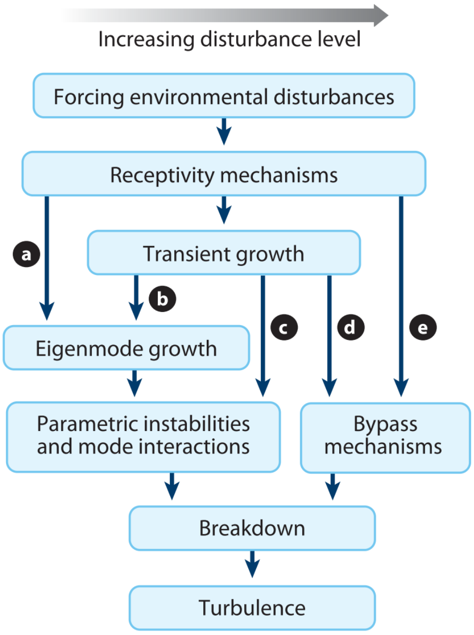

Figure 1.5: A road map of boundary layer transition (Morkovin, 1994; Fedorov, 2011).

A schematic showing the potential roads to transition induced by convective instabilities is given by Morkovin (1994) and Fedorov (2011) in fig. 1.5. The first step which takes place close to the leading edge is called receptivity by Morkovin (1969). It is a step in which internal/external disturbances enter the laminar flow and excite its eigenmodes which grow exponentially due to linear processes for small disturbances. Primary instability is the most unstable of these modes (disturbances) leading to secondary instabilities which are followed by laminar breakdown as represented in paths (a) and (b). Depending on the amplitude of the disturbances transient growth may either contribute to the transition process, path (b), or lead directly to secondary instabilities as in path (c), or result in by-pass transition by surpassing the linear and weakly non-linear stages as in path (d). Transient growth is an algebraic disturbance growth followed by an exponential decay, in other words where the dampening of small disturbances is estimated based on linear stability theory (LST), arising due to the non-normality of the linearized *Navier-Stokes* (NS) operator (Schmid and Henningson, 2001). In the presence of large disturbances, the flow instantly breaks down by bypassing the linear stages and forms localized turbulent spots as in path (e).

1.1.2 Instabilities

Rayleigh (1880) was the first one emphasizing the evolution of small but regular oscillations that are formed and travel in laminar boundary layers. Orr (1907) and Sommerfield (1908) independently derived an equation governing the amplitude growth of a perturbation mode by introducing a two-dimensional sinusoidal-shaped perturbation to incompressible NS equations. Later on, Tollmien solved this equation, which is later referred to as the Orr-Sommerfeld equation, whereas Schlichting calculated the amplification of the most unstable frequencies. However, the theory was discredited until the experimental findings of Schubauer and Skramstad (1947) where they demonstrated sinusoidal waves, later called Tollmien-Schlichting (TS) waves, constitute the first stage of the transition process. These successive accomplishments have proven the use of linear stability theory in which small sinusoidal disturbances are imposed to a given steady laminar flow to obtain the range of unstable frequencies. Lees and Lin (1946) extended the theory to compressible flows where the amplified disturbance is an equivalent of TS waves in incompressible flows. According to Mack (1969)'s terminology, these waves belong to the first-mode instabilities in compressible flows.

In compressible flows for about $M_\infty > 0.7$, the most-amplified waves become three-dimensional running obliquely ($\Psi \neq 0$) with respect to free-stream while they are two-dimensional in incompressible flows. Figure 1.6 illustrates the viscous and inviscid nature of boundary layer instability in compressible flows. (Lees and Lin, 1946) demonstrated that a necessary condition for the presence of an amplified inviscid disturbance is the presence of the generalized inflection point (GIP), which is

$$\frac{\partial}{\partial y}\left(\rho\frac{\partial u}{\partial y}\right) = 0, \quad \text{for} \quad y > y_{crit} \tag{1.1}$$

y_{crit} is the point where the non-dimensional velocity is equal to the slow acoustic wave, *i.e.* $U^* = 1 - 1/M_\infty$[1]. A compressible boundary layer is naturally susceptible to inviscid disturbances because the inflection point is always present in case of an insulated wall for $M_\infty \gtrapprox 1.6$ (Malik, 1989). When boundary layer is cooled sufficiently, which stabilizes the first mode (Lees, 1947), a second generalized inflection point for $U^* < 1 - 1/M_\infty$ appears. As cooling increases, these two existing inflectional points become closer, end up on top of each other, and then disappear by indicating a complete stabilization (Unnikrishnan and Gaitonde, 2019).

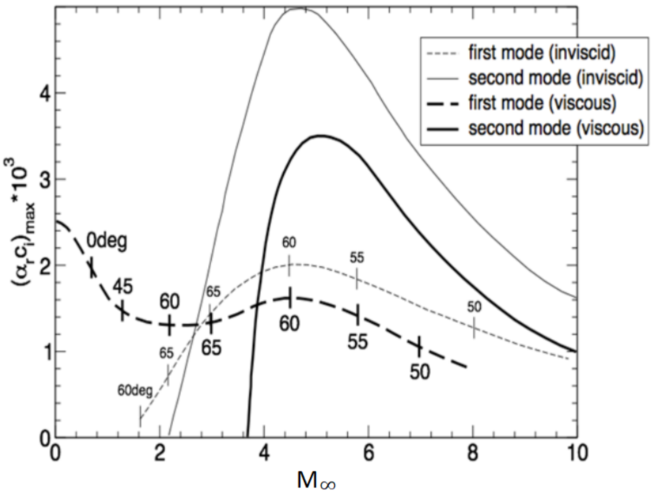

Figure 1.6: Dependence of maximum disturbance growth rate on Mach number for flat-plate flow. Influence of viscosity on the growth rate (Kloker, 2018).

Using the LST, Mack (1969) discovered the existence of higher modes appearing in supersonic boundary layers. His results showed that there is an infinite number of unstable inviscid modes (wavenumbers) so long as there is a region of supersonic mean flow relative to the phase speed, *i.e.* $\overline{M} = (u(y) - c_r)/a > 1$ where $u(y)$ is the mean-flow profile, c_r is the disturbance phase speed, and a is the local speed of sound. These instabilities, also known as the Mack modes, are of acoustic nature [2] [3], are trapped between the wall and the sonic line where the relative Mach number is supersonic, see fig. 1.7. The first of these modes is the second mode, which is the most amplified of the higher modes with $\Psi = 0$, see fig. 1.8b. One of the physical implications of the second mode is the scaling of the most amplified frequency with the local-boundary-layer thickness as $f \approx u_\infty/2\delta$, *i.e.* $\lambda \approx 2\delta$ (Stetson et al., 1989). Besides, contrary to the first-mode instabilities, the second mode is strongly destabilized with complete wall cooling, see fig. 1.8a. The reader is referred to Mack (1984) for an extensive analysis of linear stability theory for flat-plate boundary layers.

---

[1] $U = u_\infty - a_\infty$

[2] $c_r < u - a$: sound waves propagation to free-stream

[3] $c_r > u + a$: sound waves propagation to wall

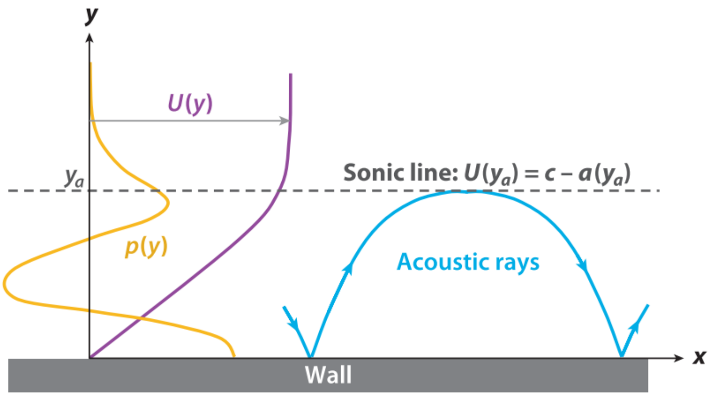

Figure 1.7: Acoustic mode in a high-speed boundary layer, where $u(y)$ is the mean-flow profile, and $p(y)$ is the pressure disturbance profile (Fedorov, 2011).

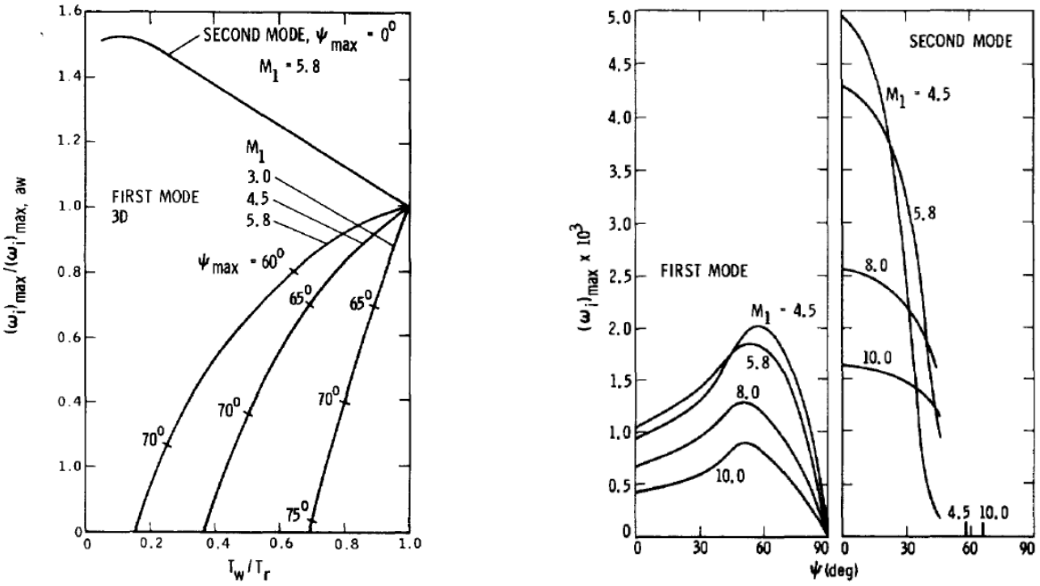

(a) Effect of wall cooling.

(b) Effect of wave angle (Ψ).

Figure 1.8: Evolution of the first- and second-mode instabilities (Mack, 1984).

1.1.3 Flat-plate laminar breakdown

For transition in an environment with a disturbance level low enough to exclude paths (c), (d), and (e), primary-instability modes are superseded by secondary instabilities, corresponding to the weakly non-linear stage in the road map. This stage of the transition process is characterized by the appearance of Λ-shaped vortices located near the boundary layer edge. In the fundamental breakdown, the secondary instability waves having the identical streamwise wavenumber as the primary waves form Λ-shaped vortices aligned in the spanwise direction, see fig. 1.9a. This scenario is called as K-type transition attributed to the findings of Klebanoff et al. (1962). If the secondary instability wave carries two times the streamwise wavelength of the primary waves, exhibiting staggered patterns as shown in fig. 1.9b, the mechanism is referred to as H- Herbert (1988) or N-type (**N**ovosibirsk) breakdown (Kachanov and Levchenko, 1984). In a special case of subharmonic resonance, the resonance wave interaction can still exist for a disturbance amplitude, $A \to 0$, if the wave speeds of the 2-D and 3-D disturbances perfectly match, leading to an optimal energy exchange *i.e* C-type breakdown after Craik (1971).

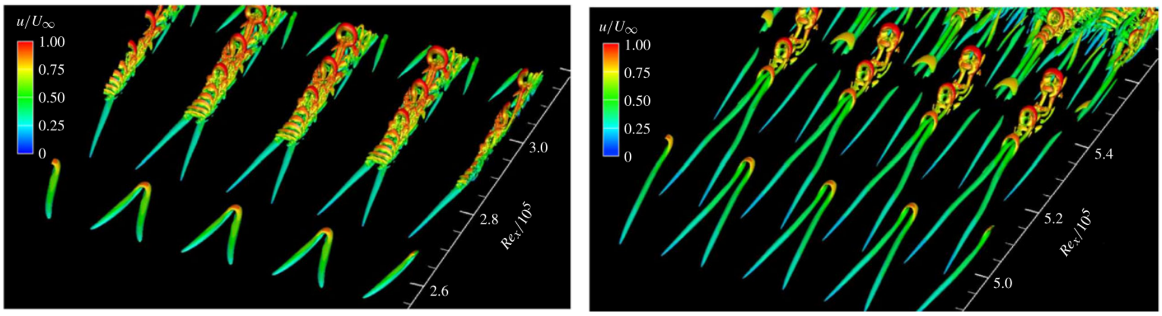

(a) K-type, $Re_x = 2.5 - 3.2 \times 10^5$ (b) H-type, $Re_x = 4.9 - 5.5 \times 10^5$

Figure 1.9: Isosurfaces of Q invariant in an instantaneous flow field, showing Λ vortices and formation of hairpin, Ω and ring-like vortices towards laminar breakdown (Sayadi et al., 2013).

For a supersonic boundary layer at Mach number 1.6, Direct Numerical Simulations (DNS) studies by Thumm (1991) and Fasel et al. (1993) were the first illustrating that the transition is controlled by oblique breakdown (OB) which is initiated by a pair of most-amplified waves traveling at identical but opposite wave angles with respect to the free-stream. Upon their amplification, their self-nonlinear interaction generates a steady vortex mode that has a double spanwise wavenumber of the oblique disturbance pair, which closes the wave-vortex triad in the spectral space (Craik, 1971). Further downstream, higher harmonic modes are generated by the non-linear interaction of the already existing modes, extending the energy exchange mechanism to a more complex stage (Bestek et al., 1994). Rather than Λ shape vortices with fundamental and subharmonic frequencies, the formation of a typical honeycomb-like structure has been demonstrated as illustrated in fig. 1.10, see (Bestek et al., 1994). A following study by Fezer and Kloker (2000) elaborated on the breakdown mechanism in the presence of the three-dimensional subharmonic modes. They found that the transition process is accelerated by the presence of subharmonic modes. However, the oblique wave pair is more likely to lead the flow to breakdown considering its larger growth rate and required lower initial amplitude. These findings were further supported by the DNS study by Husmeier et al. (2005), where the oblique breakdown was reported to be the most viable path to transition at Mach 3.0. It was indicated that the two-dimensional disturbance requires an amplitude of about 10% of the free-stream velocity to lead a classical K-type (Klebanoff et al., 1962) fundamental resonance whilst no trace of subharmonic resonance (Herbert, 1988) was observed. The experimental proof of the oblique breakdown mechanism was revealed so far as Mayer, Wernz and Fasel (2011) performed DNS calculations by replicating the experimental setup of Kosinov et al. (1994) and Ermolaev et al. (1996). The signature of the oblique breakdown was clearly demonstrated which was not reported in the 90s when the experiments were conducted. Instead, researchers concentrated mainly on a breakdown mechanism that they referred to as asymmetric subharmonic resonance which is formed by the interaction of a oblique instability wave pair and two oblique asymmetric waves, *i.e.* carrying different wave angles, with half a frequency of the former. However, Mayer, Wernz and Fasel (2011) also conjectured that a certain phase relation between input disturbances may also hinder the oblique breakdown and bring out the resonance triads. In a following study which includes the late non-linear regime of a flow field prior to the breakdown, Mayer, Von Terzi and Fasel (2011) also demonstrated that oblique breakdown can lead to a fully turbulent flow.

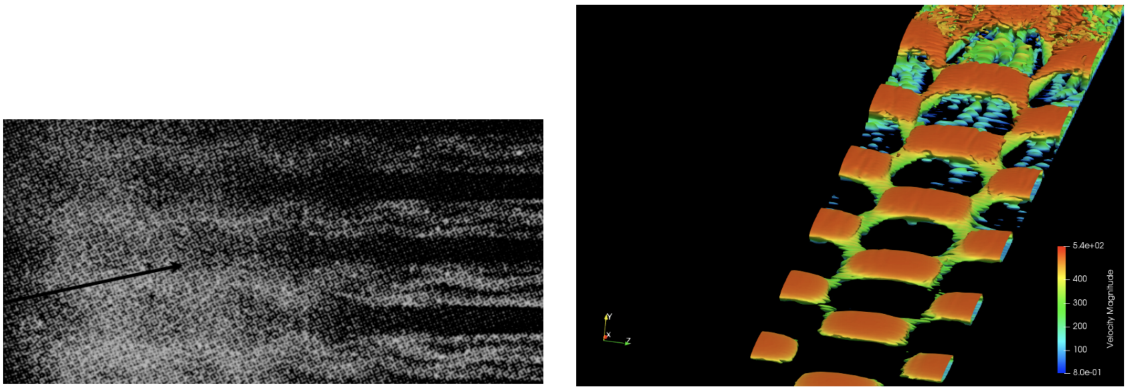

Figure 1.10: (a) O-type transition in an experimental study (Wiegel, 1997) and (b) a DNS analysis (Sharma, 2019).

In most of the aforementioned studies, numerical investigations dealt with a forced transition scenario at a single frequency and wavenumber while transition in a natural environment would be affected strongly by broadband internal/external disturbances. Taking this into consideration, Laible and Fasel (2016) and Chang and Malik (1994) have shown that a wider spectrum of disturbances results in an earlier breakdown in a laminar supersonic flow. The former also investigated the feeding mechanism of the disturbances by means of temporal DNS. They identified a continuous transient growth mechanism (non-modal) in the amplification of the vortex mode, in addition to the feeding mechanism by the fundamental oblique disturbances.

Instabilities in high-supersonic and hypersonic regimes have been investigated for various geometries, with the present discussion confined to flat plates (Fezer and Kloker, 2002; Unnikrishnan and Gaitonde, 2019; Zhou et al., 2022; Franko and Lele, 2013; Egorov and

Novikov, 2016). Fezer and Kloker (2002) indicated that first-mode oblique breakdown would be the most viable path to transition over a flat plate whereas the second-mode fundamental resonance mechanism is favored on a straight cone at Mach 6.8. Leinemann et al. (2020) could not differentiate the dominant breakdown mechanism between second-mode-induced fundamental resonance and first-mode-induced oblique breakdown, contrary to the straight-(Sivasubramanian and Fasel, 2015) and flare cones (Hader and Fasel, 2019; Sivasubramanian and Fasel, 2014) where the former was found predominant. At Mach 6.0, the first-mode oblique breakdown was shown to be the most likely scenario over an adiabatic flat plate (Unnikrishnan and Gaitonde, 2019). A comparison of fundamental/subharmonic and oblique-breakdown mechanisms at the same Mach number has identified the latter as the most viable path to transition (Franko and Lele, 2013). An overshoot in skin friction and heat transfer coefficients, compared to the theoretical turbulent estimations, was observed in the oblique breakdown. The reason was attributed to the rapid amplification of the steady vortex mode that plays a significant role in momentum and thermal energy transfer in the vicinity of the breakdown region. Even in the hypersonic regime, despite the LST results in fig. 1.8b, indicating a higher growth rate for the second mode than the first mode, first-mode oblique breakdown may still not be superseded by the second-mode-induced transition. This is due to the amplification of the first mode in a wider streamwise extent than the second mode instabilities (Malik, 1989). The predominant mechanism alters significantly depending on the wall cooling rate, Mach number, geometry, and the interested range of Reynolds number. Thus, a rigorous analysis of numerical and experimental results is a must when studying boundary-layer instabilities.

1.2 Transition control using streaks

From a physics perspective, wind tunnel transition experiments using moderately high levels of disturbances have highlighted the emergence of streamwisely elongated structures, taking the form of alternating streaks of high and low-velocity regions in the spanwise direction (Alfredsson and Matsubara, 2000). From a theoretical perspective, (Ellingsen and Palm, 1975) introduced a growth mechanism by considering the inviscid evolution of an initial disturbance independent of the streamwise coordinate in a shear layer. They demonstrated that the streamwise velocity component could grow linearly over time, resulting in the formation of alternating low- and high-velocity streaks. Building upon this, (Landahl, 1975, 1980) extended their findings to the linear evolution of localized disturbances and offered a physical explanation for this growth, known as the lift-up effect. He explained that in a shear layer, a wall-normal displacement of a fluid element would cause a perturbation in the streamwise velocity because the fluid particle initially retains its horizontal momentum. This mechanism is especially effective when weak pairs of quasi-streamwise counter-rotating vortices lift low-velocity fluid away from the wall while bringing high-velocity fluid toward it. As a result, spanwise inhomogeneities are generated, leading to the formation of streaks. This three-dimensional phenomenon play a critical role in driving the flow to transition. Their persisting existence in flow fields, especially in regions where vortical modes, such as Görtler (Görtler, 1940; Schrader et al., 2011; Ducoin et al., 2017) and cross-flow (Saric et al., 1998; Bippes, 1999) vortices, dominate the transitional region, led to the consideration of these vortices as a potential alternative for delaying and possibly even controlling the transition. The method was initially applied to incompressible flows. Closely spaced streak vortices, *i.e.*, those carrying higher wavenumber than the most-amplified mode are found effective in postponing the transition onset by dampening the most-amplified cross-flow vortices over an infinite swept wing (Wassermann and Kloker, 2002). These structures regulate the flow field by carrying the high-momentum fluid to the wall and the low-momentum away from the wall, which in turn attenuates the growing disturbances inside the boundary layer to have a longer laminar flow regime. Then, the use of these vortical structures was extended to a flat-plate configuration where TS waves dominate the transition mechanism in a low-disturbance environment. Cossu and Brandt (2002*a*) used optimal perturbations (Schmid and Henningson, 2001) which experience the highest transient growth and generate streamwisely elongated high and low-speed velocity regions (Andersson et al., 2001), also known as velocity streaks. Consequently, the mean velocity profile becomes fuller which is in favor of stabilizing the flow in a typical laminar boundary layer (Cousteix, 2005). The streaks were found capable of delaying transition by dampening the two-dimensional TS waves while early transition might be triggered above some critical streak amplitude (Cossu and Brandt, 2002*a*). The stabilizing effect on the TS waves in a low speed-boundary layer was further verified by experiments where a series of spanwise distributed roughness elements are used to generate the streaks of moderate amplitudes (Fransson et al., 2005, 2006). Furthermore, non-linear parabolized-stability-equations (PSE) were used to study the interaction of the optimally growing streaks with TS and oblique waves. For the selected initial streak amplitudes, both types of instabilities were somewhat reduced. The streak that most effectively dampens the TS wave was identified with a higher wavenumber than the optimal streaks, and it necessitates a lower amplitude (Bagheri and Hanifi, 2007). Additionally, alternative methods such as miniature vortex generators (Shahinfar et al., 2012) or plasma actuators (Dörr and Kloker, 2018) were also used to generate streamwise elongated streaks and highlight their stabilizing influence in low-speed boundary layers.

After having studied bypass transition induced by optimal streaks (Paredes et al., 2016*b*), it was observed that the streaks that experience weakly-nonlinear transient growth might also be beneficial in dampening three-dimensional first-mode instabilities. The necessary condition for a successful transition control is that the streaks should carry at least two times the wavenumber of the concerning first-mode oblique instability wave (Paredes et al., 2017). These "control" streaks were investigated in a non-linear oblique breakdown regime in a comprehensive DNS study at Mach 2.0 by Sharma, Shadloo, Hadjadj and Kloker (2019). A blowing/suction strip, placed at the wall, was used to generate the streaks which decay rapidly in the streamwise direction upon their generation. This is contrary to the streaks generated with optimal disturbances which grow in a large streamwise distance (Paredes et al., 2017). Streaks having four to five times the wavenumber of the most amplified first mode were found to be the most effective in controlling the transition while highlighting the importance of the maximum streak amplitude above which an earlier transition was induced. The hampering role of the mean-flow-deformation (MFD) has been pointed out, while the three-dimensional part of the control was also found to be stabilizing the oblique waves with high wavenumbers whose effect is seen when the MFD is weakened significantly. The latter finding contradicts Paredes et al. (2017) where the three-dimensional part of the control was found to be marginally destabilizing the flow field and leading to higher integrated growth rates. From the physical point of view, the MFD can be defined as the mean deformation of the flow field from its baseflow. The streak employment method was also found to be stabilizing the flow in the presence of a multi-frequency point source, generating broadband disturbances (Kneer et al., 2022). As an alternative approach to generating the control streaks, roughness elements were tested and found to have more enhanced control performance by causing the MFD to persist for a longer streamwise distance. In a preceding study, the effect of the moderately cooled wall, *i.e.* 10% with respect to the adiabatic wall temperature for laminar flows, control streaks were investigated at Mach 2.0, see Kneer (2020). The accumulation of the stabilizing effects of both of these methods led to a further transition delay by reducing the growth of the fundamental disturbance mode.

Transition control using streaks was also extended to high-supersonic and hypersonic regimes by Ren et al. (2016) where the non-linear PSE were used to simulate the flow field. It was shown that transiently growing sub-optimal streaks can indeed stabilize the two-dimensional first- and the second-mode instabilities, separately in supersonic boundary layers, and simultaneously in hypersonic boundary layers. Paredes et al. (2016*a*) used non-linear plane-marching PSE to study a hypersonic flow over a circular cone with zero angle of attack. The findings indicated that weakly non-linear optimally growing streaks stabilize the planar Mack mode while the stability of the three-dimensional second mode, which has an azimuthal wavelength equal to streak spacing, highly depends on the streak amplitude. The MFD was found to be strongly stabilizing, conforming with the findings of Ren et al. (2016), whereas the 3-D part of the control results in a longer amplification regime with an intermediate damped zone. Furthermore, a similar numerical investigation was conducted for a flow/geometry configuration matching the ascent phase of a hypersonic flight experiment (HIFiRE-1) by Paredes et al. (2019). Although the planar second mode was stabilized regardless of the disturbance frequency, the stabilizing effect of the MFD was inferior to that of the 3-D part of the control. Besides, in the presence of the streaks, the critical N-factor (N_{crit}, streamwisely integrated growth rate) based on experimental findings was reached both by planar and oblique second modes further downstream, indicating a transition delay. However, oblique as well as planar waves attain N_{crit} at approximately the same streamwise position in case of a lower frequency. That is to say, the transition mechanism was strongly altered by the control streaks provided that the planar Mach-mode was reported to be the most viable path to transition in this flow/geometry configuration which for the N_{crit} holds no longer reliable. In a recent study, streaky flow generated through the optimal growth approach was investigated in the presence of white-noise forcing (Caillaud, 2022). A similar mechanism, as described in Paredes et al. (2019), reveals the appearance of an additional high-frequency corresponding to the second-mode frequency region. This pertains to the subharmonic second-mode instability, characterized by half a wavenumber of the tested streaks. Besides, stabilization of the Mack mode below a certain streak amplitude was indicated whereas a strong amplification of the subharmonic first-mode instability was highlighted for any streak amplitude. The most recent study of transition control using the streak employment method was conducted by Zhou et al. (2023). Streaks that have two-to-six times the wavenumber of the oblique second-mode disturbance were found to be stabilizing the concerning instability. The primary stabilizing effect of the control stems from the spanwise component of the streaks whereas the MFD was reported to be destabilizing the disturbance for low-initial-streak amplitude. However, certain ambiguities in this investigation regarding the low-resolution simulations as well as the contradictory results, which are elaborated in Chapter 6, require a confirmation of the findings.

The recent investigations present valuable knowledge regarding transition control using the streak employment method. However, there still remain various questions to be answered. Those that are to be addressed within the scope of this thesis are given as follows:

- How effective is the streak employment method in suppressing the first-mode-induced oblique breakdown under a weakly cooled/heated wall?

- In what range of streak amplitude, under the effect of different thermal boundary conditions, first mode instabilities can be delayed?
- Can we apply these control streaks to dampen second-mode instabilities? What are the roles of the MFD and the 3-D part of the control in a possible stabilization?

To shed light upon these queries, supersonic boundary layers are simulated in a direct numerical simulation environment. Transition is triggered in a controlled fashion by a perturbation source mounted at the wall to inject selected pair(s) of disturbances.

1.3 Scope of the present work

A thorough examination of the historical progression of boundary-layer transition research, addressing both the theoretical aspects of breakdown mechanisms and transition control methods is presented. While investigating the streak employment method, certain unanswered questions have been identified, prompting the current research work to address these gaps. The overview of this thesis is given as follows:

Chapter 2: This chapter outlines the Navier-Stokes equations used in our analysis and provides insights into the numerical schemes employed by the direct numerical simulation solver. The concept of linear stability theory and underlying assumptions are introduced.

Chapter 3: Here, the validation of the DNS code and the LST solver are performed, delving into the scientific terminology of instabilities and eigenvalue spectra. DNS cases are examined to explore various aspects of perturbed flow fields, and the turbulent flow field is evaluated using first-order statistics.

Chapter 4: In an attempt to address the previously mentioned two main questions, the effect of weak wall heating/cooling on the streak employment method with the optimal wavenumber *i.e.*, five times the fundamental disturbance, has been investigated. The effective transition delay has been achieved by utilizing streaks within a specific amplitude range. The results emphasize the cumulative stabilizing impact of wall cooling on the streaks, along with the detrimental influence of wall heating on their initial amplitude.

Chapter 5: The Stanton number behavior in laminar flat plate boundary layers has been investigated using the self-similar solutions of the compressible boundary-layer equations as well as direct numerical simulations. A comprehensive analysis is conducted to understand its contradictory trends from the previous chapter with existing literature.

Chapter 6: Transition control using the streak employment method is applied to a controlled transitional boundary layer to suppress the three-dimensional (oblique) second mode instability in order to explore the remaining question. A short parametric study of the wavenumber identifies the control streaks successfully delaying transition. In contrast to the first-mode instability control analysis, streamwisely elongated streaks are observed to grow transiently rather than decaying following their generation.

Chapter 7: The summary of the presented research work together with the concluding remarks are given. A discussion concerning the possible future routes for a further understanding of the streak employment method is provided.

Chapter 2

Governing equations and numerical methods

Contents

In this chapter, the governing equations used to describe the fluid motion along with the underlying assumptions are presented. Numerical schemes adopted in the solver for the viscous and inviscid fluxes as well as time integration strategy are detailed. Finally, a brief description of the liner stability theory and the method of solving the resulting eigenvalue problem are provided.

2.1 Governing equations

The motion of any continuous medium is governed by the fundamental principles of mechanics and thermodynamics. These principles form a set of equations, called Navier-Stokes Equations (NSE) which comprise the conservation of mass, momentum, and energy. These equations can be solved by using different approaches which are generally regarded as; Reynolds-Averaged Navier-Stokes (RANS), Large-Eddy Simulation (LES), and Direct Numerical Simulation (DNS) in the fluid dynamics community. These methods are identified by their capability of resolving spatio-temporal scales in turbulent flow fields. The present fundamental study adopts the DNS approach where neither modeling, as in RANS, nor filtering, as in LES, are applied, but all the scales are resolved. The choice is deemed compulsory for a comprehensive understanding of the interactions between different instabilities inside the boundary layer and the eventual breakdown to turbulence.

Now, three-dimensional, compressible and unsteady Navier-Stokes equations in Cartesian coordinates $x_i = (x, y, z)$ are expressed as:

$$\frac{\partial \rho}{\partial t} + \frac{\partial \rho u_j}{\partial x_j} = 0, \tag{2.1}$$

$$\frac{\partial \rho u_i}{\partial t} + \frac{\partial \rho u_i u_j}{\partial x_j} = -\frac{\partial p}{\partial x_i} + \frac{\partial \tau_{ij}}{\partial x_j}, \tag{2.2}$$

$$\frac{\partial \rho E}{\partial t} + \frac{\partial (\rho E + p) u_j}{\partial x_j} = -\frac{\partial \dot{q}_j}{\partial x_j} + \frac{\partial u_i \tau_{ij}}{\partial x_j}, \tag{2.3}$$

Here, u_i is the velocity vector, ρ, and p represent density, and pressure, respectively. Meanwhile, the heat diffusion flux is:

$$q_j = -\lambda \frac{\partial T}{\partial x_j} \tag{2.4}$$

thermal conductivity is designated by λ and the pressure is estimated through the total energy E as:

$$p = (\gamma - 1)\Big(\rho E - \frac{1}{2}\rho u_i u_i\Big), \tag{2.5}$$

where γ is the heat capacity ratio and τ is the viscous stress tensor, given by:

$$\tau_{ij} = \mu\Big(\frac{\partial u_j}{\partial x_i} + \frac{\partial u_i}{\partial x_j} - \frac{2}{3}\frac{\partial u_k}{\partial x_k}\delta_{ij}\Big), \tag{2.6}$$

δ_{ij} is the Kronecker delta. The fluid of interest is air with the linear dependency of the shear stress to the velocity gradient (Newtonian law). The heat capacities are considered constant with the heat capacity ratio, $\gamma = 1.4$ and the dynamic viscosity is assumed to be only temperature dependent, and calculated by the Sutherland's law $\mu(T) = (C_1 T^{3/2})/(T + S)$ (Sutherland, 1893). Here, Sutherland's temperature for air is $S = 110.4$ K and the constant $C_1 = 1.458 \times 10^{-6}$ kg/ms$\sqrt{\mathrm{K}}$ which is calculated through $C_1 = \mu_r (T_r + S)/T_r^{3/2}$. Reference dynamic viscosity of air $\mu_r = 1.716 \times 10^{-5}$ kg/ms at the reference temperature, T_r of 273.15 K, where the subscript r refers to the reference values.

2.2 Numerical schemes

The study utilizes an in-house developed Direct Numerical Simulation code known as **C**ompressible **H**igh-**O**rder **C**ode using **W**eno **A**daptive **S**tencils (CHOC-WAVES), which solves compressible, unsteady, three-dimensional Navier-Stokes equations in an explicit manner on a Cartesian mesh for perfect gases. The code, fully parallelized with the MPI/OMP library and exploits HDF5 library for Input/Output (IO). It has been tested in various applications with detailed descriptions of validation cases in Hadjadj et al. (2015); Shadloo et al. (2014); Sharma, Shadloo, Hadjadj and Kloker (2019). Convective fluxes are discretized by a hybrid locally-conservative sixth-order skew-symmetric split-centered finite-difference scheme as proposed in Pirozzoli (2010) with a fifth-order Weighted Essential Non-Oscillatory (WENO) scheme. A fourth-order central scheme is used to approximate the diffusive terms which are expressed in compact form (Laplace formulation is employed). Time integration is carried out by using a classical explicit third-order Total-Variation-Diminishing (TVD) Runge-Kutta scheme (Shu and Osher, 1988). For details concerning the scalability of the code, interested readers are referred to Piquet (2017).

2.2.1 Treatment of convective fluxes

Accuracy and robustness are essential features of numerical schemes in order to properly resolve the flow field in detail. In supersonic flows, there might exist regions with strong gradients such as shock waves and slip lines known as contact discontinuities in inviscid gas dynamics which require special attention in adjusting the optimal characteristics.

2.2.1.1 WENO scheme

Essentially Non-Oscillatory (ENO) schemes are based on the idea of determining the numerical flux from a high-order reconstruction on a single adaptive stencil that is selected to avoid interpolation through discontinuities as much as possible. However, these schemes suffer from convergence problems towards a stationary solution, as well as from a loss of accuracy (Pirozzoli, 2010). To circumvent the limitations of the ENO, the WENO schemes are devised which construct a high-order numerical flux from a convex linear combination of a weighted reconstruction of lower-order polynomials (stencils). The weighting of the stencils aims at maximizing the accuracy of the scheme in the so-called smooth regions while canceling the effect of the adaptive stencil near the discontinuity.

In the CHOC-WAVES code, several variants of the WENO scheme are available, such as the classical WENO scheme of Jiang and Shu (1996), the broadband WENO scheme of Martín et al. (2006) or the Mapped-WENO scheme of Henrick et al. (2005). These schemes can be used either at order 3 (r = 2) or at order 5 (r = 3), the accuracy of the scheme being 2r - 1.

For the description of the calculation method of the WENO scheme, a one-dimensional scalar conservation equation is used (Nasr, 2012):

$$\frac{\partial u}{\partial t}+\frac{\partial f(u)}{\partial x}=0 \tag{2.7}$$

$f(u)$ being the characteristic flux is decomposed into a positive and negative parts

$$f(u)=f^{+}(u)+f^{-}(u) \tag{2.8}$$

These two fluxes represent the non-negative and non-positive propagation speeds, respectively:

$$\frac{df^{+}(u)}{du}\geq 0, \qquad \frac{df^{-}(u)}{du}\leq 0 \tag{2.9}$$

whose decomposition is performed based on Lax-Friedrichs (LF) scheme which is given as:

$$f^{\pm}(u)=\frac{1}{2}(f(u)\pm\alpha u) \tag{2.10}$$

where $\alpha=\max_u|f'(u)|$ is the greatest value on the concerned mesh on which the flux at the interface is decomposed as:

$$f_{i+1/2}=f^{+}_{i+1/2}+f^{-}_{i+1/2} \tag{2.11}$$

The flux $f^{+}_{i+1/2}$ (similarly $f^{-}_{i+1/2}$) is reconstructed through interpolating the $f^{+}_{i+1/2}$ (similarly $f^{-}_{i+1/2}$) fluxes from three stencils $S=\{S1,...,S3\}$. The WENO scheme uses a convex combination of three consecutive fluxes to obtain maximum precision in the region of weak and negligible gradients:

$$\begin{cases} f^{+(1)}_{i+1/2} & = & \frac{2}{6}f^{+}_{i-2} & - & \frac{7}{6}f^{+}_{i-1} & + & \frac{11}{6}f^{+}_{i} \\ f^{+(2)}_{i+1/2} & = & -\frac{1}{6}f^{+}_{i-1} & + & \frac{5}{6}f^{+}_{i} & + & \frac{2}{6}f^{+}_{i+1} \\ f^{+(3)}_{i+1/2} & = & \frac{2}{6}f^{+}_{i} & + & \frac{5}{6}f^{+}_{i+1} & - & \frac{1}{6}f^{+}_{i+2} \end{cases} \tag{2.12}$$

Thus, the numerical flux at the interface for the 5^{th} order is estimated as follows:

$$f_{i+1/2} = \sum_{l=1}^{r} \omega_l^+ f_{i+1/2}^{+(l)} \tag{2.13}$$

where the nonlinear weighting coefficients are given as:

$$\omega_l^+ = \frac{\alpha_l^+}{\sum_{l=1}^{r} \alpha_l^+}, \qquad \alpha_l^+ = \frac{d_l^+}{(\epsilon + \beta_l^+)^2} \tag{2.14}$$

the weights $d_l^+ = d_l^- = d_l$ allow to obtain an optimum precision with the present 5^{th} order WENO scheme. The weights in this work are $d_1 = 1/10$, $d_2 = 6/10$, $d_3 = 3/10$, where ϵ is a small number ($\epsilon = 10^{-6}$) to avoid division by zero (Jiang and Shu, 1996). To decrease the weight of the stencils containing the discontinuity, a β_l^+ parameter is used as an indicator. It is defined as the sum of the norms of all the derivatives of the polynomials used for interpolation and can be written as:

$$\begin{cases} \beta_1^+ = \frac{13}{12}(f_{i-2}^+ - 2f_{i-1}^+ + f_i^+)^2 + \frac{1}{4}(f_{i-2}^+ - 4f_{i-1}^+ + f_i^+)^2 \\ \beta_2^+ = \frac{13}{12}(f_{i-1}^+ - 2f_i^+ + f_{i+1}^+)^2 + \frac{1}{4}(f_{i-1}^+ - 4f_i^+ + f_{i+1}^+)^2 \\ \beta_3^+ = \frac{13}{12}(f_i^+ - 2f_{i+1}^+ + f_{i+2}^+)^2 + \frac{1}{4}(f_i^+ - 4f_{i+1}^+ + f_{i+2}^+)^2 \end{cases} \tag{2.15}$$

In the same manner, the negative part of the numerical flux ($f_{i+1/2}^-$) is calculated by replacing f^+ with f^-.

2.2.1.2 Conservative split-centered scheme (skew-symmetric)

It is acknowledged that the use of centered finite difference approximations leads to instabilities, even in the absence of shock waves, when they are used at very low viscosities, or even zero, which is the case for hyperbolic equations. There exist various methods to ensure numerical stability for flows without discontinuity. For a detailed review of these methods, the reader is referred to Pirozzoli (2010).

One of the known methods is the use of the split form of the derivatives of the convective terms in the Navier-Stokes equations. This method is based on the idea of writing the convective terms in a skew-symmetric form. However, the approximations obtained cannot be written in a locally conservative form, *i.e.* in the form of a divergence as they are presented in eq. 2.17. Based on these findings, Pirozzoli (2010) proposes a locally conservative approximation of the convective terms of the compressible Navier-Stokes equations, written as:

$$\frac{\partial \rho u_k \varphi}{\partial x_k} \tag{2.16}$$

where φ is a generic scalar proper, reduced to unity for the continuity equation, to the velocity vector $u_i (i = 1,2,3)$ for the momentum, and to the enthalpy $\mathcal{H} = \frac{\gamma}{\gamma-1}\frac{p}{\rho} + \frac{u^2}{2}$ for the energy equation.

Basic principle of formulation

In case of one-dimensional, equidistantly distributed grid points i.e. $x_j = j.h$, the conservative finite difference approximation of the convective terms can be written as[4]:

$$\left.\frac{\partial \rho u \varphi}{\partial x}\right|_{x=x_j} \approx \frac{1}{h}(\hat{f}_{j+1/2} - \hat{f}_{j-1/2}), \tag{2.17}$$

where $\hat{f}_{j+1/2}$ is the numerical flux. Equation 2.17 is expanded to dictate the split form of the convective derivatives either as:

$$\frac{\partial \rho u \varphi}{\partial x} = \frac{1}{2}\frac{\partial \rho u \varphi}{\partial x} + \frac{1}{2}\varphi\frac{\partial \rho u}{\partial x} + \frac{1}{2}\rho u\frac{\partial \varphi}{\partial x}, \tag{2.18}$$

or

$$\frac{\partial \rho u \varphi}{\partial x} = \frac{1}{2}\frac{\partial \rho u \varphi}{\partial x} + \frac{1}{2}u\frac{\partial \rho \varphi}{\partial x} + \frac{1}{2}\rho\varphi\frac{\partial u}{\partial x}. \tag{2.19}$$

Replacing the continuous derivative operators in eqs. 2.18 and 2.19 by their finite difference formulations gives

$$\left.\frac{\partial fg}{\partial x}\right|_{x=x_j} \approx D_s(fg)_j \equiv \frac{1}{2}D(fg)_j + \frac{1}{2}f_j Dg_j + \frac{1}{2}g_j Df_j, \tag{2.20}$$

where the discrete approximation of the split convective derivative term is represented by D_s, while Df_j stands for the discrete approximation of the first derivative of f at the node x_j. In the split forms, $(f = \rho u,\ g = \varphi)$ or $(f = \rho\varphi,\ g = u)$ in eqs. 2.18 and 2.19, respectively. Here, a standard central approximation of the first derivative is written as

$$Df_j = \sum_{l=1}^{L} a_l D^l f_j, \tag{2.21}$$

where the coefficients a_l can be obtained by either acquiring the exact order of accuracy of the approximation or from the approximation of the discrete phase velocity closest to the exact one for a wide range of wavenumbers, providing the class of the dispersion-relation-preserving (DRP) schemes (Pirozzoli, 2010). Also,

$$D^l f_j = \frac{1}{h}(f_{j+l} - f_{j-l}), \tag{2.22}$$

---

[4] The following numerical development is taken from the article by Pirozzoli (2010).

Inserting eqs. 2.21 and 2.22 into eq. 2.20 allows us to obtain the conservation form of the convective derivative approximation. When $L = 1$, the following is obtained for the second-order approximation:

$$\hat{f}_{i+1/2} = \frac{1}{4}(f_j + f_{j+1})(g_j + g_{j+1}), \tag{2.23}$$

while a conservative approximation of 2.17 is written as:

$$\hat{f}_{i+1/2} = \frac{1}{2}(f_j g_j + f_{j+1} g_{j+1}). \tag{2.24}$$

Considering one single term (D^l) in eq. 2.22, inserting into eq. 2.21, would give:

$$D_s^l(fg)_j = \frac{1}{2}D^l(fg)_j + \frac{1}{2}f_j D^l g_j + \frac{1}{2}g_j D^l f_j = \frac{2}{h}\Big(\widetilde{(f,g)}_{j,l} - \widetilde{(f,g)}_{j-l,l}\Big), \tag{2.25}$$

such that

$$\widetilde{(f,g)}_{j,l} = \frac{1}{4}(f_j + f_{j+l})(g_j + g_{j+l}), \tag{2.26}$$

is a two-point, two-variable discrete mean operator. It is to be noted that eq. 2.25 is not written in the conservative form as in eq. 2.17. Through manipulation, it can be re-casted as:

$$D_s^l(fg)_j = \frac{1}{h}(\hat{f}^l_{j+1/2} - \hat{f}^l_{j-1/2}), \tag{2.27}$$

with

$$\hat{f}^l_{j+1/2} = 2\sum_{m=0}^{l-1} \widetilde{(f,g)}_{j-m,l}, \tag{2.28}$$

By summing up all the partial fluxes, the total flux is then written as:

$$\hat{f}_{j+1/2} = \sum_{l=1}^{L} a_l \hat{f}^l_{j+1/2}, \tag{2.29}$$

this results in

$$\hat{f}_{j+1/2} = 2\sum_{l=1}^{L} a_l \sum_{m=0}^{l-1} \widetilde{(\rho u,\varphi)}_{j-m,l}, \tag{2.30}$$

and

$$\hat{f}_{j+1/2} = 2\sum_{l=1}^{L} a_l \sum_{m=0}^{l-1} \widetilde{(\rho\varphi,u)}_{j-m,l}. \tag{2.31}$$

It is seen that eqs. 2.30 and 2.31 correspond to the form of eqs. 2.18 and 2.19, respectively in case of $a_l = a_1 = 1/2$.

Generalized form

Full expansion of the triple products in eq. 2.16 yields additional robustness for flows with strong density variations (Pirozzoli, 2010). The obtained generalized split form is written as follows

$$\begin{aligned}\frac{\partial \rho u \varphi}{\partial x} = \alpha \frac{\partial \rho u \varphi}{\partial x} + \beta \Big(u \frac{\partial \rho \varphi}{\partial x} + \rho \frac{\partial u \varphi}{\partial x} + \varphi \frac{\partial \rho u}{\partial x} \Big) \\ + (1-\alpha-2\beta) \Big(\rho u \frac{\partial \varphi}{\partial x} + \rho \varphi \frac{\partial u}{\partial x} + u \varphi \frac{\partial \varphi}{\partial x} \Big),\end{aligned} \tag{2.32}$$

Conservative approximations of the split form 2.32 can be recovered only under particular circumstances. In case of $\alpha = \beta = 1/4$, following the identical approach as for the "standard" split formulations, one obtains:

$$\hat{f}_{j+1/2} = 2 \sum_{l=1}^{L} a_l \sum_{m=0}^{l-1} (\widetilde{\rho, u, \varphi})_{j-m,l}, \tag{2.33}$$

where the two-point, three-variable discrete averaging operator is defined as

$$(\widetilde{f, g, h})_{j,l} = \frac{1}{8}(f_j + f_{j+l})(g_j + g_{j+l})(h_j + h_{j+l}). \tag{2.34}$$

with the constants a_l, obtained through Taylor's expansion, are presented in table 2.1. It is highlighted that the effect of density variation is considered in eq. 2.34, which is independent of the other variables, u and φ. In this study, 6^{th} order central scheme is used.

Table 2.1: Central scheme coefficients of second to eight order.

Order (2L)	$i=1$	$i=2$	$i=3$	$i=4$
2	$a_1 = 1/2$	-	-	-
4	$a_1 = 8/12$	$a_2 = -1/12$	-	-
6	$a_1 = 45/60$	$a_2 = -9/60$	$a_3 = 1/60$	-
8	$a_1 = 672/840$	$a_2 = -168/840$	$a_3 = -1/840$	$a_4 = 3/840$

2.2.1.3 Hybrid scheme

It is acknowledged that WENO schemes are somewhat dissipative in the regions of strong gradients. Meanwhile, central difference schemes might lead to some stability issues in the vicinity of weak shocks or shocklets, like those generated in turbulent flow fields. Thus, a hybrid scheme that acts as a switch between the WENO scheme and the skew-symmetric centered scheme has been utilized. The procedure allows the WENO scheme to be activated in the strong gradient regions, preventing any spurious oscillations with its dissipative nature whereas the skew-symmetric scheme is used in the rest of the region to ensure accuracy and the stability of the solver. The hybrid scheme is defined as:

$$\frac{\partial \varphi}{\partial x}^{Hybrid} = (1-\Theta)\frac{\partial \varphi}{\partial x}^{Skew-symmetric} + \Theta\frac{\partial \varphi}{\partial x}^{WENO}, \tag{2.35}$$

To sustain the stability of the skew-symmetric scheme, regions of strong gradients should be located accurately in the computational domain. Thereafter, the shock sensor proposed by Ducros et al. (1999) based on the sensor presented by Jameson et al. (1981) is used:

$$\theta = \frac{(\nabla.\boldsymbol{u})^2}{(\nabla.\boldsymbol{u})^2 + (\nabla\times\boldsymbol{u})^2 + \epsilon}, \tag{2.36}$$

where numerical divergence is prevented using a small number *i.e.* $\epsilon = 10^{-5}$. A new value of ϵ is devised by Pirozzoli (2011) to overcome the inadequacy of the Ducros sensor outside of the boundary layer (where $\nabla\times\boldsymbol{u} \approx 0$) where the sensor becomes excessively sensitive to the dilatational fluctuation:

$$\epsilon = \left(\frac{u_\infty}{\delta_0}\right)^2, \tag{2.37}$$

The relation between the shock sensor and the hybrid scheme is put forward such that Θ is set as a switch equal to 0 or 1 with the limiter value, $\theta_0 = 0.02$

$$\begin{cases} \Theta = 1, & \text{if } \theta > \theta_0 \\ 0, & \text{otherwise.} \end{cases} \tag{2.38}$$

The sensor has been tested for different ϵ values in eq. 2.36. The analysis is performed using the adiabatic as well as isothermal cases in chapter 4. Figure A.1 illustrates the regions in the flow field where the shock sensor becomes activated for the perturbed flow. ϵ plays a crucial role, particularly in the free-stream and turbulent flow fields. When the parameter is set according to eq. 2.37, the sensor activates solely at one location within the provided $X-Y$ plane. This observation highlights the significance of appropriately selecting the ϵ value to ensure accurate shock detection and characterization in the numerical simulations. Following this analysis, eq. 2.37 is retained for estimating the ϵ in this work.

2.2.2 Treatment of viscous terms

In the CHOC-WAVES code, viscous fluxes are approximated using a fourth-order compact central difference discretization, in which the derivative in the longitudinal direction (in the wall-normal and spanwise directions, the computations are approximated by a standard central formulation) is written as[5]

$$(\mathcal{D}_x \boldsymbol{F_v})_i = \frac{\boldsymbol{F_v}_{i-2} - 8\boldsymbol{F_v}_{i-1} + 8\boldsymbol{F_v}_{i+1} - \boldsymbol{F_v}_{i+2}}{12\Delta x} + \mathcal{O}(\Delta x^4), \tag{2.39}$$

where $\mathcal{D}_x \boldsymbol{F_v} = \Delta x \partial_x \boldsymbol{F_v}$. The derivative of the primitive variables $\partial_x \psi$ are stored in $\boldsymbol{F_v}$. In the longitudinal direction, the derivatives in $\boldsymbol{F_v}$ are approximated using differently biased 5-point formulas of 4^{th} order on stencils lying in $S = \{i-2, i-1, i, i+1, i+2\}$

$$\begin{cases} (\mathcal{D}_x\psi)_{i-2} & = \frac{1}{12\Delta x}[-25\psi_{i-2} + 48\psi_{i-1} - 36\psi_i + 16\psi_{i+1} - 3\psi_{i+2}] & + \mathcal{O}(\Delta x^4), \\ (\mathcal{D}_x\psi)_{i-1} & = \frac{1}{12\Delta x}[-3\psi_{i-2} - 10\psi_{i-1} + 18\psi_i - 6\psi_{i+1} + \psi_{i+2}] & + \mathcal{O}(\Delta x^4), \\ (\mathcal{D}_x\psi)_{i+1} & = \frac{1}{12\Delta x}[-\psi_{i-2} + 6\psi_{i-1} - 18\psi_i + 10\psi_{i+1} + 3\psi_{i+2}] & + \mathcal{O}(\Delta x^4), \\ (\mathcal{D}_x\psi)_{i+2} & = \frac{1}{12\Delta x}[3\psi_{i-2} - 16\psi_{i-1} + 36\psi_i - 48\psi_{i+1} + 25\psi_{i+2}] & + \mathcal{O}(\Delta x^4). \end{cases} \tag{2.40}$$

Using these formulas results in a compact 5-point approximation that aligns with the standard 4^{th}-order expression for the second derivative.

2.2.3 Time integration

Time-integration schemes implemented in the code are mainly explicit TVD Runge-Kutta algorithms (Shu and Osher, 1988), *i.e.* classical 1^{st}-to-3^{rd} orders as well as 4^{th} order RK-Gill (Gill, 1951) and 2^{nd} order RK-Jameson. These schemes obey a restriction on the temporal increment which must be sufficiently small to properly take the unsteady character of the studied flows into consideration. In this study, 3^{rd} order TVD Runge-Kutta is chosen and the integration procedure is performed in three steps as follows:

$$\frac{\partial \boldsymbol{Q}(t,\boldsymbol{x})}{\partial t} = \mathcal{L}(t,\boldsymbol{x}), \tag{2.41}$$

where $\mathcal{L}$ is the discretization of the spatial operator

$$\begin{cases} \boldsymbol{Q}^1 & = \boldsymbol{Q}^n + \Delta t \mathcal{L}(\boldsymbol{Q}^n), \\ \boldsymbol{Q}^2 & = \frac{1}{4}\Big[3\boldsymbol{Q}^n + \boldsymbol{Q}^1 + \Delta t \mathcal{L}(\boldsymbol{Q}^1)\Big], \\ \boldsymbol{Q}^{n+1} & = \frac{1}{3}\Big[\boldsymbol{Q}^n + 2\boldsymbol{Q}^2 + 2\Delta t \mathcal{L}(\boldsymbol{Q}^2)\Big], \end{cases} \tag{2.42}$$

where Δt is the time step, $\boldsymbol{Q}^n$ is the value of the $\boldsymbol{Q}$ variable at an instant n, and $\boldsymbol{Q}^{(k)}$ are the intermediate values of $\boldsymbol{Q}^{(k=1,2)}$. The stability criterion used for the time-stepping

---

[5] The following numerical development is taken from the article by Chaudhuri et al. (2011).

is given as:

$$[C_{\Delta t}]_{i,j,k} = \left[\sum_{l=1}^{3} \frac{|u_l + c|}{\Delta x_l} + \frac{2\gamma\mu}{Pr} \sum_{l=1}^{3} \frac{\Delta x_l^2}{\rho} \right]_{i,j,k}, \tag{2.43}$$

where

$$\Delta t = \min \left[\frac{CFL}{(C_{\Delta t})_{i,j,k}} \right]. \tag{2.44}$$

the convective time is the first term on the right-hand side of the equation whereas the second term represents the diffusion time. Trials have shown that ensuring global numerical stability requires the Courant-Friedrichs-Lewy (CFL) number to be less than one, which is set as 0.9 in this study. For an insightful comprehension of the weighting of the terms on the time-stepping, base flow DNS data computed in Chapter 4 has been analyzed for the adiabatic as well as the isothermal cases. Once the statistical convergence of the parameters is satisfied, the analysis is performed. Figure A.2 displays the interplay between the limiting role of the viscous and inviscid parts of eq. 2.43. The impact of viscosity increases near the wall and with increasing wall temperature, whereas the inviscid part plays the dominant role in restricting the global time-stepping. Deeper analysis of the cooled wall highlights the predominant effect of the v-component of the velocity vector near the wall which is due to abrupt mesh stretching in the wall-normal direction. Indeed, the term remains the most influential factor up to near 2δ. A similar trend is observed also in the second viscous term which scales up with the mesh size in y-direction. The overall influence of the thermal boundary condition indicates a higher time-stepping for the cooled wall, thus resulting in a lower number of iterations to reach the identical physical time compared to the adiabatic and heated cases.

2.3 Linear stability analysis

The linear stability theory analyzes the stability of a steady base flow with respect to infinitesimally small sinusoidal disturbances. The flow field can be split into its steady base flow Φ_1 and unsteady perturbation as

$$\Phi(x,y,z,t) = \Phi_1(x,y,z) + \Phi'(x,y,z,t) \tag{2.45}$$

The principal assumptions behind the theory are (Groskopf et al., 2008; Groskopf and Kloker, 2016):

- Φ_1 is the steady solution to the Navier-Stokes equations
- The steady primary state is assumed to be parallel $\left(\frac{\partial}{\partial x} \equiv 0\right)$, leading to a local theory indicating that the change of flow properties per wavelength is negligible,

i.e. boundary layer does not grow

- the y-component of the velocity is set to zero, *i.e.* $v_1 \equiv 0$
- Initial perturbation is considered to be small which allows for a linearization by neglecting the quadratic terms of the disturbances

Following the concerning assumptions, it is assumed that any disturbance Φ' can be expressed by a wave-like ansatz:

$$\Phi' = \begin{bmatrix} \rho'(x,y,z,t) \\ u'(x,y,z,t) \\ v'(x,y,z,t) \\ w'(x,y,z,t) \\ T'(x,y,z,t) \end{bmatrix} = \begin{bmatrix} \hat{\rho}(y) \\ \hat{u}(y) \\ \hat{v}(y) \\ \hat{w}(y) \\ \hat{T}(y) \end{bmatrix} .e^{i(\alpha x+\beta z-\omega t)} \quad + \quad c.c \tag{2.46}$$

where $\hat{\Phi}(y)$ is the corresponding complex amplitude distribution of the perturbation in a plane perpendicular to the x- and z-axes. Also, α, β, and ω refer to the spatial wavenumbers in x- and z-directions and the frequency, respectively. Once the disturbance ansatz is applied, the stability equations are obtained from the Navier-Stokes equations simply by subtracting the governing equations of the unperturbed base flow from the flow field. We aim to find the solution within the spatial mode, with the given real input values for β and ω, where α represents the complex eigenvalue, with spatial amplification for growth rate $\alpha_i < 0$, that needs to be determined through the ensuing nonlinear eigenvalue problem (EVP) (Schmidt and Rist, 2014)

$$(\widetilde{\boldsymbol{L}} + \widetilde{\boldsymbol{M}}\alpha)\widetilde{\boldsymbol{q}} = 0, \tag{2.47}$$

where $\widetilde{\boldsymbol{q}} = (\hat{\rho},\ \hat{u},\ \hat{v},\ \hat{w},\ \hat{T},\ \alpha\hat{u},\ \alpha\hat{v},\ \alpha\hat{w},\ \alpha\hat{T})$ with the coefficient matrices, $\widetilde{\boldsymbol{L}}$ and $\widetilde{\boldsymbol{M}}$, of the discretized problems. The EVP is solved using the Chebyshev spectral method with Dirichlet boundary conditions applied at the wall and in the free stream, *i.e.* $(u' = v' = w' = T' = 0)$. Construction of the whole matrix allows to solve the complete range of eigenvalues *i.e.* employing the global method (Malik, 1990). Then, for a given streamwise location, an eigenvalue is selected to visualize the associated eigenvectors. The chosen eigenvalue is tracked by the algorithm that identifies eigenvectors at different streamwise locations and selects the ones with the highest correlation.

Using Chebyshev polynomials requires mapping the infinite and semi-infinite domains onto a finite domain. Thus, an algebraic stretching which transforms the physical domain $0 \leq y \leq y_{max}$ to the computational domain $-1 \leq \hat{y} \leq 1$ is employed as follows (Schmid and Henningson, 2001)

$$y = a\frac{1+\hat{y}}{b-\hat{y}}, \tag{2.48}$$

with

$$a = \frac{y_i y_{max}}{y_{max} - 2y_i}, \quad b = 1 + \frac{2a}{y_{max}}. \tag{2.49}$$

The variable y_i defines near the boundary layer height, up to which half of the points lie. Despite the advantage of clustering the grid near the wall, y_i should be carefully chosen in high-speed flows as the critical layer moves towards the boundary layer edge as the Mach number increases (Malik, 1990).

2.4 Conclusion

The governing equations of fluid motion, the numerical strategy and the CFD solver have been presented. The linear stability theory, inherent assumptions, and the LST code for solving the spatial nonlinear eigenvalue-problem have been introduced.

Chapter 3

Validation of the code

Contents

This chapter focuses on evaluating the accuracy and efficiency of the direct numerical simulation (DNS) code and the linear stability solver in the context of supersonic boundary layer flows. Linear stability results for different modes of disturbances as well as intrinsic limitations are discussed. Furthermore, DNS results for a supersonic/near-hypersonic transitional boundary layer are compared with reference data from Zhou et al. (2022). Laminar breakdown scenarios, triggered by first- and second-mode instabilities are elaborated, and different perturbation methods are presented. Eventually, the primary assessment of DNS results is conducted by tracking the evolution of disturbances within the boundary layer until reaching a fully-developed turbulent flow.

3.1 Linear stability analysis

In our linear-stability analysis solver, self-similar compressible boundary-layer profiles are applied to solve the entire spectrum for a single disturbance frequency at a given streamwise position in the flow and for a prescribed spanwise wavenumber (Schmidt and Rist, 2014). The initial analysis is performed for a designated pair of frequency and spanwise wavenumber associated with the first-mode instability. Figure 3.1 compares the complex wavenumber evolution along the streamwise direction and the two-dimensional eigenvalue spectra at a particular streamwise position. The wavenumber results are found to match almost perfectly, with a minor deviation observed in the real-valued streamwise component. The associated eigenvalue to the relevant first-mode instability wave is accurately captured at $x = 0.5$ m, streamwise direction, in the spectra which reveal three main branches. According to Tumin et al. (2007)'s classification, the left branch corresponds to the fast acoustic wave spectrum, while the right branch pertains to the slow acoustic wave spectrum. These designations are based on the phase speed of their origin, characterized by $c_r = 1 \pm 1/M_\infty$. Additionally, the vertical line of squares represents the continuous entropy and vorticity spectra with $c_r = 1$.

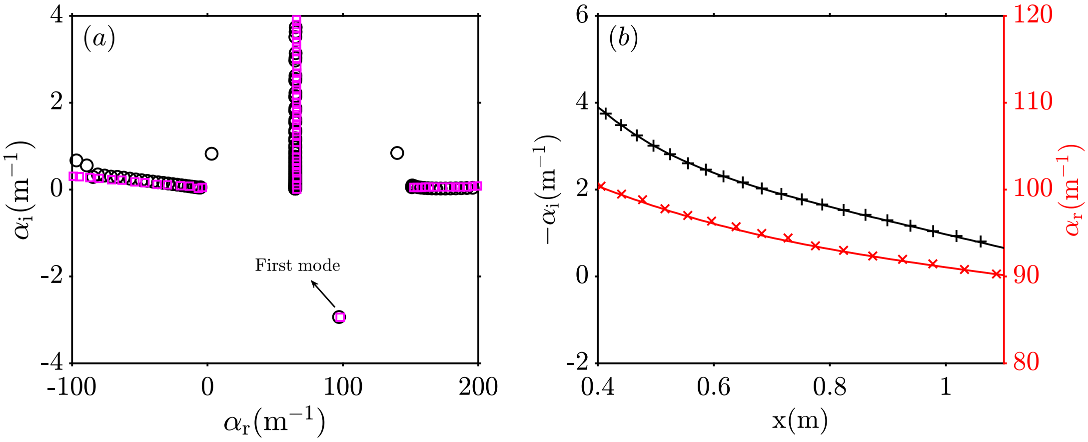

Figure 3.1: (a) 2-D eigenvalue spectra at $x = 0.5$ m and (b) streamwise evolution of the complex wavenumber α for the three-dimensional first mode with $f = 6.36$ kHz and $\beta = 196.2\ \mathrm{m}^{-1}$ at $M_\infty = 3.0, T_\infty = 103.6$ K, and $Re_u = 2.181 \times 10^6\ \mathrm{m}^{-1}$. LST (×, +, □) by Mayer, Von Terzi and Fasel (2011).

A similar analysis is performed with a 2-D second-mode instability, the most amplified mode of the Mack mode family. The linear stability theory (LST) results are compared with those obtained through the parabolic stability equations (PSE) in fig. 3.2. The LST results are depicted by a single N-factor curve, whilst the PSE predicts individual amplifications for different disturbance parameters. This discrepancy arises from PSE's departure from the parallel flow assumption inherent in LST. For comparison, the best agreement between the results is observed for v', indicating that it is the least affected dis-

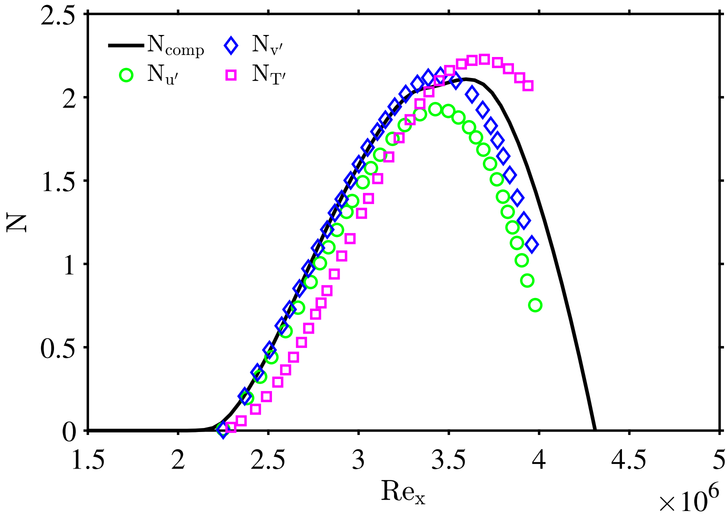

Figure 3.2: Integrated growth rates (N-factors) of a second-mode instability at $M_\infty = 4.5$, $T_\infty = 61.11$ K, and $Re_u = 3.306 \times 10^6$ m^{-1}. PSE results (symbols) by Jiang et al. (2004).

turbance component from the parallel-flow assumption. (Malik, 2003) has shown that the assumptions of LST may result in predicting the wavenumber and growth rate with significant errors when compared with the PSE and full Navier-Stokes (NS) results. However, despite the its limitations, LST remains as a valuable tool for accurately representing a significant portion of the transitional regime under low-disturbance flight-like conditions.

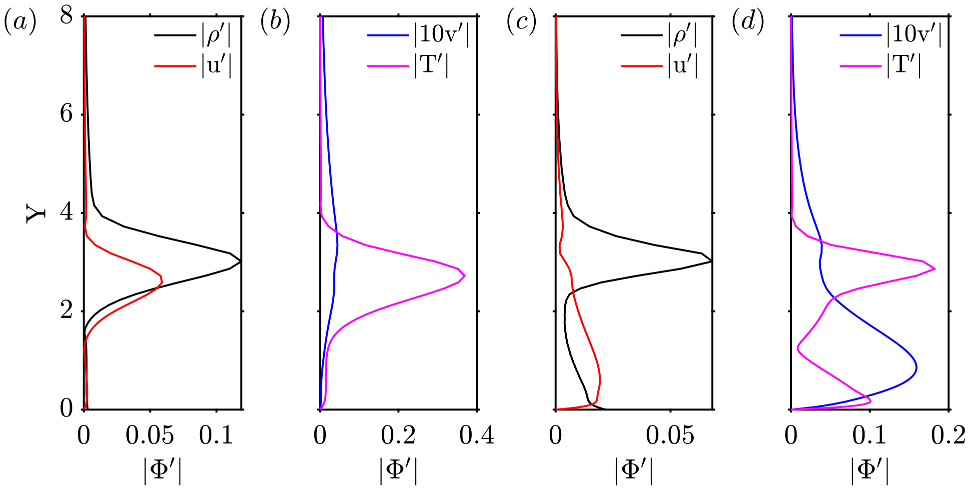

Figure 3.3: Eigenfunctions of the disturbance parameters for (a-b) the first mode ($f = 21$ kHz, $\beta = 392.70$ m^{-1}) and (c-d) second mode ($f = 91$ kHz, $\beta = 167.55$ m^{-1}) instabilities at $Re_x = 3.8 \times 10^6$, respectively.

In fig. 3.3, the eigenfunctions of disturbances corresponding to the previously examined first-mode and second-mode instability waves are depicted. In both cases, the maximum disturbance amplitude is obtained in T' where the eigenfunction exhibits a secondary peak near the wall with a comparable amplitude as the first peak in second-mode. Also, u',v' have their maxima near the wall, while for the first mode, they tend to be closer to the boundary-layer edge. The influence of the Dirichlet wall boundary condition, detailed in section 2.3, is also evident for u', v', and T'.

3.2 Direct numerical simulation

After validating the LST solver, the DNS code is used to simulate supersonic flat-plate boundary layers to demonstrate its capabilities. Transition is triggered by using first- and second-mode oblique disturbances separately. Second-mode induced transition case serves for validation while both breakdown scenarios are compared to discern the evolution of disturbances and alteration of the mean-flow field.

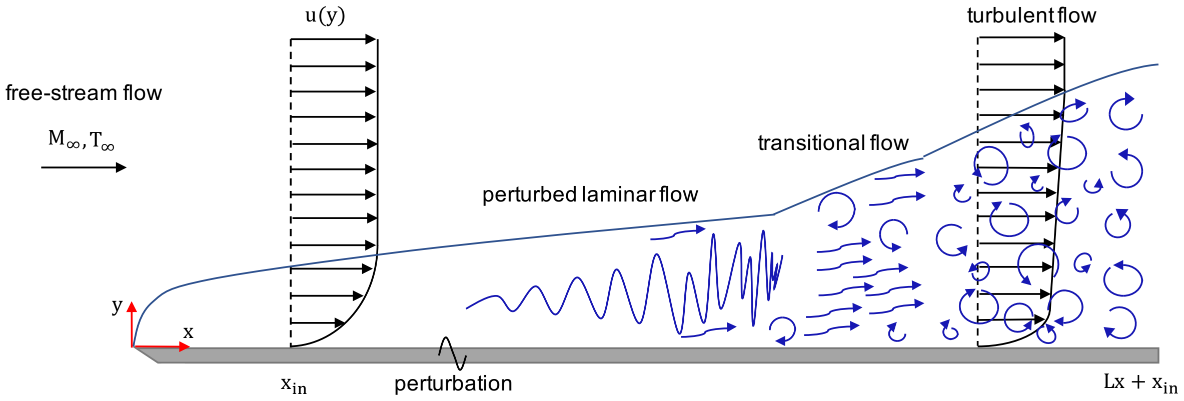

Figure 3.4: Schematic of the computational domain and boundary conditions.

3.2.1 Problem setup

The set-up is designed to keep the flow conditions of Zhou et al. (2022) at $M_\infty = 4.5$, $T_\infty = 65.15$ K, $Re_u = 7.2 \times 10^6$ as well as the wall temperature, fixed at $T_w = 4.0 \times T_\infty$. This corresponds approximately to 10% of wall cooling with respect to the adiabatic wall temperature for laminar flows where $Pr = 0.72$. Following the schematic of the computational domain depicted in fig. 3.4, the streamwise length and the height of the domain in the wall-normal direction are defined as $L_x = 0.8$ m and $L_y = 0.1$ m, respectively. The domain width, L_z, corresponds to the spanwise wavelength of the injected disturbance, as indicated in table 3.1. The mesh is designed to have a comparable resolution with the reference case in all directions. Grid is distributed equidistantly in streamwise and spanwise directions with $N_x = 3500$ and $N_z = 200$ number of points while a grid stretching function is used with $N_y = 200$ in the wall-normal direction for accurately capturing the inner boundary layer next to the wall which is given as

$$\begin{aligned} y_{j,str} &= L_y\left(1+\frac{\tanh(\kappa\times(y_{j,eq}-1))}{\tanh(\kappa)}\right), \\ y_{j,eq} &= j/Ny, \qquad \forall j\in\{1,\cdots,Ny\}. \end{aligned} \tag{3.1}$$

where $\kappa = 2.6$.

3.2.2 Method of perturbation

Transition can be triggered in numerous ways such as heat transfer, a blowing and suction strip at the wall, pressure gradient, surface roughness, curvature noise, free-stream turbulence intensity, etc. Here, the laminar boundary layer is excited via blowing and suction strip placed at the wall whose formulations are identical as Sharma, Shadloo, Hadjadj and Kloker (2019) and are expressed as

$$\dot{m}(x,y=0,z,t) = \rho v = A\rho_\infty u_\infty f(x)g(z)h_1(t), \tag{3.2}$$

$$f(x) = 4sin\theta(x)(1-cos\theta(x))/\sqrt{27}, \tag{3.3}$$

$$\theta(x) = 2\pi(x-(x_1-x_{in}))/(x_2-x_1), \tag{3.4}$$

$$g(z) = (-1)^k cos(2\pi kz/L_z), \tag{3.5}$$

$$h_1(t) = sin(h\omega t), \tag{3.6}$$

where A is the maximum disturbance amplitude given as $(\rho v)_w/(\rho_\infty u_\infty)$, $\dot{m}$ is the transverse mass flux, ω is the angular frequency of the excitation mode, h being the multiple of the fundamental frequency, and k the multiple of the fundamental spanwise wavenumber. The dimensional frequency and the spanwise wavenumber of the introduced perturbation are denoted by f_0 and β_0, respectively. For the sake of simplicity, the modes are labeled based on their contents *i.e.* the (h,k) standing for the frequency/spanwise wavenumber tuple. Here, (h,k) indicates the disturbance mode with frequency $h\times f_0$ and spanwise wavenumber $k\times\beta_0$. The tuples $(h=0,k)$ are the steady modes (waves), $(h>0,k)$ are known as the unsteady or the traveling modes whereas 2-D modes are designated by $(h\neq 0,0)$. For three-dimensional disturbances, the tuple stands for the sum of $(h,+k)$ and $(h,-k)$ for three-dimensional disturbances. Also, the mean-flow-deformation (MFD) is indicated by $(0,0)$ tuple.

3.2.3 Boundary conditions

Self-similar boundary layer (BL) profiles that are obtained by solving the compressible boundary layer equations are prescribed at the inlet. Appendix B provides detailed information regarding the BL solver. Supersonic inflow and outflow conditions are applied at the inlet ($x = x_{in}$) and at the outlet ($x = x_{in} + L_x$) of the computational domain, respectively. As for the rest of the boundaries, periodicity is imposed at the side walls as well as a slip condition with zero boundary-normal gradients imposed at the upper boundary. No-slip condition is applied at the wall with the permeable region occupied by the blowing/suction strip. To satisfy the boundary conditions, finite values on the ghost cells outside the computational domain are imposed. Depending on the physical condition to be satisfied, the conservative variables of the system of equations governing the flow are defined in these meshes.

Three DNS cases, which are enlisted in table 3.1, are investigated. Here, x_1 and x_2 indicate the start and ending locations of the perturbation strip, respectively. It is seen that the width of the strip is adjusted in accordance with the streamwise wavelength of the associated disturbance while maintaining the same ending location. By definition, having a sufficient resolution is the critical parameter for a proper DNS. Therefore, the computational grid is designed to have comparable resolution with respect to spatial (Pirozzoli et al., 2004; Franko and Lele, 2013) and temporal (Duan and Martin, 2011) DNS studies. The resolution is calculated in wall units with the viscous length scale at the streamwise position corresponding to the peak value of the skin-friction coefficient (Passiatore, 2021), see fig. 3.7.

Table 3.1: Parameters for the simulations. The case names are composed of the first character (“F” and “S”), which represents the first- and second-mode oblique breakdowns, respectively. The ensued letters (“m” and “v”) denote the mass-flux and velocity type of perturbations through the strip, respectively.

Cases	A (% of $\rho_\infty u_\infty, u_\infty$)	β_0 (m^{-1})	f_0 (kHz)	x_1-x_2 (m)	$\Delta x_w^+ \times \Delta y_w^+ \times \Delta z_w^+$
Fm$_{\text{ob}}$	0.495	392.70	21	0.412-0.44	$7.21 \times 0.91 \times 2.52$
Sm$_{\text{ob}}$	0.495	167.55	91	0.43-0.44	$6.35 \times 0.81 \times 5.21$
Sv$_{\text{ob}}$	2	167.55	91	0.43-0.44	$6.39 \times 0.81 \times 5.24$

3.2.4 Data sampling

Time sampling of the variables, $\boldsymbol{Q} = \{\rho u, \rho v, \rho w, \rho E, \rho\}$ as represented in CHOC-WAVES, is performed after six flow through time corresponding to a solution that ensures attenuated initial transient. The primitive variables, $\{u, v, w, p, T\}$ can then be calculated by the density vector in matrix $\boldsymbol{Q}$ together with eq. 2.5. In order to optimize the post-processing cost and the accurate representation of the disturbances inside the boundary layer, slices of $\boldsymbol{Q}$ are acquired at certain streamwise positions and in time. The streamwise wavelength of the fundamental disturbance is the criterion to define the locations in space whereas the lowest frequency of interest sets the sampling frequency, f_s based on the Nyquist theorem (Shannon, 1949). That said, information of the desired signal can be perfectly constructed only if the sampling frequency is two times higher $f_s \geq 2 \times f$. It should also be noted that the present study does not concern sampling a continuous frequency spectrum but rather the discrete sub/super- harmonics of the fundamental frequency, therefore, sampling does not necessarily generate a massive database as in the case of Caillaud (2022). Once the sampling is completed, the eigenvectors (disturbance modes) are obtained via Fourier transformation that is performed in time and in the spanwise direction as Kloker (1993):

$$f'(x,y,z,t) = \sum_{h=-H}^{H} \sum_{k=-K}^{K} \hat{F}_{h,k}(x,y) e^{i(hf_0 t + k\beta_0 z)}, \tag{3.7}$$

Here f_0 is the lowest frequency that can be displayed in the interference spectrum and β_0 is the fundamental transverse wavenumber. In the presentation of the results, the real amplitudes $F_{h,k}$ and phases $\Theta_{h,k}$ of the individual Fourier components are used, which are related to the complex amplitude functions $\hat{F}_{h,k}$ as follows:

$$F_{0,0} = |\hat{F}_{0,0}| = \mathbf{Re}(\hat{F}_{0,0}), \tag{3.8}$$

$$F_{h,k} = 2|\hat{F}_{h,k}| \quad \text{for} \quad h = 0 \quad \text{or} \quad k = 0, \tag{3.9}$$

$$F_{h,k} = 4|\hat{F}_{h,k}| \quad \text{for} \quad h,k \neq 0, \tag{3.10}$$

$$\Theta_{h,k} = \arctan \frac{-\mathbf{Im}(\hat{F}_{h,k})}{\mathbf{Re}(\hat{F}_{h,k})}. \tag{3.11}$$

3.2.5 Validation

The validation has been performed for $\mathrm{Sm_{ob}}$ and $\mathrm{Sv_{ob}}$ due to lower streamwise resolution per disturbance wavelength compared to $\mathrm{Fm_{ob}}$. The designated second-mode wave is resolved with ≈ 37 points in the streamwise direction. Additionally, resolution per wavelength gradually decreases downstream of the perturbation strip since the wavelength of the second-mode instability wave increases along the streamwise direction. However, the effect is negligible since the concerning increase is only by 3% all along its amplified streamwise region based on the linear stability analysis (LSA), see fig. A.3.

The authors utilized transverse velocity disturbance with an amplitude of 2% of u_∞ contrary to the transverse mass-flux perturbation presented in section 3.2.2. In a numerical environment, it is commonplace to use various perturbation methods to trigger transition such as free-stream disturbance, roughness elements, blowing/suction strips, point source, and so on. Nevertheless, when considering injection scenarios, the method of perturbation should be carefully chosen if a realistic approach is sought. The transverse velocity disturbance does not take the non-constant density into account, violating the mass conservation. Although it successfully triggers the transition, Sharma, Shadloo and Hadjadj (2019) highlighted that comparing cases with different thermal boundary conditions might be misleading if the density is not considered. Contradicting the well-known stabilizing effect of the wall cooling on the first-mode, their findings showed a destabilized disturbance when cooling was applied, leading to an earlier transition compared to a heated wall. Nonetheless, for validation, we have initially retained the formula employing the transverse velocity perturbation in $\mathrm{Sv_{ob}}$.

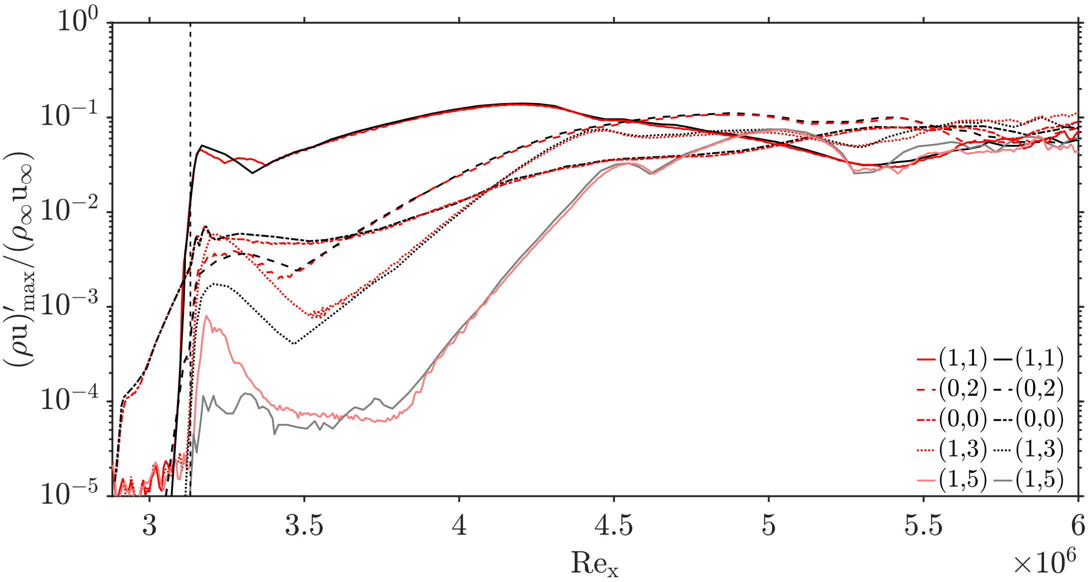

Figure 3.5: Streamwise evolution of maximum modal disturbance amplitudes for $\mathrm{Sv_{ob}}$ (red) and Zhou et al. (2022) (black). Vertical dashed line: perturbation strip center ($Re_x \approx 3.13 \times 10^6$).

Figure 3.5 presents a comparison between the evolution of disturbances obtained from our DNS results and those reported by Zhou et al. (2022). For a better visualization, the results are presented up to $Re_x = 6 \times 10^6$, corresponding to the position beyond the onset of transition based on the minimum C_f value, see fig. A.4. Here, each mode is computed by a time sampling over two fundamental periods, *i.e.* $2 \times f_0$. Following a Fourier analysis in time and the spanwise direction, the maximum amplitude of a selected mode in the wall-normal direction is plotted. The generation of disturbances is similar to the laminar breakdown induced by a first-mode oblique wave instability (Thumm, 1991). The self-nonlinear interaction of the fundamental disturbance leads to the generation of the steady mode (0,2). Furthermore, the non-linear interaction of this steady mode with the fundamental disturbance (1,±1) leads to higher harmonics in the spanwise direction while the self-nonlinear interaction of the fundamental disturbance gives rise to higher harmonics in time, *i.e.* (2,0), (4,0), and so on. The discrepancies in the proximity of the perturbation strip are mainly attributed to the near-field effect, as well as the method employed to search for the maximum amplitude of modes in the wall-normal direction. Additionally, the oscillations in the low-amplitude region are due to the background noise of our solver, influenced by machine precision, numerical schemes, and the parameters selected to initiate the simulation. A higher resolution in the streamwise direction has been shown to decrease this noise-related earlier amplification of the 3-D modes in fig. A.5.

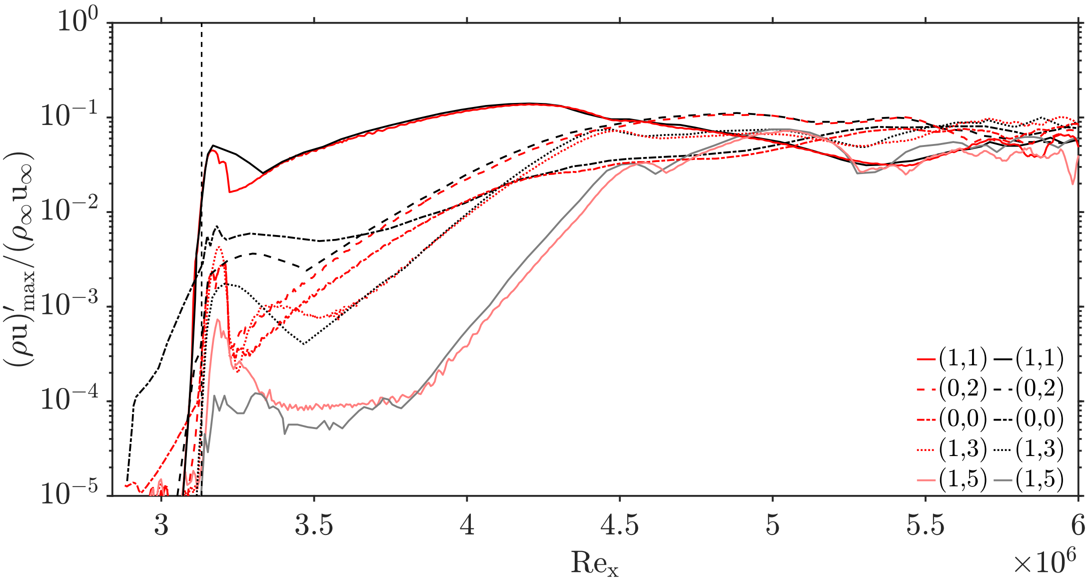

Figure 3.6: Streamwise evolution of maximum modal disturbance amplitudes for $\mathrm{Sm_{ob}}$ (red) and Zhou et al. (2022) (black). Vertical dashed line: perturbation strip center ($Re_x \approx 3.13 \times 10^6$).

From this point on, the transverse mass-flux type of perturbation is retained. Accordingly, the perturbation amplitude is adjusted to account for density variations and ensure zero net-mass injection at the wall. The impact of this modification is observed on the MFD in fig. 3.6. The results closely align with the reference values at approximately $Re_x = 4 \times 10^6$, only after the perturbation amplitude reaches 1% of the maximum amplitude. Despite the alterations in the perturbation method, the influence on the C_f and C_h is found to be insignificant as depicted in fig. A.4.

3.2.6 Oblique breakdown scenarios

Zhou et al. (2022) has provided a thorough analysis of the oblique breakdown scenarios that are induced by oblique wave pairs of the 1^{st} and 2^{nd}-mode instabilities. Hence, to avoid repetition, we will only address the amplification of different perturbation parameters as well as the evolution of non-linearly generated disturbances within the boundary layer along the streamwise direction in the laminar transitional regime. Therefore, an additional DNS case, $\mathrm{Fm_{ob}}$, where the transition is triggered by the 1^{st}-mode instability, as designated by Zhou et al. (2022), is performed.

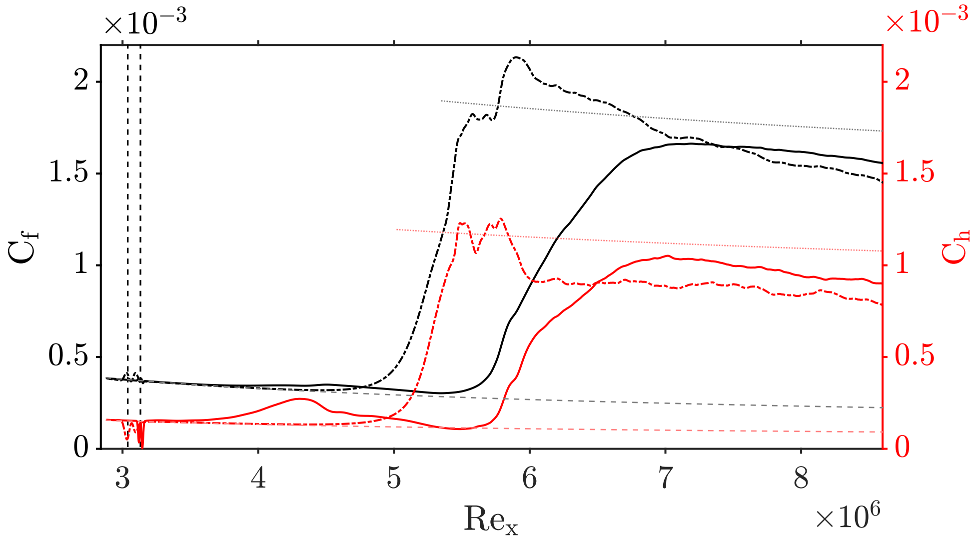

Figure 3.7: Streamwise evolution of skin-friction coefficient and Stanton number for $\mathrm{Fm_{ob}}$ (-·-) and $\mathrm{Sm_{ob}}$ (—). Laminar base flow values (--) and turbulent values (·····). Vertical dashed lines: perturbation strip centers for $\mathrm{Fm_{ob}}$ ($Re_x \approx 3.06\times10^6$) and $\mathrm{Sm_{ob}}$ ($Re_x \approx 3.13\times10^6$).

Before investigating the disturbances, we first examine the evolution of the time- and spanwise-averaged skin-friction coefficient and the Stanton number, denoted as C_f and C_h, respectively. The Stanton number is a dimensionless parameter that quantifies the wall heat-transfer rate and is defined as $C_h = \dot{q}_w/[\rho_\infty u_\infty C_p(T_{rec}-T_w)]$, where $\dot{q}_w$ represents the heat transfer rate from the wall, calculated as $\dot{q}_w = -\lambda_w(\partial\overline{T}/\partial y)|_w$ and C_p is the specific heat capacity at constant pressure. Here, the $(\bar{\bullet})$ denotes time- and space-averaged quantities. Being the recovery temperature at wall for a turbulent boundary layer, T_{rec} is estimated by $T_{rec} = T_\infty[1+r(\gamma-1)/2\times M_\infty^2]$ where $r = Pr^{1/3}$ is the recovery factor for turbulent flows (White and Corfield, 2006). As the definition of the Stanton number is based on the adiabatic wall temperature for turbulent flows, its values, depicted in fig. 3.7, in the laminar and transitional regimes should be interpreted only qualitatively. Additionally, turbulent values of C_f are also included in the figure following (White and Corfield, 2006)'s relation given by:

$$C_f = \frac{0.455}{S^2}\left[ln\left(\frac{0.06}{S}Re_x\frac{\mu_\infty}{\mu_w}\sqrt{\frac{T_\infty}{T_w}}\right)\right]^{-2}, \tag{3.12}$$

where

$$S = \frac{\sqrt{T_{rec}/T_\infty}-1}{\arcsin(A)+\arcsin(B)}, \tag{3.13}$$

and

$$A = \frac{2a^2 - b}{\sqrt{b^2 + 4a^2}}, \quad B = \frac{b}{\sqrt{b^2 + 4a^2}}, \quad a = \sqrt{r\frac{\gamma - 1}{2}M_\infty^2 \frac{T_\infty}{T_w}}, \quad b = \left(\frac{T_{rec}}{T_w} - 1\right). \tag{3.14}$$

Eventually, C_h for turbulent flow is calculated using the Reynolds analogy, expressed as $C_h = C_f/(2Pr^{2/3})$(Reynolds, 1901). While examining fig. 3.7, the onset of transition location is defined as the point corresponding to the minimum value of C_f, which is at $Re_x = 4.46 \times 10^6$ and $Re_x = 5.34 \times 10^6$ for $\mathrm{Fm_{ob}}$ and $\mathrm{Sm_{ob}}$, respectively. The figure reveals that C_f closely follows the laminar base-flow values with a slight hump before reaching the transition onset location in $\mathrm{Sm_{ob}}$. Similarly, a somewhat stronger trend is observed in C_h. Zhou et al. (2022) analyzed the wall heating rate by the viscous dissipation as the sum of the dilatation dissipation, where both pressure and viscous terms play a role, and the work done by shear stress. The peak in C_h in the laminar regime was found to be associated with the dilatation dissipation by the pressure work whereas the shear stress was responsible for the second peak *e.g* mechanism revealed by Zhu et al. (2018). For $\mathrm{Fm_{ob}}$, both C_f and C_h follow the base-flow trends, except near the perturbation strip, until the transition onset location. Further, into the fully-developed turbulent regime, the overshooting of C_f and C_h is observed only for the first-mode oblique breakdown, consistent with the findings of Franko and Lele (2013). The rapid amplification of the steady vortex mode with an initial amplitude higher compared with that of the second-mode induced transition, as illustrated in fig. 3.9, was considered as the primary reason of the observed phenomenon.

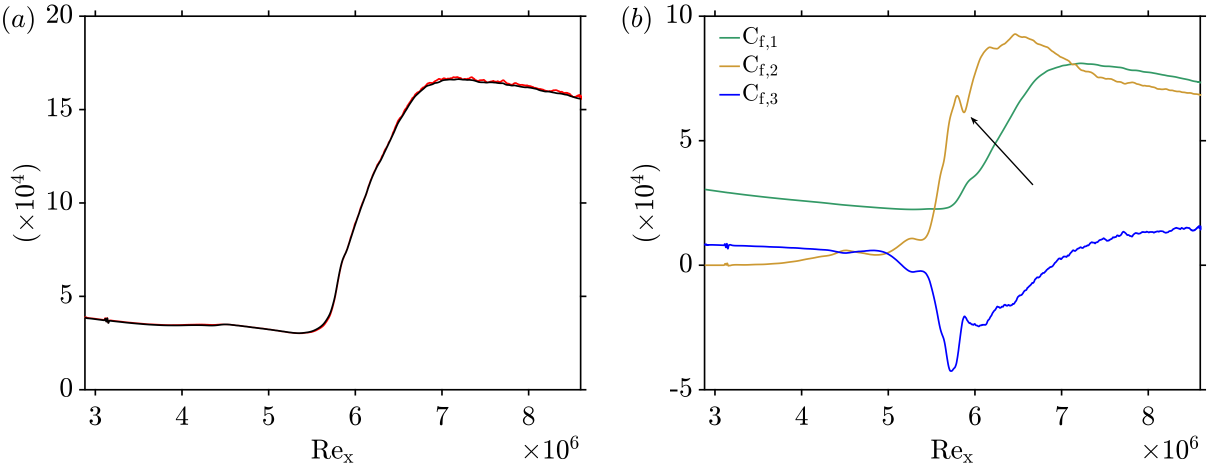

Figure 3.8: (a) Evolution of the skin-friction coefficient in $\mathrm{Sm_{ob}}$ with Renard-Deck decomposition (red) and (b) contribution of the terms in equation 3.15.

A deeper understanding of the C_f evolution requires examining the contribution of different physical mechanisms as in C_h. Thus, Renard and Deck (2016) (RD) identity is used to decompose the skin-friction coefficient in $\mathrm{Sm_{ob}}$. The approach was generalized for compressible channel flows by Li et al. (2019) and further extended to compressible boundary layers by Fan et al. (2019). The RD identity was derived from the mean streamwise kinetic energy budget in an absolute reference frame under the following assumptions: no-slip condition at the wall, statistical stationary in time, statistical homogeneity in the spanwise direction, and no additional body force and is formulated as:

$$
\begin{aligned}
C_f = & \overbrace{\frac{2}{\rho_\infty u_\infty^3}\int_0^\infty \overline{\tau}_{yx}\frac{\partial \widetilde{u}}{\partial y}dy}^{C_{f,1}} + \overbrace{\frac{2}{\rho_\infty u_\infty^3}\int_0^\infty -\overline{\rho u''v''}\frac{\partial \widetilde{u}}{\partial y}dy}^{C_{f,2}} \\
& \underbrace{+\frac{2}{\rho_\infty u_\infty^3}\int_0^\infty (\widetilde{u}-u_\infty)\left[\overline{\rho}\left(\widetilde{u}\frac{\partial \widetilde{u}}{\partial x}+\widetilde{v}\frac{\partial \widetilde{u}}{\partial y}\right)-\frac{\partial}{\partial x}\left(\overline{\tau}_{xx}-\overline{\rho}\widetilde{u''u''}-\overline{p}\right)\right]dy}_{C_{f,3}}
\end{aligned}
\tag{3.15}
$$

where $C_{f,1}$ accounts for the direct effect of viscous dissipation, transforming mechanical power into heat; $C_{f,2}$ is the power converted into turbulent kinetic energy production; and $C_{f,3}$ stands for the spatial growth of the flow which incorporates into streamwise heterogeneity effects. Here, $(\bullet)''$ is the Favre fluctuation while $\widetilde{(\bullet)}$ represents the Favre averaging. For a given variable f, these two operators are linked via $\widetilde{f} = f - f'' = \overline{\rho f}/\overline{\rho}$. It is seen in fig. 3.8a that the RD identity perfectly captures the C_f evolution. The maximum deviation is 2% at $Re_x \approx 5.75\times 10^6$, corresponding to the streamwise location that precedes the jump in C_f. Viscous dissipation dominates over the other terms up to $Re_x = 5.3\times 10^6$. Meanwhile, $C_{f,2}$ exhibits a gradual increase as the fluctuating kinetic energy rises, resulting in the observed hump in C_f during the laminar regime before surpassing $C_{f,1}$. Concurrently, $C_{f,3}$ opposes the $C_{f,2}$ as it increases/decreases while the latter decreases/increases, respectively, expanding the breakdown region until the point indicated by the arrow in fig. 3.8b. Eventually, dissipation-related contributions decrease asymptotically while $C_{f,3}$ experiences a slow, positive increase, contributing to the overall C_f in the turbulent regime.

Figure 3.9 compares the evolution of disturbances in both of the breakdown scenarios. It is observed that the growth rates in $\mathrm{Sm_{ob}}$ are higher than $\mathrm{Fm_{ob}}$ which are in accordance with the LST estimations. Topological investigation of Franko and Lele (2013) revealed that the streaks persist longer in the case of the second-mode-induced transition scenarios, which was attributed to the initially weaker amplitude of the streaks. A similar trend is observed in fig. 3.9, where the steady mode (0,2) in $\mathrm{Sm_{ob}}$ has a two/one order of magnitude lower initial amplitudes in $u'/(\rho u)'$. Furthermore, transition is strongly associated with the breakdown of the vortical structures generated by the steady modes. In case $\mathrm{Fm_{ob}}$, the location corresponding to the maximum amplitude of (0,2) following

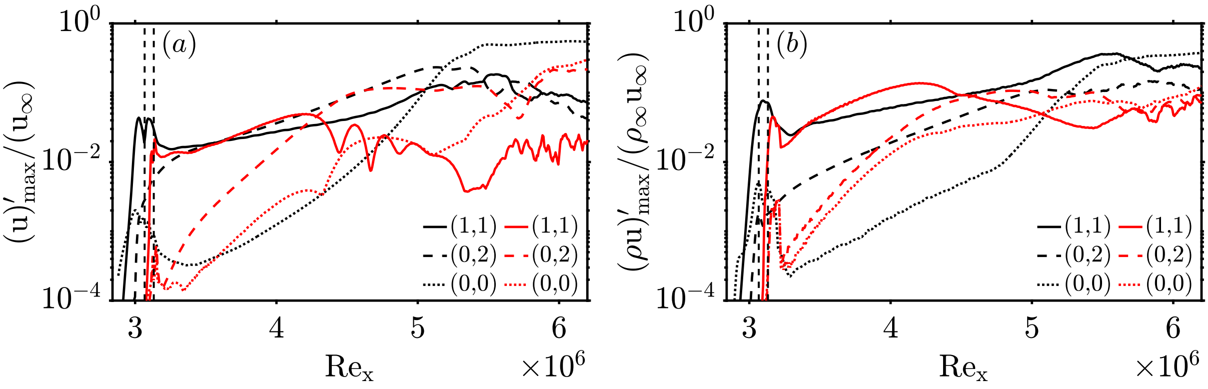

Figure 3.9: Streamwise evolution of maximum modal disturbance amplitudes for Fm$_{ob}$ (black) and Sm$_{ob}$ (red) cases. Vertical dashed lines: perturbation strip centers in Fm$_{ob}$ ($Re_x \approx 3.06 \times 10^6$) and Sm$_{ob}$ ($Re_x \approx 3.13 \times 10^6$).

its amplification is approximately in the range of Reynolds numbers where C_f already starts to shoot up. However, the same analogy does not hold in case Sm$_{ob}$ since the saturation of (0,2) encompasses a large streamwise distance before reaching the transition onset location. Conversely, the earlier transition in case Fm$_{ob}$ compared to case Sm$_{ob}$ can be inferred from the evolution of MFD, which reaches its maximum value shortly before $Re_x = 6 \times 10^6$, while the maximum amplitude of the mode keeps increasing in case Sm$_{ob}$ in both disturbance profiles.

The streamwise evolution of the disturbances within the boundary layer is presented in figs. 3.10 and 3.11 for both breakdown scenarios. In case Fm$_{ob}$, the steady modes (0,2) and (0,4) have their maximum amplitudes almost around the same normalized distance from the wall at the initial three locations for both of the perturbation parameters. Further downstream, the modes experience irregularities due to the strong non-linear transitional regime. However, the steady modes exhibit different wall-normal distributions in case Sm$_{ob}$, as depicted in fig. 3.3. For u', (0,2) goes gradually away from the wall which is followed by (0,4) until around $Re_x = 5 \times 10^6$. Subsequently, (0,4) approaches the wall by increasing its maximum disturbance amplitude. A similar up-and-down movement of the vortical structures was observed in the case of transition induced by the fundamental resonance mechanism over straight (Sivasubramanian and Fasel, 2015) and flared cones (Hader and Fasel, 2017, 2019; Meersman et al., 2018; Chynoweth, 2018). The motion of these vortical structures inside the boundary layer was associated with the generation of the well-known streamwise streak pattern *i.e.* appearing-disappearing-reappearing. Despite the differences between the currently examined oblique breakdown and fundamental resonance scenarios, the up and down movement of the steady modes (0,2) and (0,4) in the u' wall-normal disturbance bears resemblances.

Additionally, a significant difference is observed in the evolution of the MFDs. In case Fm$_{ob}$, the MFD shows modulation starting from the third streamwise location that cor-

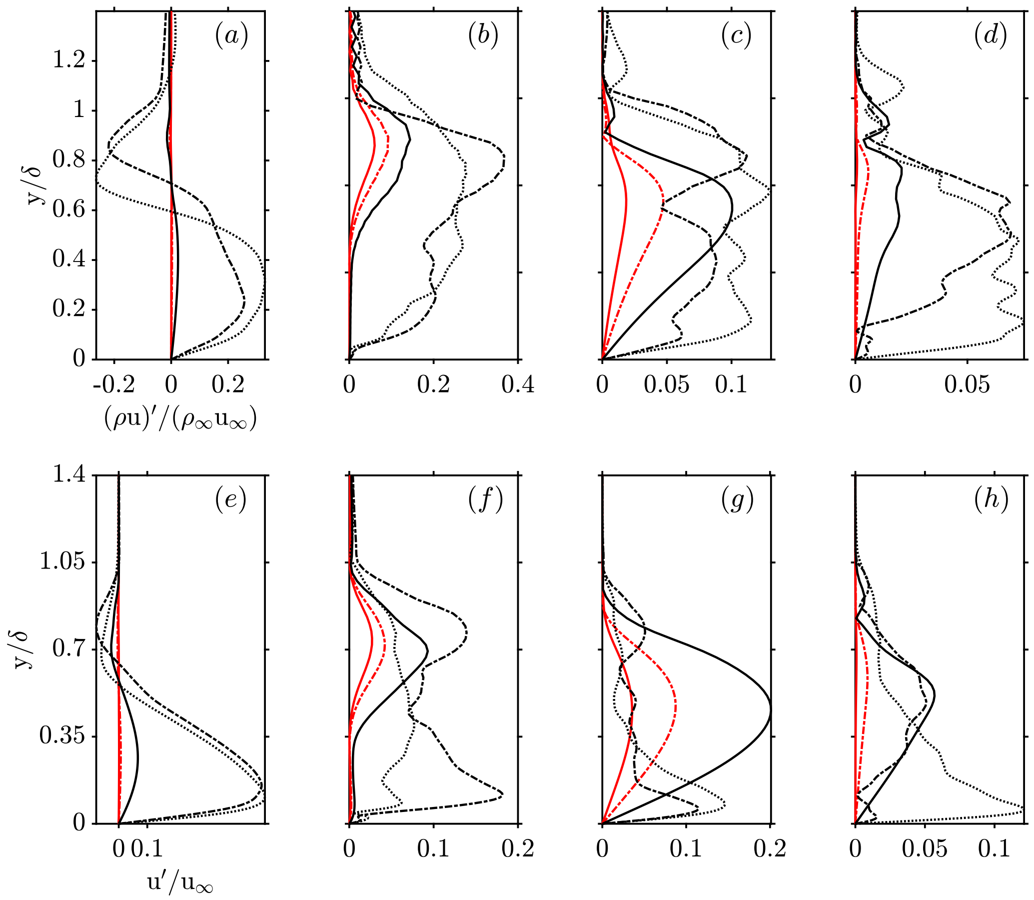

Figure 3.10: Wall-normal distribution of $(\rho u)'$ (top) and u' (bottom) disturbances for case $\mathrm{Fm_{ob}}$: (a-e) MFD, (b-f) (1,1), (c-g) (0,2), and (d-h) (0,4) inside the boundary layer at $Re_x = 3.98 \times 10^6$ (−), $Re_x = 4.51 \times 10^6$ (-··), $Re_x = 4.97 \times 10^6$ (−), $Re_x = 5.5 \times 10^6$ (-··), and $Re_x = 5.76 \times 10^6$ (·····).

responds to approximately around where the rampant increase in C_f and C_h is observed in fig. 3.7. On the other hand, strong modulation of the MFD is observed in u' and $(\rho u)'$ much earlier than the transition location in case of the second-mode disturbance due to its nature as depicted in fig. 3.3.

3.2.7 Turbulence

Accurate resolution of the turbulent flow field with all the small scales requires an adequate grid resolution and computational domain size. According to Poggie et al. (2015), the spanwise length of the domain should be two times greater than the local boundary layer thickness to ensure proper decorrelation in the spanwise direction. Considering the outlet boundary layer thickness in case $\mathrm{Sm_{ob}}$, $(L_x \times L_y \times L_z)/\delta_{out} \approx 72.9 \times 9.1 \times 3.4$ satisfies the asserted requirement. In this section, the attention is given to case $\mathrm{Sm_{ob}}$ since this case will be used as a subject of investigation for transition control in Chapter 6. However, the lower spanwise extent in case $\mathrm{Fm_{ob}}$ as well as the observed earlier breakdown to tur-

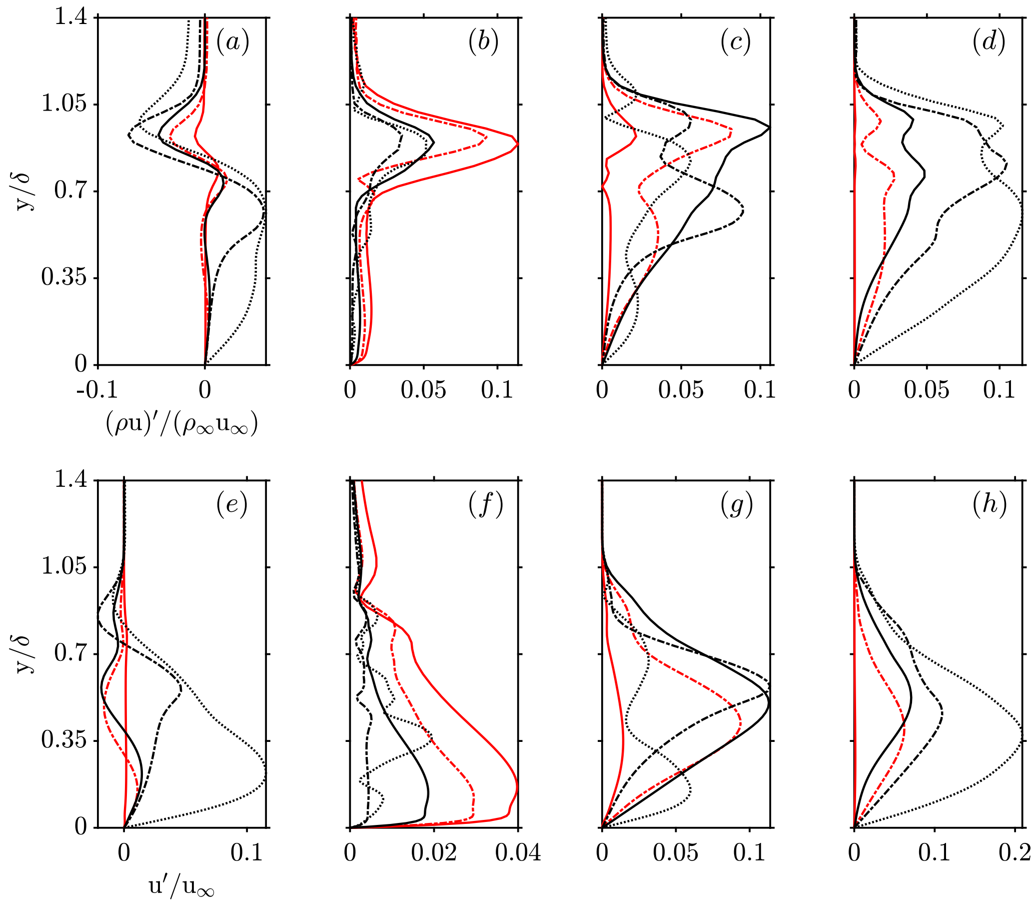

Figure 3.11: Wall-normal distribution of $(\rho u)'$ (top) and u' (bottom) disturbances for case Sm$_{\mathrm{ob}}$: (a-e) MFD, (b-f) (1,1), (c-g) (0,2), and (d-h) (0,4) inside the boundary layer at $Re_x = 3.98 \times 10^6$ (—), $Re_x = 4.51 \times 10^6$ (-··-), $Re_x = 4.97 \times 10^6$ (—), $Re_x = 5.5 \times 10^6$ (-·-), and $Re_x = 5.76 \times 10^6$ (·····).

bulence, resulting in a thicker boundary-layer, makes this case questionable for the matter of decorrelation in the spanwise direction *i.e.* $(L_x \times L_y \times L_z)/\delta_{out} \approx 63.7 \times 7.8 \times 1.3$. Returning to case Sm$_{\mathrm{ob}}$ for the moment, the adequacy of the spanwise extent of the domain can be evaluated using the two-point correlation which is defined as Pirozzoli et al. (2004)

$$R_{\alpha\alpha}(r_z) = \sum_{k=1}^{N_z-1} \overline{\alpha_k \alpha_{k+k_r}}, \qquad k_r = 0, 1, ..., k-1, \tag{3.16}$$

where $r_z = k_r \Delta z$, Δz is the cell-thickness in the $z-$direction, and α stands for the fluctuations of any one of the variables ρ, u, v, w or p. Ensemble averages, indicated by $\overline{(.)}$, are obtained by collecting 562 samples over the time period of $T_0 \approx 340 \times \delta^*/u_\infty$, where δ^* is the local displacement thickness. The sample time falls between 200 and 1200 corresponding to the investigations of Spalart (1988) and Pirozzoli et al. (2004), respectively. Figure 3.12 displays two-point correlations at different wall-normal positions corresponding to the viscous sub-layer, buffer zone, and the logarithmic layer from the wall, respectively. All the variables exhibit a very weak correlation, oscillating around zero at the half spanwise extent, ensuring that the domain is wide enough not to inhibit the turbulence mechanism (Shadloo et al., 2015). A similar investigation has been performed for case $\mathrm{Fm_{ob}}$ and plotted in fig. A.6. Confirming the previously mentioned suspense, the two-point correlation analysis emphasizes the insufficient spanwise length of the domain, where u in the logarithmic zone, w and ρ in the viscous sub-layer and ρ in the buffer zone are not decorrelated entirely at the half-spanwise direction.

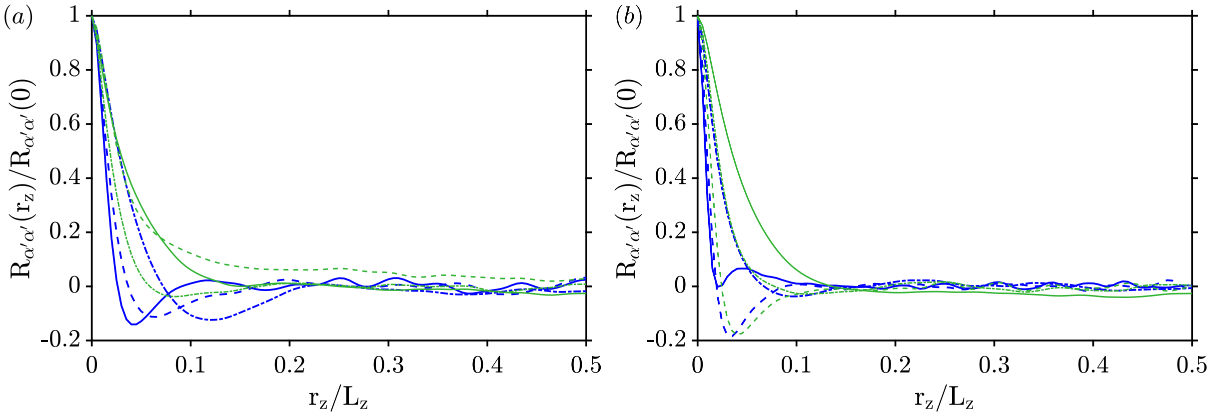

Figure 3.12: Distribution of the two-point correlations in the spanwise direction for case $\mathrm{Sm_{ob}}$ at $Re_x = 8 \times 10^6$ with (a) $\alpha = u$ (blue) and $\alpha = \rho$ (green) and (b) $\alpha = v$ (blue) and $\alpha = w$ (green) at $y^+ = 2.9$ (solid lines), $y^+ = 25.5$ (dashed lines), and $y^+ = 133.3$ (dash-dotted lines).

In order to assess the formation of a fully-developed turbulent boundary layer, the mean flow characteristics averaged both in time and spanwise direction for 3 flow through, are examined. Thus, the streamwise velocity and the wall-normal coordinate are scaled by the friction viscosity and viscous length scale, respectively, as

$$y^+ = \frac{\rho_w u_\tau y}{\mu_w}, \quad u_\tau = \sqrt{\frac{\bar{\tau}_w}{\rho_w}}, \tag{3.17}$$

log-law for incompressible flows are transformed by the Van Driest transform as

$$U_{VD}^+ = \frac{1}{u_\tau}\int_0^{\widetilde{u}} \sqrt{\frac{\widetilde{\rho}}{\rho_w}} d\widetilde{u}^+, \tag{3.18}$$

with $\widetilde{u}^+ = \widetilde{u}/u_\tau$ and superscript $(\bullet)^+$ denotes the scaled variables. Figure 3.13a shows that the transformed mean velocity profile matches the viscous sub-layer *i.e.* $y^+ \leq 5$ and the logarithmic layer, *i.e.* $30 \lessapprox y^+ \lessapprox 100$. While the slope of the logarithmic wall varies only negligibly, the second constant alters significantly with the thermal wall boundary condition (Maeder, 2000; Shahab et al., 2011; Poggie et al., 2015; Hadjadj et al., 2015).

The mean temperature profile can be related to the mean velocity profile through the

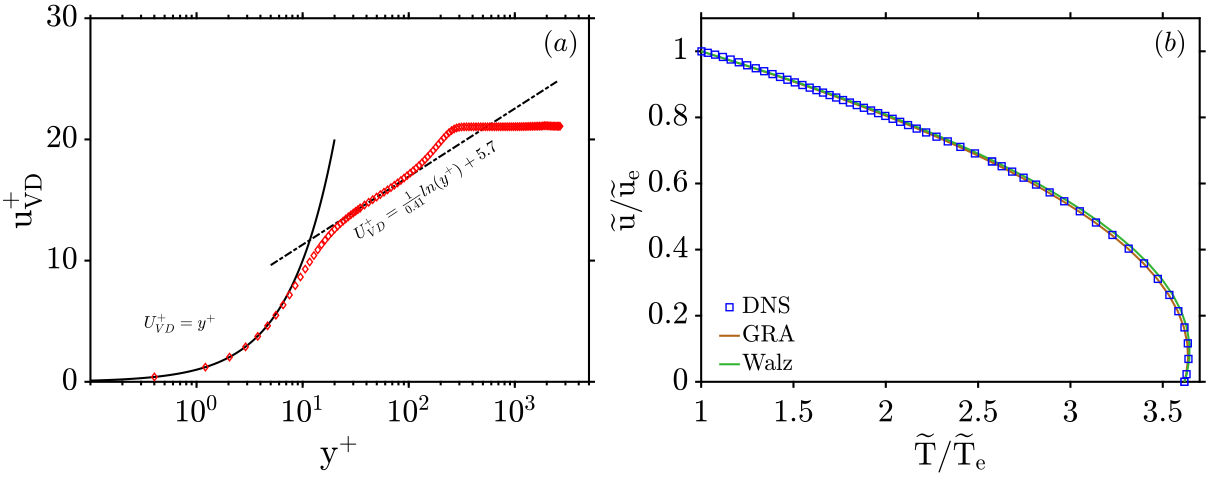

Figure 3.13: Distribution of the Favre-averaged mean quantities in the wall-normal direction at $Re_x = 8 \times 10^6$. (a) van-Driest transformed streamwise velocity and (b) temperature as a function of velocity.

modified Crocco-Busemann of Walz (1969) in zero-pressure gradient (ZPG), flat-plate compressible turbulent boundary layers. In this modified relation, the recovery factor appears in the quadratic velocity term to increase the accuracy

$$\frac{\widetilde{T}}{\widetilde{T}_e} = \frac{T_w}{\widetilde{T}_e} + \frac{\widetilde{T}_{rec} - T_w}{\widetilde{T}_e}\left(\frac{\widetilde{u}}{\widetilde{u}_e}\right) - \frac{\widetilde{T}_e - \widetilde{T}_{rec}}{\widetilde{T}_e}\left(\frac{\widetilde{u}}{\widetilde{u}_e}\right)^2, \tag{3.19}$$

where $\widetilde{T}_{rec}$ is estimated with the boundary-layer edge Mach number, M_e. It was reported that while accurately estimating the adiabatic profiles, Walz's equation deviates significantly for cooled walls Duan et al. (2010). To account for the wall heat transfer, Zhang et al. (2014) introduced a generalized Reynolds analogy (GRA), where $\widetilde{T}_{rec}$ in eq. 3.19 is replaced with $\widetilde{T}_{rg} = \widetilde{T}_e + r_g \widetilde{u}_e^2/(2C_p)$ and r_g is given as

$$r_g = \frac{\widetilde{T}_w - \widetilde{T}_e}{\widetilde{u}_e^2/(2C_p)} + \frac{2C_p}{\widetilde{u}_e}\frac{\partial \widetilde{T}}{\partial \widetilde{u}}\bigg|_w. \tag{3.20}$$

It is seen that the GRA relation reduces to Walz's equation for adiabatic walls. Figure 3.13b plots these two relations for the DNS case. It is seen that Walz's equation slightly overestimates the profiles in the lower half of the boundary layer where GRA accurately captures the DNS data with a maximum deviation $< 1\%$.

3.3 Conclusion

In this chapter, the linear stability solver is tested and proven to accurately estimate the instabilities for the provided base flows. Subsequently, DNS cases are conceived to validate the exploited numerical solver, elaborate different methods of perturbations, and compare oblique breakdown scenarios that are initiated by different types of instabilities. The steady disturbances in transition that is induced by unsteady second-mode disturbance showed resemblances to the topological features of the vortical structures in the fundamental breakdown observed over slender, straight, and flared cones. Ultimately, the turbulent flow field is shown to be reached before the end of the computational domain where the spanwise extent of the domain for the second-mode induced transition is found sufficient to sustain the turbulence mechanism.

Chapter 4

Control of oblique-breakdown in a supersonic boundary layer

Contents

In this chapter, we investigate the application of the streak employment method as a mean to delay laminar breakdown in a supersonic boundary layer. Our study can be regarded as an extension of the research conducted by Sharma, Shadloo, Hadjadj and Kloker (2019), where the range of streak amplitude was roughly studied and only for adiabatic walls. Thus, we conduct a parametric analysis to determine the range of streak amplitudes that effectively suppress flow transition in both adiabatic and isothermal wall conditions. Furthermore, of particular interest is the downstream development of the disturbances in the absence/presence of the streaks within the boundary layer. Most of the results presented in this chapter have been published in Physical Review Fluids (Celep et al., 2022)[6] and were presented at the 8^{th} European Congress on Computational Methods in Applied Sciences and Engineering [7].

---

[6] https://doi.org/10.1103/PhysRevFluids.7.053904

[7] http://www.eccomas2022.org

4.1 Problem setup

4.1.1 Simulation parameters

Simulations are performed for supersonic flows at Mach number $M_\infty = 2.0$, with temperature $T_\infty = 160$ K, velocity $u_\infty = 507.1$ m/s, kinematic viscosity $\nu_\infty = 2.1067 \times 10^{-5}$ m^2/s, pressure $p_\infty = 23.786$ kPa and Prandtl number $Pr = 0.72$. The inlet location, $x_{in} = 4.154$ mm corresponding to the inlet Reynolds number $Re_{x_{in}} = 10^5$, is designated far enough from the leading edge to preclude possible interactions between weakly generated shocks at the leading edge and the disturbance modes of the boundary layer. The length and the height of the domain are $L_x = 55$ mm and $L_y = 10.2$ mm, respectively, while the width of the domain corresponds to the wavelength of the fundamental disturbance, $L_z = 2.153$ mm. Grid is distributed equidistantly in streamwise and spanwise directions with $N_x = 800$ and $N_z = 140$ number of points, whilst grid stretching eq. 3.1 with $\kappa = 3.075$ is used with $N_y = 180$ in the wall-normal direction for accurately capturing the inner boundary layer next to the wall.

4.1.2 Boundary conditions

Supersonic inflow and outflow conditions are applied at the inlet and the outlet. Figure A.7 presents nondimensional velocity and temperature self-similar boundary layer profiles prescribed at the inlet, $Re_{x,in} = 10^5$. As for the rest of the boundaries, periodicity is imposed on the side walls. A slip condition with zero boundary-normal gradient is imposed at the upper boundary. The wall is assumed to be either adiabatic or fixed temperature is imposed *i.e.* $T_w = 0.95 \times T_{rec}$ for cooled wall and $T_w = 1.05 \times T_{rec}$ for heated wall, where $T_{rec} = T_\infty \times [1 + 0.5\sqrt{Pr}(\gamma - 1)M_\infty^2]$. The boundary layer is excited using a blowing/suction strip positioned at the wall, extending from $Re_{x_1} = 2 \times 10^5$ to $Re_{x_2} = 3.32 \times 10^5$. The method of excitation is the transverse mass flux, as introduced in chapter 3 using identical driving formulations. We introduce the same disturbance as in Sharma, Shadloo, Hadjadj and Kloker (2019) with an amplitude of $A = 3.27 \times 10^{-4}$, fundamental frequency $f_0 = 73.87$ kHz, and wavenumber $\beta_0 = 2\pi/\lambda_z = 2.9176 \times 10^3$ m^{-1}, corresponding to the disturbance marked as $(1, \pm 1)$. This modal disturbance is kept the same for all the investigated cases here. Moreover, an additional strip is placed in between $Re_{x_{c,1}} = 1.48 \times 10^5$ to $Re_{x_{c,2}} = 1.96 \times 10^5$, is used to introduce the streamwisely elongated control streaks, such that

$$\dot{m}(x, y = 0, z) = \rho v = A_c \rho_\infty u_\infty f(x) g(z), \tag{4.1}$$

$$f(x) = 2.5983[1 - cos\theta(x)]/\sqrt{27}. \tag{4.2}$$

With a control amplitude $A_c = 1.22 \times 10^{-2}$, while $\theta(x)$ and $g(z)$ formulations of the perturbation strip are retained. It is noted that the mean net flux injected to the domain in both of the strips is zero. Besides, the absence of the time-dependent function highlights the steady nature of the control strip. No-slip condition is applied at the rest of the wall, excluding the permeable regions occupied by the strips. For the cases with isothermal wall condition a minimal amount of heating/cooling, ±5% of T_{rec}, is applied to limit the influence of thermal boundary conditions on the linear stability behavior of the base flow.

Figure 4.1 displays the regarding base flow linear stability diagrams for which the results align well with previous studies, indicating that cooling the entire surface stabilizes the flow resulting in lower N-factors whereas heating destabilizes it strongly. Thus, in the absence of any control mechanism, an identical initial perturbation amplitude would result in an earlier transition for the heated wall scenario compared to the cooled and adiabatic cases. Kneer (2020) pointed out that a 10% cooling rate significantly stabilizes the perturbation, nearly eliminating the concerning disturbance within the domain, thus making the investigation of an additional control mechanism redundant. For simplicity, the details about the performed cases are enlisted in table 4.1.

Table 4.1: Parameters for simulations.

Cases	T_w/T_{rec}	Control Mode	A_c
A5C	1	(0,5)	1.22×10^{-2}
C5C	0.95	(0,5)	1.22×10^{-2}
H5C	1.05	(0,5)	1.22×10^{-2}
$\mathrm{A_T}$	1	—	0
$\mathrm{C_T}$	0.95	—	0
$\mathrm{H_T}$	1.05	—	0

4.2 Results

4.2.1 Evolution of disturbances

Before embarking on the influence of the isothermal boundary conditions on the control streaks, simulations are performed for adiabatic wall condition. The control mode (0,5) is used in A5C, whereas no control is activated in $\mathrm{A_T}$. Figure 4.2 presents a comparison

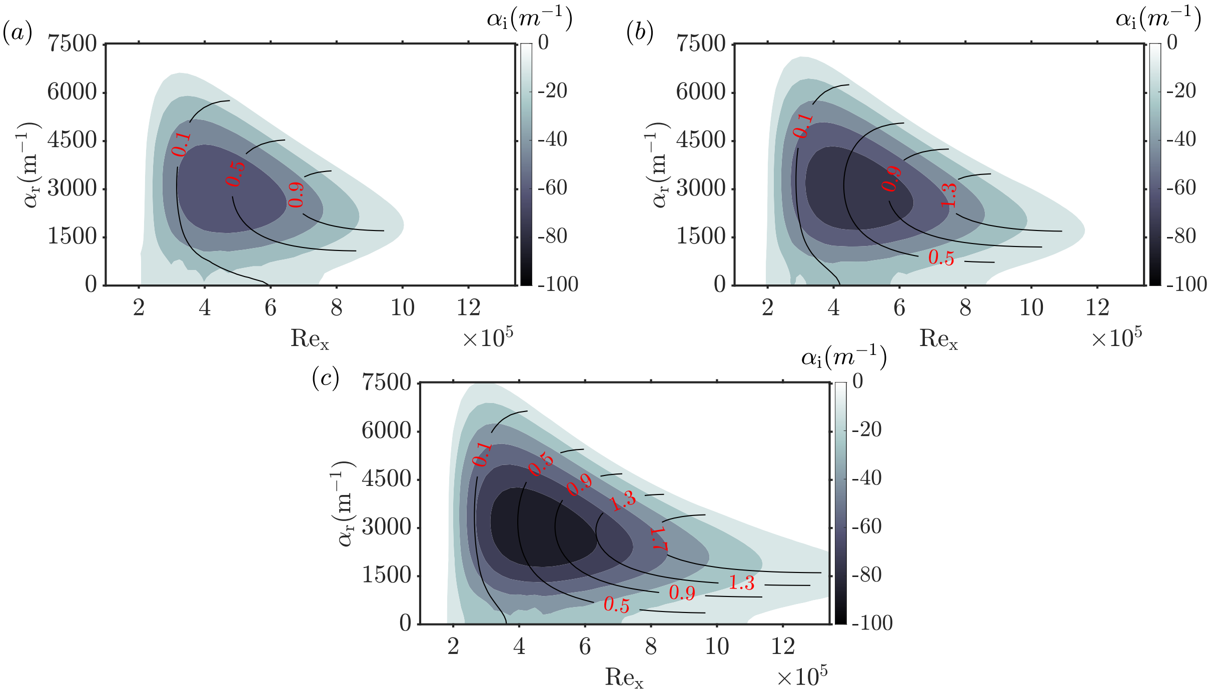

Figure 4.1: Linear stability diagrams for base flows of (a) cooled ($T_w = 0.95 \times T_{rec}$), (b) adiabatic, and (c) heated ($T_w = 1.05 \times T_{rec}$) cases. Integrated growth rates are marked by isocontours.

between these cases for their respective streamwise evolution of the disturbance modes. Hereby, each mode is computed by a time sampling over two fundamental periods. Fourier transform is performed in time and in the spanwise direction, whose maximum value in the wall-normal direction is plotted. It is inferred from fig. 4.2 that the growth rate reduction in the fundamental (1,±1) and the nonlinearly generated steady (0,2) modes illustrates the transition delaying effect of the control streaks. Besides, introducing the control streaks resulted in an earlier generation of MFD (0,0), which plays a vital role in delaying the flow transition (Paredes et al., 2017). In the absence of the control mode (0,5), the chaotic nature of turbulence demonstrates itself in the amplitudes of the fundamental disturbance mode (1,1) and nonlinearly generated (1,3), (1,5) 3-D unsteady modes at around $Re_x = 9 \times 10^5$. Eventually, a saturation sets in for the MFD after having reached an amplitude of ≈35% of $\rho_\infty u_\infty$, whereas an exponential drop is observed in (0,2).

Proceeding to the isothermal conditions, fig. 4.3 illustrates the nondimensional streamwise velocity contour taken inside the boundary layer, at $y/\delta_{in} = 0.517$ in the $x-z$ plane for cases with and without control streaks. Note that the transition to turbulence takes place in all the uncontrolled scenarios. Therefore, a comparison between these cases shows, although not explicitly in fig. 4.3, the stabilizing/destabilizing effect of cooling/heating, as predicted by LST in fig. 4.1. In the presence of the streaks, the formation of streamwisely elongated steady vortices is represented by the superposition of

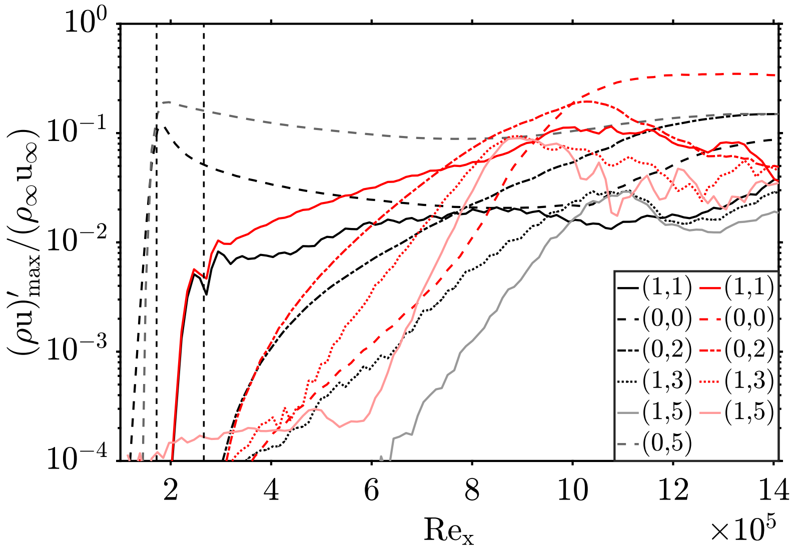

Figure 4.2: Streamwise evolution of the maximum disturbance amplitudes for A_T (red) and A5C (black). Vertical dashed lines: control ($Re_x \approx 1.72 \times 10^5$) and perturbation ($Re_x \approx 2.66 \times 10^5$) strip centers.

streaky modes (0,2), (0,4), (0,6), and so on, observed in A5C and C5C in the downstream direction. They regulate the flow field by transporting high-momentum fluid from the external boundary layer to the near-wall regime. Thereafter, the flow stays laminar in A5C and C5C cases, whereas the streaks break down to turbulence as they are strongly amplified in H5C.

For a better understanding of the propagation of disturbances and their possible breakdown mechanisms, the streamwise evolution of various disturbance modes is plotted in fig. 4.4. For uncontrolled scenarios, exponential growth of the fundamental disturbance (1,1) is followed by fully-nonlinear behavior indicating a flow transition farther downstream in all the cases. The earliest in the heated (H_T) and the latest in the cooled (C_T) are marked, as shown in fig. 4.4a. For a given streamwise location, it is seen that both the maximum disturbance amplitude and the growth rate of any mode are the highest for H_T and the lowest for C_T once the modes reach significant amplitudes. After having generated, the steady mode (0,2) drives the flow to transition with the contribution of (1,1) and nonlinearly generated modes, *i.e.* (1,3), (1,5), and so on. Towards the outlet, the MFD attains the highest amplitude, indicating a strong mean flow deformation due to transition to turbulence. When the control strip is activated, see fig. 4.4b, the presence of the control mode (0,5) leads to an earlier generation of the MFD in all cases, as aforementioned. It is seen that the MFD carries approximately the same value until around a point where (0,2) gains significant amplitude. Then, H5C deviates from the cases at around $Re_x = 9 \times 10^5$. Here, the steady mode (0,2) will be used for marking the presence of transition in the domain since sudden changes in MFD could also be an indication of

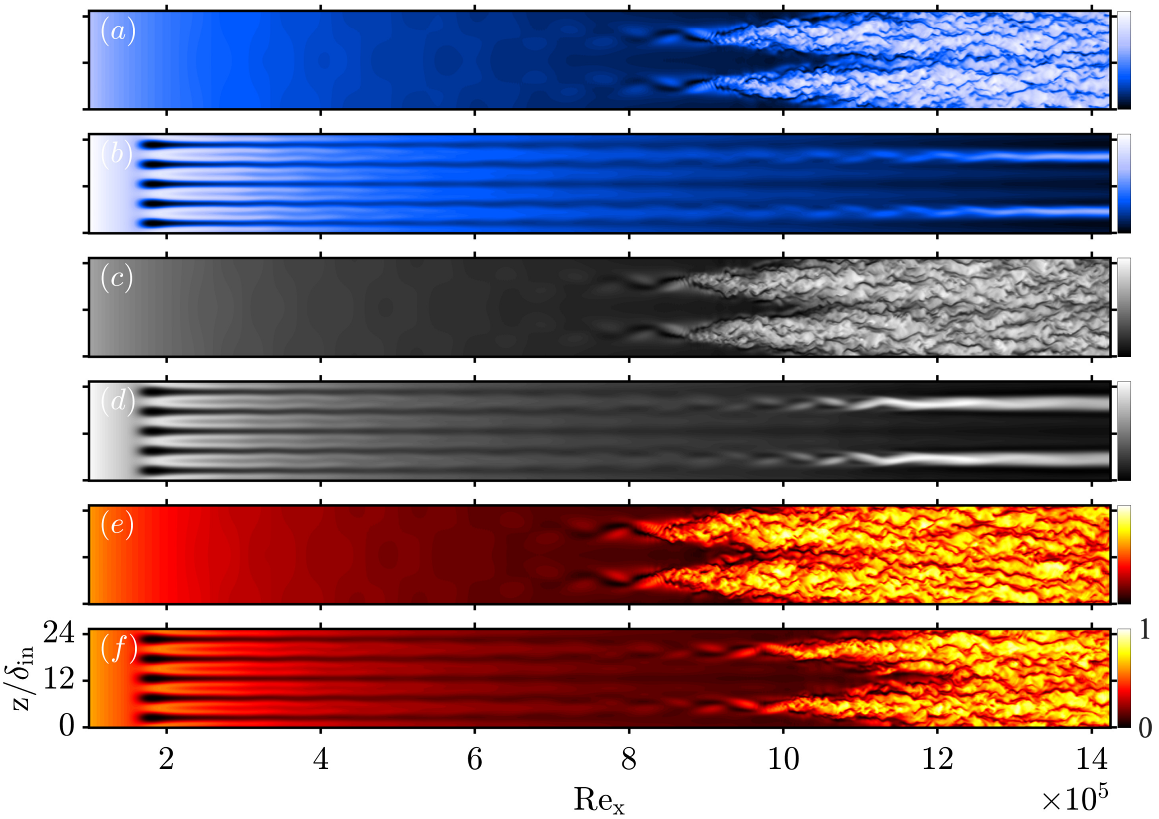

Figure 4.3: Contours of $U^* = (u - u_{min})/(u_{max} - u_{min})$ at $y/\delta_{in} = 0.517$ in an instantaneous flow-field for (a) C_T, (b) C5C, (c) A_T, (d) A5C, (e) H_T, and (f) H5C scenarios. The spanwise is nondimensionalized by the δ_{in} for the adiabatic flow.

sharp but regular deformation of the flow field. In doing so, it could be deduced that the laminar flow regime is preserved until the end of the computational domain in A5C and C5C, whereas the transition in H5C is postponed to downstream without being able to completely avoid it. Moreover, the fundamental mode (1,1) for the cooled scenario (C5C) is fully attenuated after having reached its maximum value at around $Re_x = 8 \times 10^5$. This is a definite sign of flow staying laminar.

In addition to the maximum amplitude of various disturbances, the shape of a disturbance with respect to the wall-normal direction should also be looked at to understand its evolution inside the boundary layer. Prior to the isothermal boundary condition, the nonlinear transitional regime is elaborated for the adiabatic wall condition. The most significant modes in the oblique breakdown are plotted and a comparison between A_T and A5C scenarios is provided in fig. 4.5. The evolution of the MFD in the absence and the presence of the control mode, the latter leading to an earlier generation of the MFD compared to the former, is depicted in fig. 4.5a. Although the maximum amplitude of the MFD rapidly decreases from 12% to 3% of $\rho_\infty u_\infty$ shortly after its generation to the first streamwise location, the maximum amplitude of the mode remains substantially higher than that of A_T until $Re_x = 8 \times 10^5$. In case A_T, the MFD attains a positive

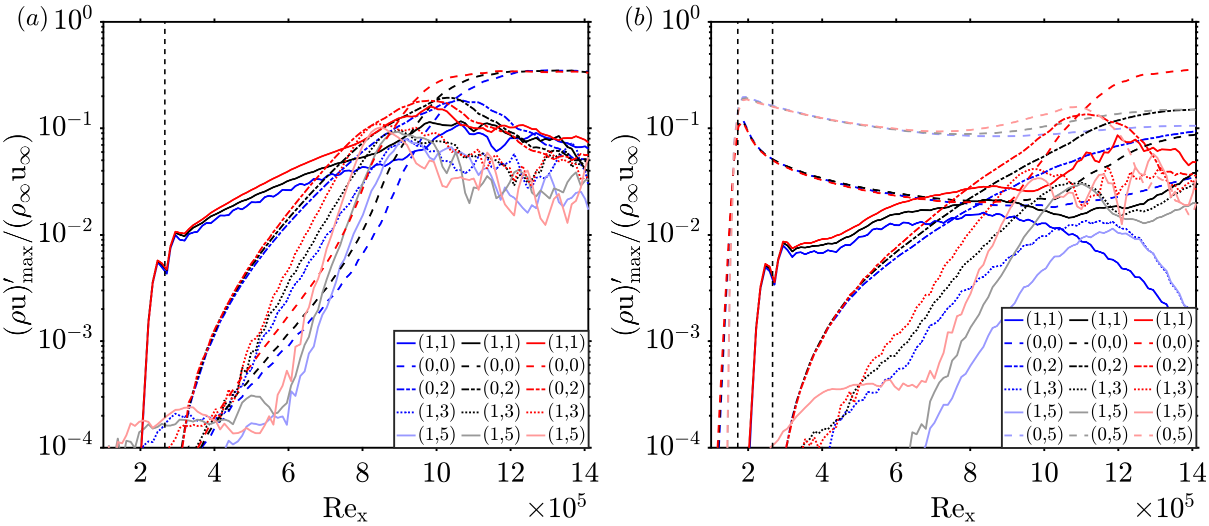

Figure 4.4: Streamwise evolution of the maximum disturbance amplitudes for (a) uncontrolled cases: C_T, A_T, and H_T and (b) controlled cases: C5C, A5C, and H5C. Cooled (blue), adiabatic (black), and heated (red) scenarios. Vertical dashed lines: control ($Re_x \approx 1.72 \times 10^5$) and perturbation ($Re_x \approx 2.66 \times 10^5$) strip centers.

amplitude near the wall making the mean flow profile fuller as the onset of transition is reached at $Re_x = 8 \times 10^5$. Conversely, the MFD in A5C stabilizes the flow from its generation, creating a fuller velocity profile in the boundary layer with positive values in the inner boundary layer and negative values in the outer two-thirds of the boundary layer. Notably, the distortion of the control streaks (0,5) is more prominent in the upper half of the boundary layer. As we move downstream, the MFD is overtaken by the steady mode (0,2) at around $Re_x = 8 \times 10^5$ in A5C. Subsequently, as the steady modes (0,2), (0,4), (0,6), etc., transform into streamwise elongated vortices, the positive shape of the profile expands within the boundary layer, generating an anti-symmetric profile centered at about half of the boundary layer thickness. The fundamental mode (1,1) in A_T consistently grows following an exponential modulation, carrying its maximum amplitude at around $y/\delta = 0.5$ until $Re_x = 8 \times 10^5$, as shown in fig. 4.5b. At this point, the flow undergoes transition, significantly modifying the shape of the disturbance profile and generating a second hump in the inner half of the boundary layer. In the presence of the control streaks (0,5) in A5C, the growth of the fundamental mode in each fluid layer is attenuated. However, this regression is compensated once the fundamental mode starts growing again after $Re_x = 1.1 \times 10^6$, although its maximum amplitude does not exceed 2.3% of $\rho_\infty u_\infty$ in A5C. The strong damping of the fundamental mode is evident in both the growth rate and the amplitude profile of the steady mode (0,2), as shown in fig. 4.5c. Although its growth rate is reduced with the presence of the control streaks, it still persistently increases in amplitude until the end of the computational domain in A5C. Contrary to the shift of the profile closer to the boundary layer edge in A_T, the profile approaches the wall with an increased maximum disturbance amplitude in AC5. Having obtained significant amplitudes at $Re_x = 10^6$, it leads to the generation of two high-velocity streaks with the contribution of its integer multiples i.e. (0,4), (0,6) and so on, see fig. 4.3b. On the other hand, the profile of $\mathrm{A_T}$ is distinctly distorted at $Re_x = 10^6$, exhibiting fully-nonlinear effects followed by flow transition further downstream. Additionally, fig. 4.5d represents the control mode (0,5) with two additional streamwise positions. As the evolution progresses, the amplitude of the control mode in each fluid layer decreases until $Re_x = 6 \times 10^5$. Moving downstream, the control mode starts to grow, and its profile becomes distorted in the inner half of the boundary layer after $Re_x = 8 \times 10^5$ due to the presence of high-amplitude steady modes.

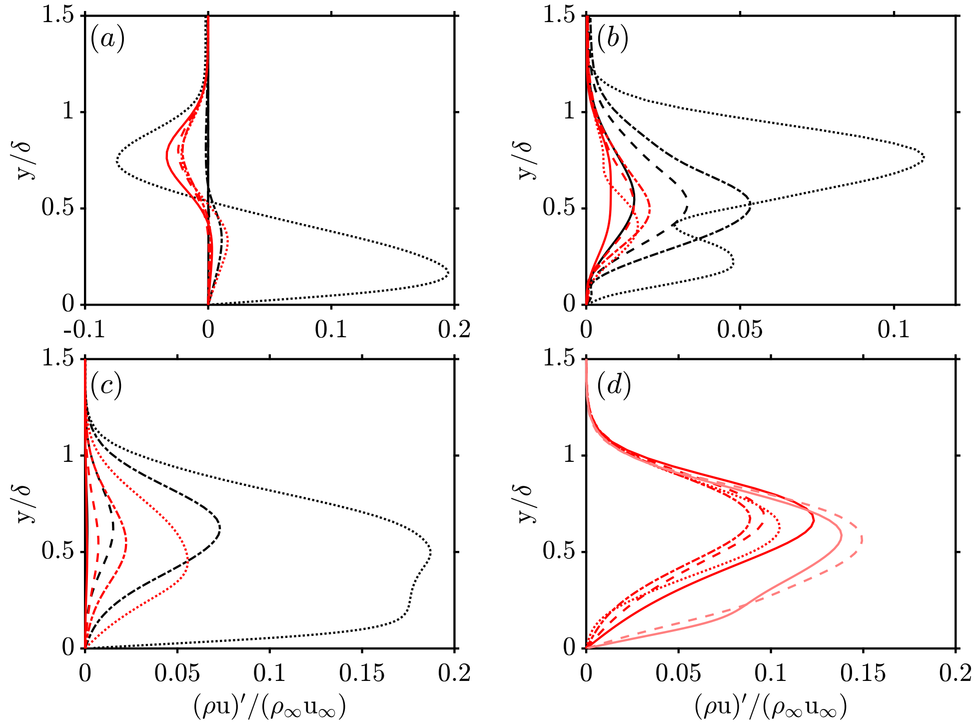

Figure 4.5: Disturbance amplitude of (a) MFD, (b) (1,1), (c) (0,2), and (d) (0,5) for $\mathrm{A_T}$ (black) and A5C (red) obtained at $Re_x = 4 \times 10^5$ (—), $Re_x = 6 \times 10^5$ (--), $Re_x = 8 \times 10^5$, (-·-) and $Re_x = \times 10^6$ (·····) along the wall-normal direction. Two additional locations are given (d) at $Re_x = 12 \times 10^5$ (—) and $Re_x = 14 \times 10^5$ (--). δ denotes the local boundary-layer thickness.

Regarding the influence of the isothermal wall condition on the disturbances, fig. 4.6 depicts the shape evolution of various modes within the boundary layer obtained at three different streamwise locations for cooled, adiabatic, and heated boundary conditions. The extraction is done at points where the deviations between the cases become significant. Utilizing non-linear parabolic-stability-equations (PSE), Chang and Malik (1994) asserted that negative values of the MFD indicate an energy transfer extracted from the mean flow and transferred to the unsteady disturbances. It is seen that the MFD retains only positive values near the wall in all cases, yielding a fuller velocity profile as the flow goes towards the transition to turbulence, denoting the energy transfer from the disturbances to mean flow, see fig. 4.6a. Also, it is observed that $\mathrm{H_T}$ is the first scenario bearing relatively high negative values at $Re_x = 9 \times 10^5$ in the upper boundary layer compared to the cooled and adiabatic cases. This corresponds to the position at which the MFD starts to dominate the fundamental disturbance (1,1), where the flow enters the late non-linear regime (Mayer, Von Terzi and Fasel (2011)), as seen in fig. 4.4a. The MFD maximum gets closer to the wall with the positive region shrinking and approaching the wall. Meanwhile, the region of negative values occupies two-thirds of the boundary layer corresponding to its outer part. This trend is observed consistently in each scenario. With transition to turbulence, the MFD attains its maximum disturbance amplitude, representing the shape change of the mean-velocity profile from laminar to turbulent, induced by the action of the Reynolds stresses. The evolution of the fundamental mode (1,1) shows that its peak amplitude appears closer to the boundary-layer edge as the wall is heated, whereas it gets closer to the wall if it is cooled down, as shown in fig. 4.6c. As soon as the onset of transition is reached, the profiles are distorted due to strong non-linear effects. As for the steady mode (0,2), based on the terminology of Mayer, Von Terzi and Fasel (2011); Tumin et al. (2007), the point corresponding roughly to a position where (0,2) and (1,3) reach the same order of amplitude indicates the end of the early transition regime. The distortion in its wall-normal profile can be interpreted as the inception of strong non-linear interactions in the flow domain. Besides, cooling diminishes the growth of the mode, causing it to have a lower maximum amplitude, whereas its influence is reversed in the inner boundary layer at $Re_x = 7 \times 10^5$, as shown in fig. 4.6e. Further downstream, the shape of the profiles gets bumpier in the lower half of the boundary layer, earliest in the heated case, and latest in the cooled scenario, indicating strong non-linearities.

When the control streaks are employed, the MFD exhibits a similar trend, as depicted in fig. 4.6b, to what was observed in fig. 4.6a for AC5. The significant difference is observed in H5C where the MFD reaches almost 15% of amplitude at $Re_x = 11 \times 10^5$, undergoing transition. The combined stabilizing effect of cooling and the induced control mode is evident in the damping of (1,1) mode as the flow proceeds downstream, as shown in fig. 4.6d. Not only the maximum value of the disturbance amplitude but also the entire profile experience regression. However, in H5C, flow transition occurs with a maximum amplitude that grows in the streamwise direction. On the other hand, in A5C, there is an exponential amplification in the fundamental mode until it saturates at around $Re_x = 7 \times 10^5$. Having reached saturation with around 2% of $\rho_\infty u_\infty$, the maximum amplitude remains constant until $Re_x = 10^6$, after which it experiences an exponential increase until the end of the domain. As long as the flow remains laminar, the maximum

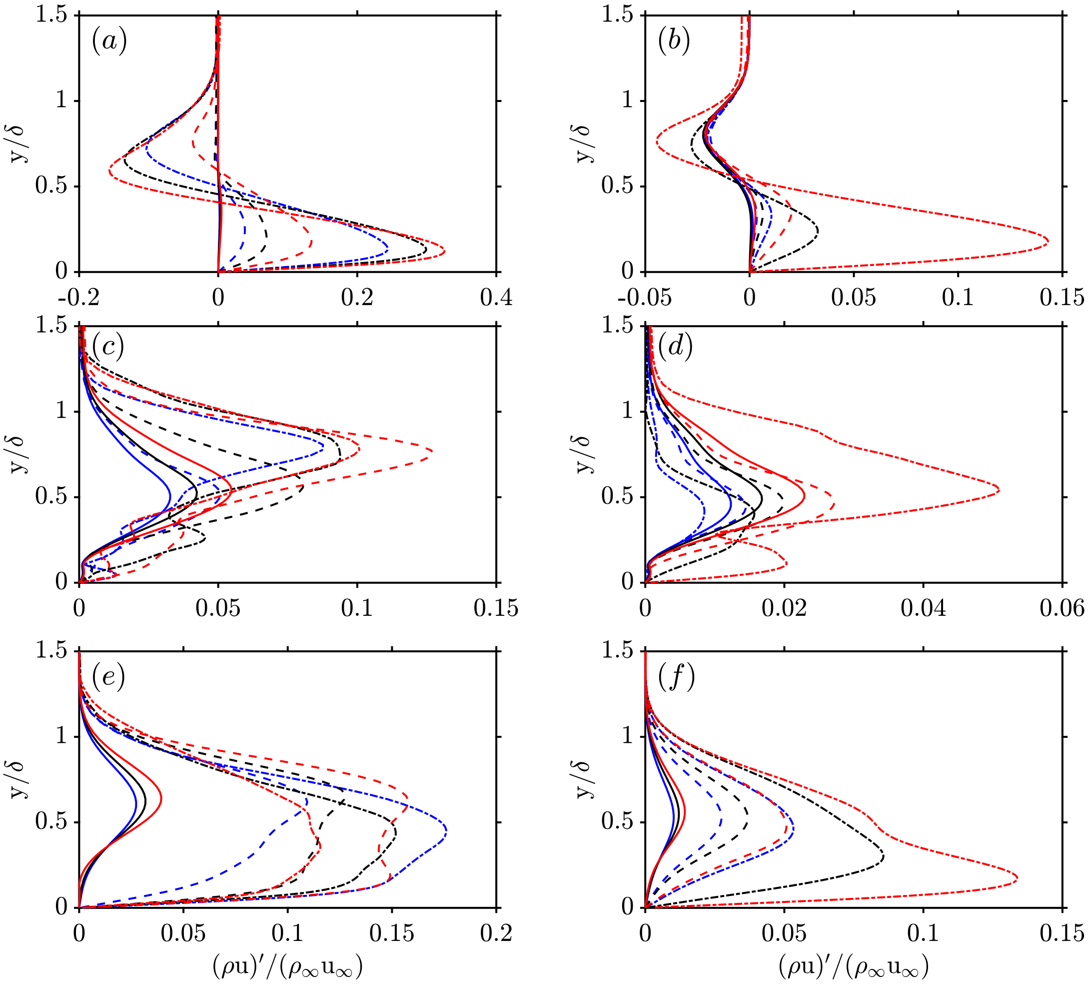

Figure 4.6: Disturbance amplitude of (a,b) MFD, (c,d) (1,1), and (e,f) (0,2) along the wall-normal direction at $Re_x = 7 \times 10^5$ (—), $Re_x = 9 \times 10^5$ (- -), and $Re_x = 11 \times 10^5$ (- · -). Cooled (blue), adiabatic (black), and heated (red) scenarios. $\mathrm{C_T}$, $\mathrm{A_T}$, and $\mathrm{H_T}$ (left column) and C5C, A5C, and H5C (right column).

disturbance amplitude of the steady vortex mode (0,2) gets closer to the wall as the flow develops, regardless of the wall boundary condition, see fig. 4.6f. Its active role in regulating the flow field gets stronger as it gets closer to the wall, with a maximum disturbance amplitude reaching up to 14% and 8% for AC5 and C5C, respectively. Further downstream, a hump starts to form in the outer half of the boundary layer in all scenarios. The disturbance profile of H5C becomes significantly distorted once the flow becomes turbulent. Experiencing a saturation, A5C preserves its maximum amplitude for a longer streamwise distance in (0,2), as shown in fig. 4.4b, while its profile attains the highest amplitude in the entire boundary layer compared with C5C and H5C. Besides, the wall cooling reduces the amplitude growth of the steady mode and keeps its maximum always at a higher location in the wall-normal direction compared to A5C and H5C before the transition occurs in the heating scenario.

4.2.2 Mean-flow field

The skin-friction coefficient along the streamwise direction is illustrated in fig. 4.7. Stabilizing effect of wall cooling, is more explicitly marked for control-free scenarios in fig. 4.7a. Having traced the laminar C_f trend, transition onset is observed the earliest in $\mathrm{H_T}$, and the latest in $\mathrm{C_T}$. When the flow breaks down to turbulence, the order is inversed in terms of the magnitude of the turbulent C_f. The reason is attributed to the higher velocity gradient of the cooled scenarios in the wall-normal direction. Since the dynamic viscosity scales up with temperature which is inversely proportional to the density, wall cooling results in a lower air kinematic viscosity, so does a thinner boundary layer compared to the heated cases. Although the dynamic viscosity is lowered with the temperature decrease, a higher velocity gradient due to lower boundary layer thickness is dominant and causes a higher C_f. In the presence of the control streaks, the kinks corresponding to the location of the control strip, are generated due to control streaks, see 4.7b. All the profiles follow the laminar C_f, to a streamwise location corresponding to about $Re_x = 8 \times 10^5$ from which a prominent deviation can be observed in H5C. This deviation corresponds to a region between $Re_x = 8.5 \times 10^5$ and $Re_x = 10^6$ in fig. 4.3f, where a formation of two high-velocity streaks becomes visible in addition to the control streaks. Since they rapidly break down to turbulence further downstream, their formation in H5C is relatively discrete compared to the adiabatic counterpart (A5C), see fig. 4.3d. The concerning breakdown mechanism exhibits its impact on the C_f with a drastic augmentation at around $Re_x = 10^6$ for H5C. Contrarily, these non-linearly generated streamwise vortices last longer in the streamwise direction and reach the end of the computation domain for C5C and A5C. The boundary layer gets thinner in the proximity of these streaks which results in a steeper velocity gradient at the wall in the case of A5C. Consequently, the C_f undergoes a slight augmentation around $Re_x = 10^6$, followed by a decrease with a slope similar to that in the laminar regime while the flow remains laminar until the end.

Figure 4.8a shows the streamwise evolution of the Stanton number for isothermal scenarios. Heat transfer is found to be strongly influenced by the control streaks which alter the C_h in favor of the C5C as opposed to uncontrolled cases. However, they all converge until the earliest transition onset which is observed in $\mathrm{H_T}$. From this point forth, a significant variation between the scenarios reveals itself. It is observed that the rate of heat transfer becomes five to six times higher for $\mathrm{C_T}$ than C5C as a result of a marginally steeper temperature gradient near the wall in the absence of the control mechanism as shown in fig. 4.9. As for H5C, following a delayed transition in the presence of the control streaks, an initial reduction ensued by an increase towards downstream where St

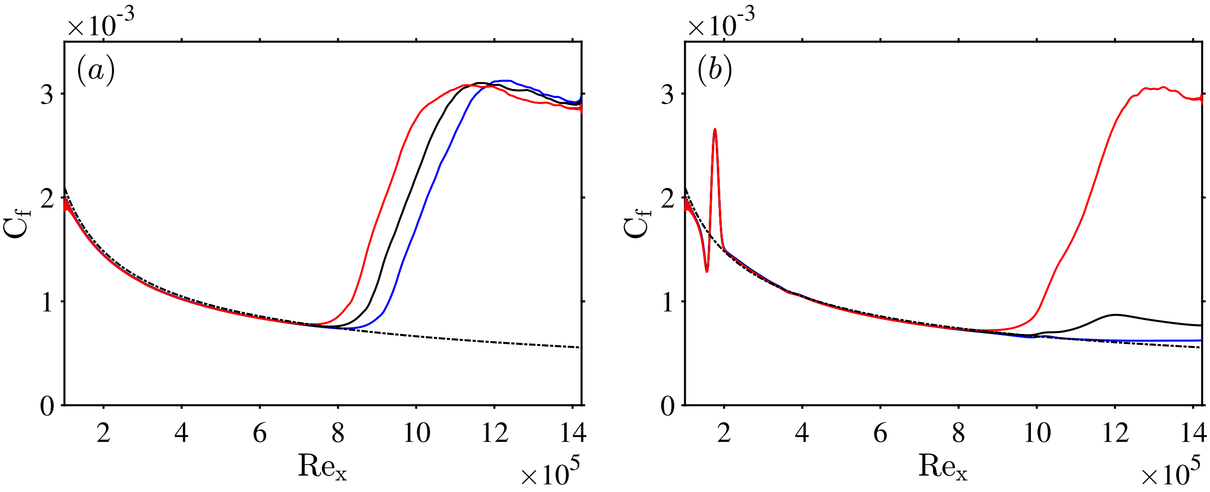

Figure 4.7: Streamwise evolution of skin-friction coefficient for (a) uncontrolled ($\mathrm{C_T}$, $\mathrm{A_T}$, and $\mathrm{H_T}$) and (b) controlled cases (C5C, A5C, and H5C) where cooled (blue), adiabatic (black), and heated (red). Skin-friction coefficient for laminar flow (--) estimated by White and Corfield (2006) $C_f = 0.664/\sqrt{Re_x}$.

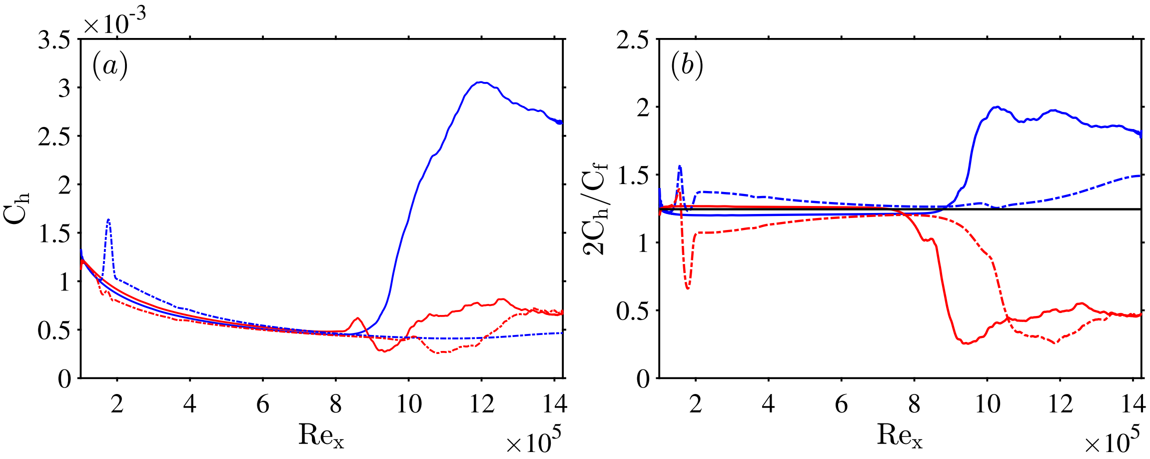

Figure 4.8: Streamwise evolution of (a) Stanton number and (b) Reynolds analogy factor ($2C_h/C_f$). $\mathrm{C_T}$ (—), C5C (-·-), $\mathrm{H_T}$ (—), H5C (-·-), and $Pr^{-2/3}$ (—) .

meets its uncontrolled counterpart of $\mathrm{H_T}$ towards the end of the domain. Furthermore, a direct relation between the shear stress and the heat transfer is provided by the Reynolds analogy factor $2C_h/C_f = Pr^{-2/3}$, which serves as a useful tool in practical applications to estimate the heat transfer rate through the skin-friction coefficient. All curves converge, rather slower in the uncontrolled cases, to the $Pr^{-2/3}$, see fig. 4.8b. In the sequel of the transition onset, the cases drift apart with a decrease in the heated scenarios and a rise in $\mathrm{C_T}$. Further downstream, the increase both in C_h and C_f to the formation of two-high velocity streaks increases the Reynolds analogy factor in C5C.

In an attempt to consider the influence of the boundary-layer growth in the streamwise direction, knowing that the boundary layer thickness is proportional (Schlichting and Gersten, 2016) to $\sqrt{x}$, fig. 4.9 is plotted with respect to $y/\sqrt{x}$. It is seen that employing

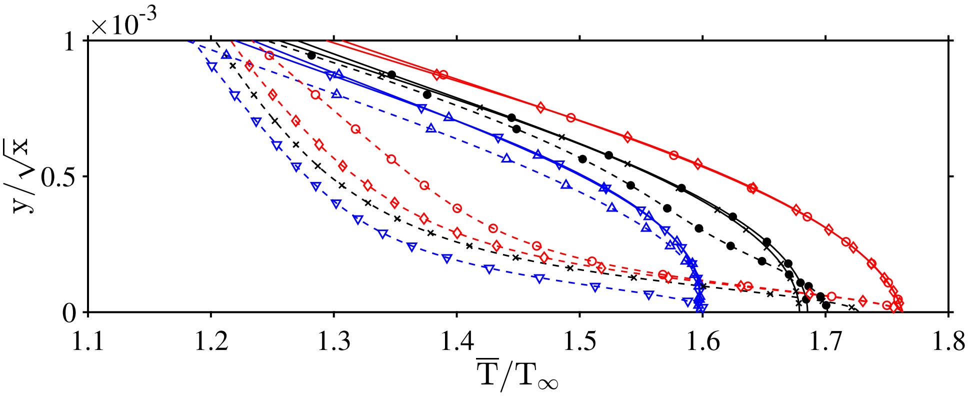

Figure 4.9: Temperature profiles at $Re_x = 4.3 \times 10^5$ (solid lines) and $Re_x = 12.57 \times 10^5$ (dashed lines). C_T (△), C5C (▽), A_T (×), A5C (●), H_T (○), and H5C (◇).

the velocity streaks decreases the temperature gradient at the wall and retains the laminar temperature profile for C5C at $Re_x = 12.57 \times 10^5$. When no control is applied, C_T attains a turbulent profile with identical wall temperature as the rest of the cooled scenarios, but with a steeper temperature gradient. This gradient as well as the definition of $T_{rec} = f(\sqrt{Pr})$ are the reasons for observing a tremendous increase in the C_h in fig. 4.8a. As for the heated cases (H5C, H_T), it is seen that the presence of the control streaks does not carry any significance at the wall, but they modify the temperature profile at the first streamwise location. Given that $Re_x = 12.57 \times 10^5$ corresponds to the turbulent regime in both H_T and H5C, they present steeper temperature profiles. Adiabatic cases on the other hand show different trends compared to the isothermal scenarios. The presence of velocity streaks generates a marginally higher wall temperature at the wall at $Re_x = 4.3 \times 10^5$, which increases downstream following the formation of high-velocity streaks with a modified temperature profile. Once the control mechanism is discarded, the flow becomes turbulent with a wall temperature equal to the adiabatic wall temperature of turbulent flow at the second streamwise location, $Re_x = 12.57 \times 10^5$. Kneer (2020) reported similar behaviors for adiabatic and cooled wall scenarios.

Figure 4.10 represents the mean flow temperature and velocity profiles in order to scrutinize the stabilizing influence of the MFD (0,0) stated by Paredes et al. (2017). It is seen that the flow is accelerated near the wall with the induction of the streaks, whereas it decelerates in the outer region of the boundary layer. Thus, a fuller velocity profile is provided indicating a more stable flow (Cousteix, 2005). Contrarily, the temperature field exhibits an opposite behavior such that the flow is slightly cooled down in the inner boundary layer, whereas it is heated in the outer part. However, there exists a region where the fluid is heated in the adiabatic scenario close to the wall as illustrated in fig. 4.9 with respect to A_T. While the role of heating/cooling continuously changes in the wall-normal direction in terms of the velocity profile, it is decidedly seen that H5C has

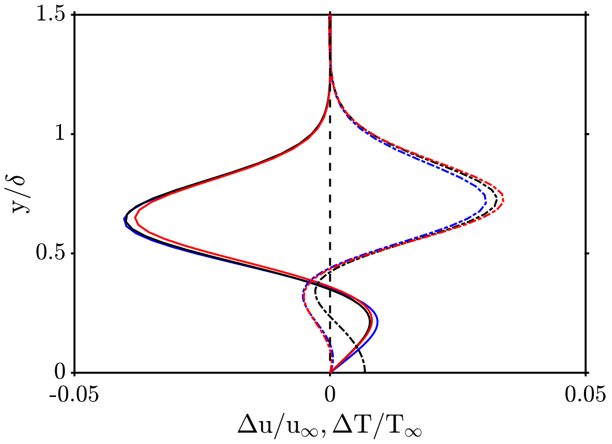

Figure 4.10: Mean temperature $\Delta T = \overline{T} - T_b$ (dash-dotted lines) and mean streamwise velocity profiles (solid lines) $\Delta u = \overline{u} - u_b$ at $Re_x = 3 \times 10^5$ for C5C (blue), A5C (black), and H5C.

the highest heating and the lowest decelerating impact on the fluid in the outer boundary layer.

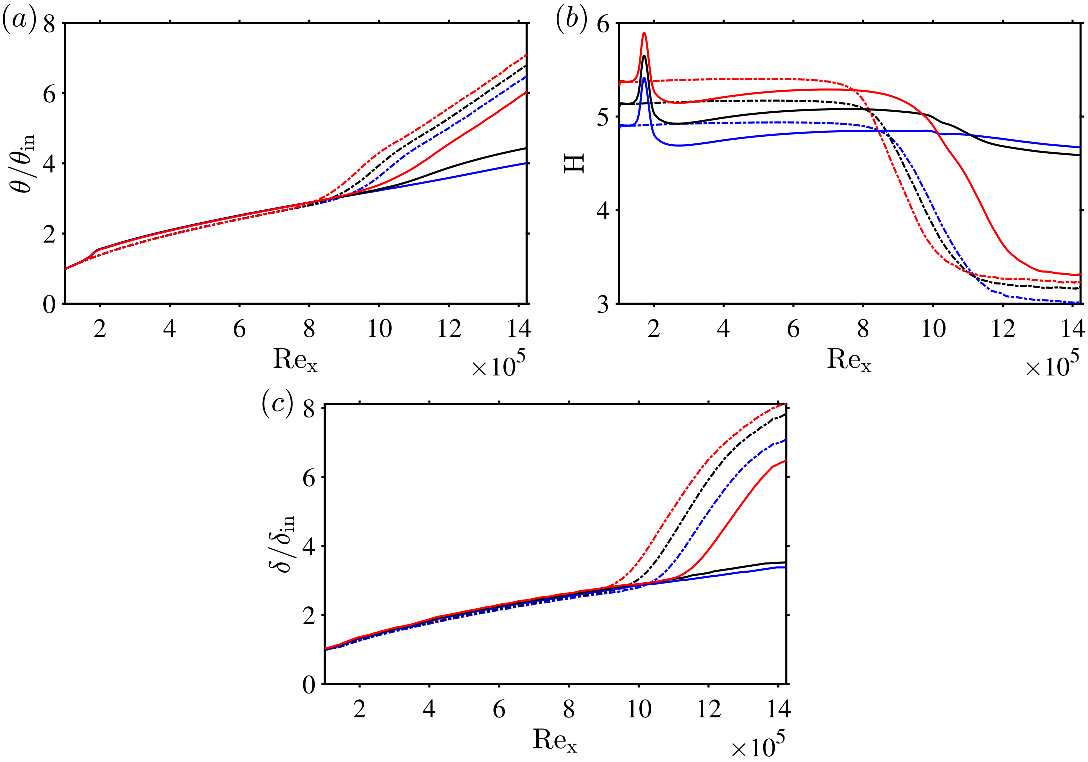

Figure 4.11: Streamwise evolution of (a) momentum thickness, (b) shape factor, and (c) boundary-layer thickness. Uncontrolled (dash-dotted lines) and controlled cases (solid lines) wherein cooled (blue), adiabatic (black), and heated (red).

The streamwise evolution of the momentum thickness is presented in fig. 4.11a. All the profiles follow a smooth trend in the laminar region except for the location where the earlier appearance of the MFD becomes evident due to the control streaks. It is seen that the growth rate increases drastically once the flow becomes turbulent in uncontrolled and

H5C cases. Besides, the highest value is obtained always for the case experiencing the earliest transition. Cooling has been one of the common techniques to achieve a fuller velocity profile for air-flow stabilization (Crouch, 1999) which consequently decreases the shape factor. The presence of the control mode (0,5) results in an instantaneous decrease in the shape factor at the beginning of the domain as shown in fig. 4.11b. In that way, the transition is avoided in A5C and C5C, whereas the shape factor of H5C decreases further downstream with regard to $\mathrm{H_T}$ that indicates a delay in the heated scenarios. Despite having a fuller velocity profile in the boundary layer, the presence of the streaks resulted in thickening the boundary layer, see fig. 4.11c.

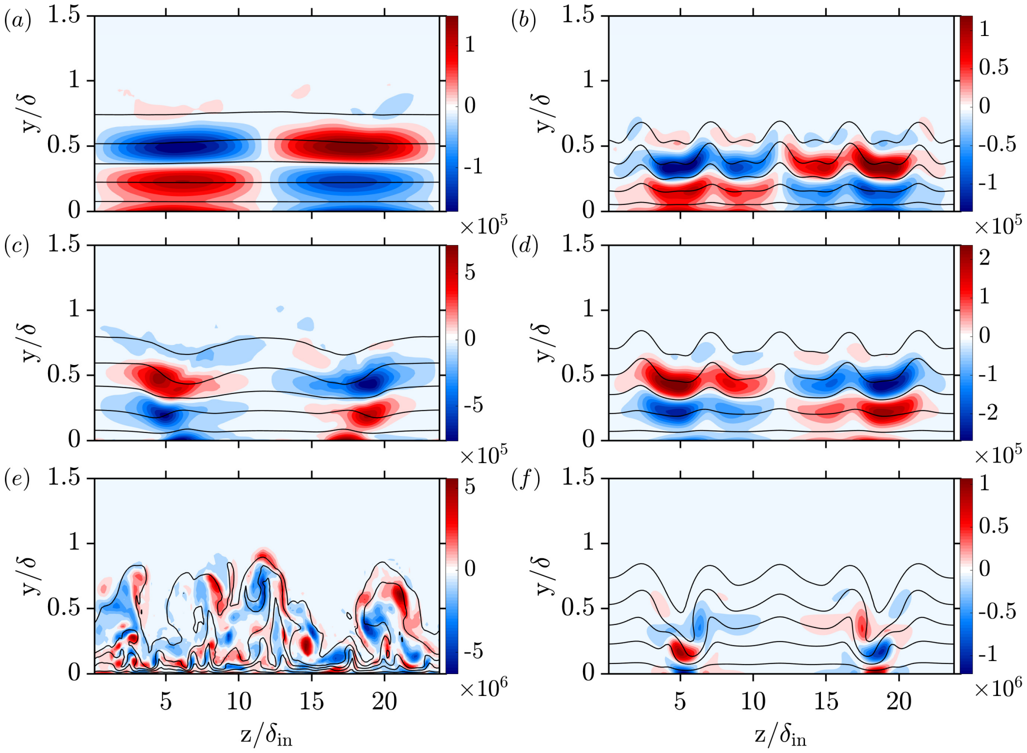

Figure 4.12: Streamwise vorticity (ω_x) contours of an instantaneous flow-field at various streamwise positions for $\mathrm{A_T}$ (left row) and A5C (right row). The black solid lines are isolines of the streamwise velocity component with 0.1, 0.3, 0.5, 0.7, and 0.9 $\times u_\infty$.

Figure 4.12 shows the streamwise vorticity contours obtained at various downstream positions for $\mathrm{A_T}$ and A5C. Structural flow development is analyzed only for the adiabatic scenario after having concluded that weak heating/cooling does not exhibit a significant impact on the general flow structures. Concerning the uncontrolled case, the evolution of the disturbances is accompanied by the opposite signs of vorticity values due to their obliquely-running nature, are depicted in fig. 4.12a at $Re_x = 5 \times 10^5$. Further downstream, the steady mode (0,2) having maximum disturbance amplitude of 6% of $\rho_\infty u_\infty$, see fig. 4.4a, shows its impact on the flow by prominently distorting the streamwise vorticity field in fig. 4.12c. At around $Re_x = 9 \times 10^5$, the onset of the transition appears in the domain, leading the flow to transition where a fully-nonlinear regime prevails in the field resulting in the formation of small near-wall structures as illustrated in fig. 4.12e. Once the control streaks are applied, the strong flow field regulation, visualized in the $x-z$ plane in fig. 4.3d, can also be seen for the vorticity field in fig. 4.12b with some deformation in the inner boundary. Following the growth of the disturbance modes, deformation is reflected in the vorticity field at $Re_x = 8\times10^5$ as seen in fig. 4.12d. Further downstream, high deformation due to strengthened steady modes is observed with its clear physical domination of the flow field in fig. 4.12f. The fluid retains its regular structure with the formation of two high-velocity streaks, whilst the boundary layer properties remain akin to those of the laminar flow until the end of the computational domain.

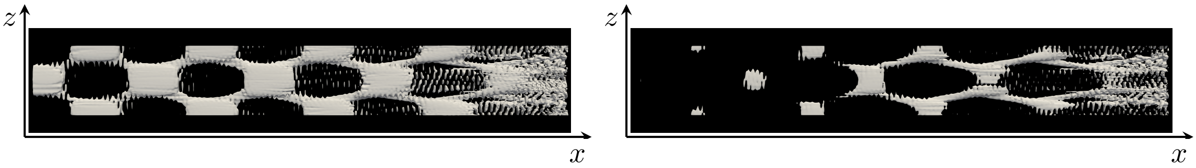

(a) $Q = 0.01\% \times Q_{max}$ at $Re_x = 5-9\times10^5$. (b) $Q = 0.05\% \times Q_{max}$ at $Re_x = 5-9\times10^5$.

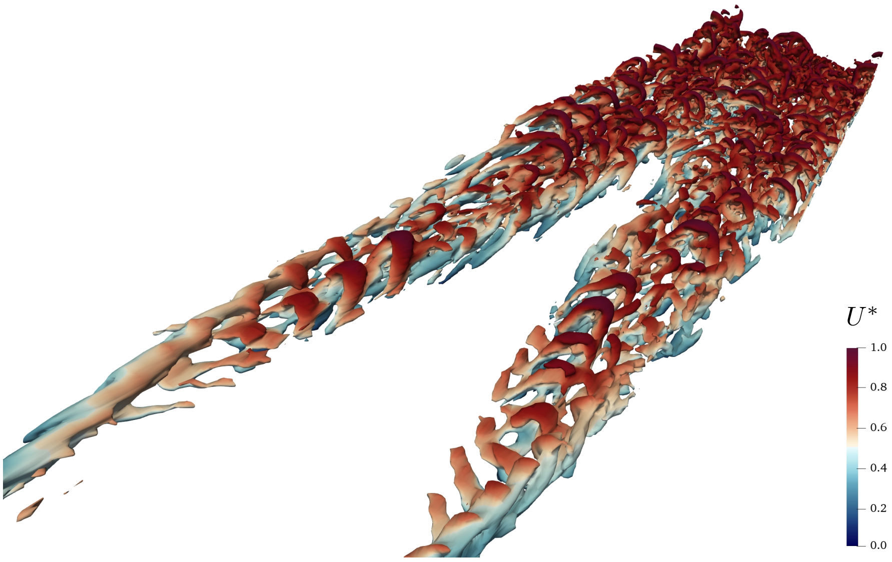

(c) $Q = 0.5\% \times Q_{max}$ at $Re_x = 8-12\times10^5$.

Figure 4.13: Isosurfaces of $Q-$criterion for $\mathrm{A_T}$ with $U^* = (u-u_{min})/(u_{max}-u_{min})$. (a) and (b) Top view. (c) 3-D view.

The vortical structures developed in $\mathrm{A_T}$ are identified by the $Q-$criterion (Hunt et al., 1988) in fig. 4.13a (Q is the second invariant of the velocity gradient, which defines the vortical regions where the vorticity magnitude is larger than that of the strain rate). Figure 4.13a illustrates the superposition of the fundamental oblique wave traveling in the opposite spanwise directions. The formation of a honeycomb-like structure is seen as reported by Bestek et al. (1994). Moving downstream, its shape is distorted due to the steady modes that are rapidly growing. When the Q criterion is increased, the vortical structures generated due to steady modes become visible, see fig. 4.13b. To accurately display the transitional and turbulent regimes, a 3-D flow-field visualization is used in fig. 4.13c. Proceeding to the onset of transition at around $Re_x = 8 \times 10^5$, the formation of ring-shaped vortices is marked in the figure. Further downstream, the identification of hairpin vortices is a clear evidence of a fully-turbulent boundary layer in the domain. A similar study is carried out for A5C to reveal the influence of the control streaks in the flow development. The presence of the control streaks regulates the flow field by damping the disturbances in figs. 4.14a and 4.14b. Besides, an increase in $Q-$criterion highlights the formation of the steady modes in the domain. With the 3-D view of the flow field, it is observed that no transitional regime is reached by the end of the domain, see fig. 4.14c. Therefore, a successful transition delay is proven to be sustained once again in the presence of the control mode (0,5).

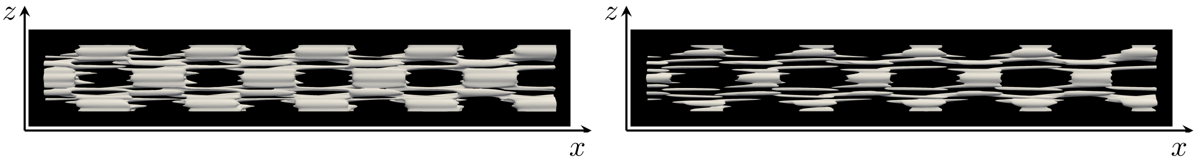

(a) $Q = 0.5\% \times Q_{max}$ at $Re_x = 5 - 9 \times 10^5$. (b) $Q = 5\% \times Q_{max}$ at $Re_x = 5 - 9 \times 10^5$.

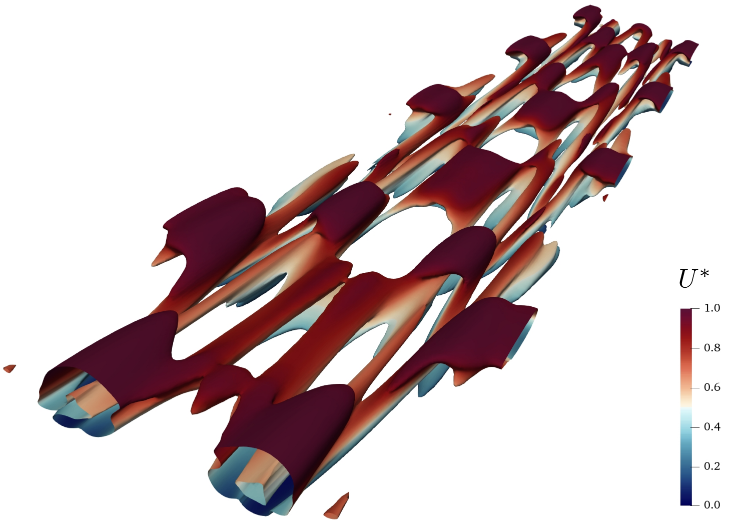

(c) $Q = 0.1\% \times Q_{max}$ at $Re_x = 1 - 1.42 \times 10^6$.

Figure 4.14: Isosurfaces of $Q-$criterion for A5C with $U^* = (u - u_{min})/(u_{max} - u_{min})$. (a) and (b) Top view. (c) 3-D view.

4.2.3 Parametric study

Preceding the effective transition delay of the current strategy, the question as to what extent this method could be applied should be answered. In that way, an extensive parametric study is carried out for adiabatic and weakly cooled/heated walls for a wide range of the control strip amplitudes.

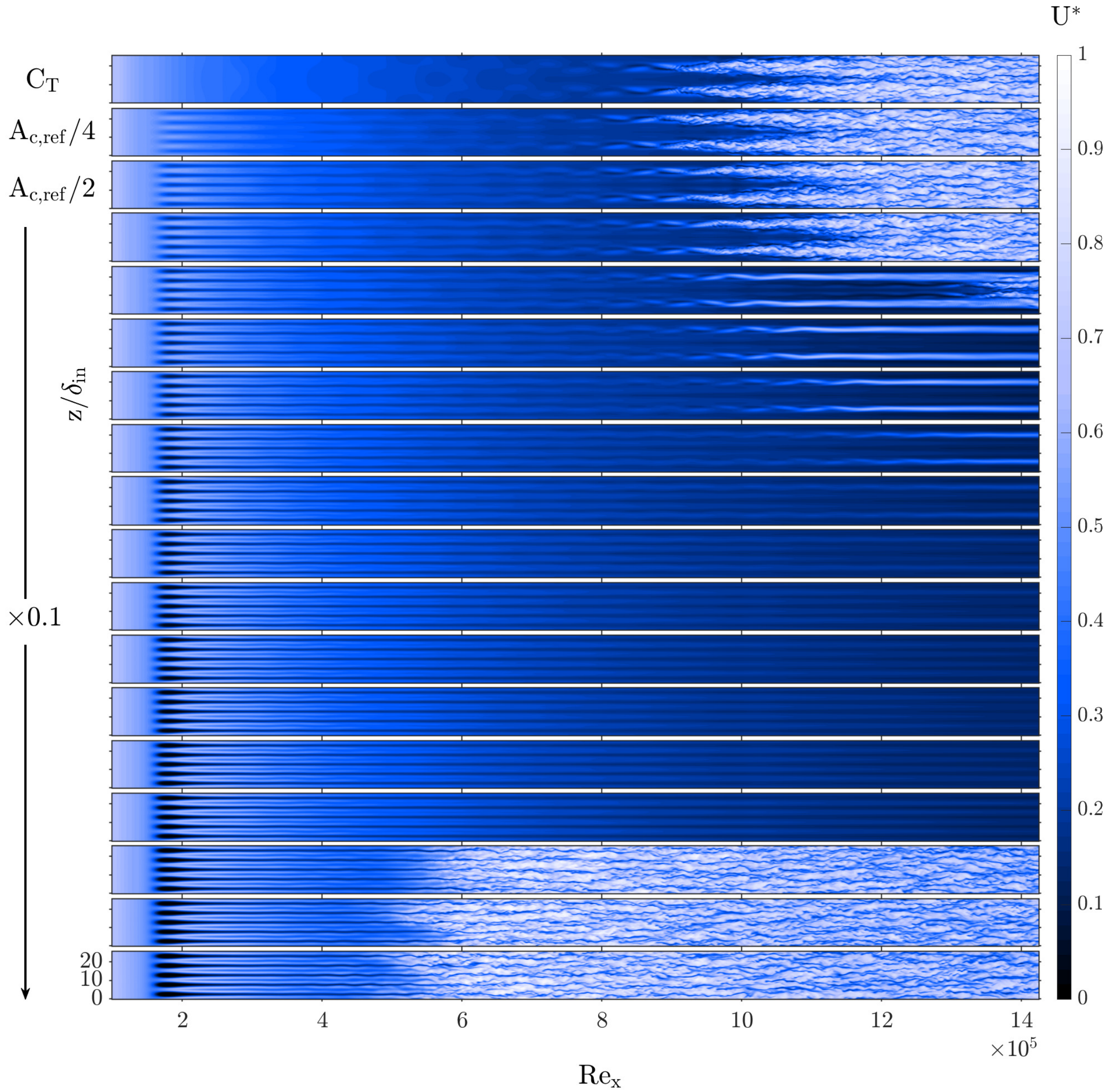

Figure 4.15: Contours of $U^* = (u - u_{min})/(u_{max} - u_{min})$ at $y/\delta_{in} = 0.517$ in an instantaneous flow-field for various control amplitudes in the cooled scenarios. From top-to-bottom, the first one designates C_T whereas the trailing two are the controlled cases with $A_c = 0.25 \times A_{c,ref}$ and $A_c = 0.5 \times A_{c,ref}$, respectively. Then, the increase of control amplitude is by 0.1 in the direction of the arrow.

Velocity contours obtained at $y/\delta_{in} = 0.517$ are illustrated in figs. 4.15 and 4.17 representing cooled, adiabatic and heated scenarios, respectively. The applied control

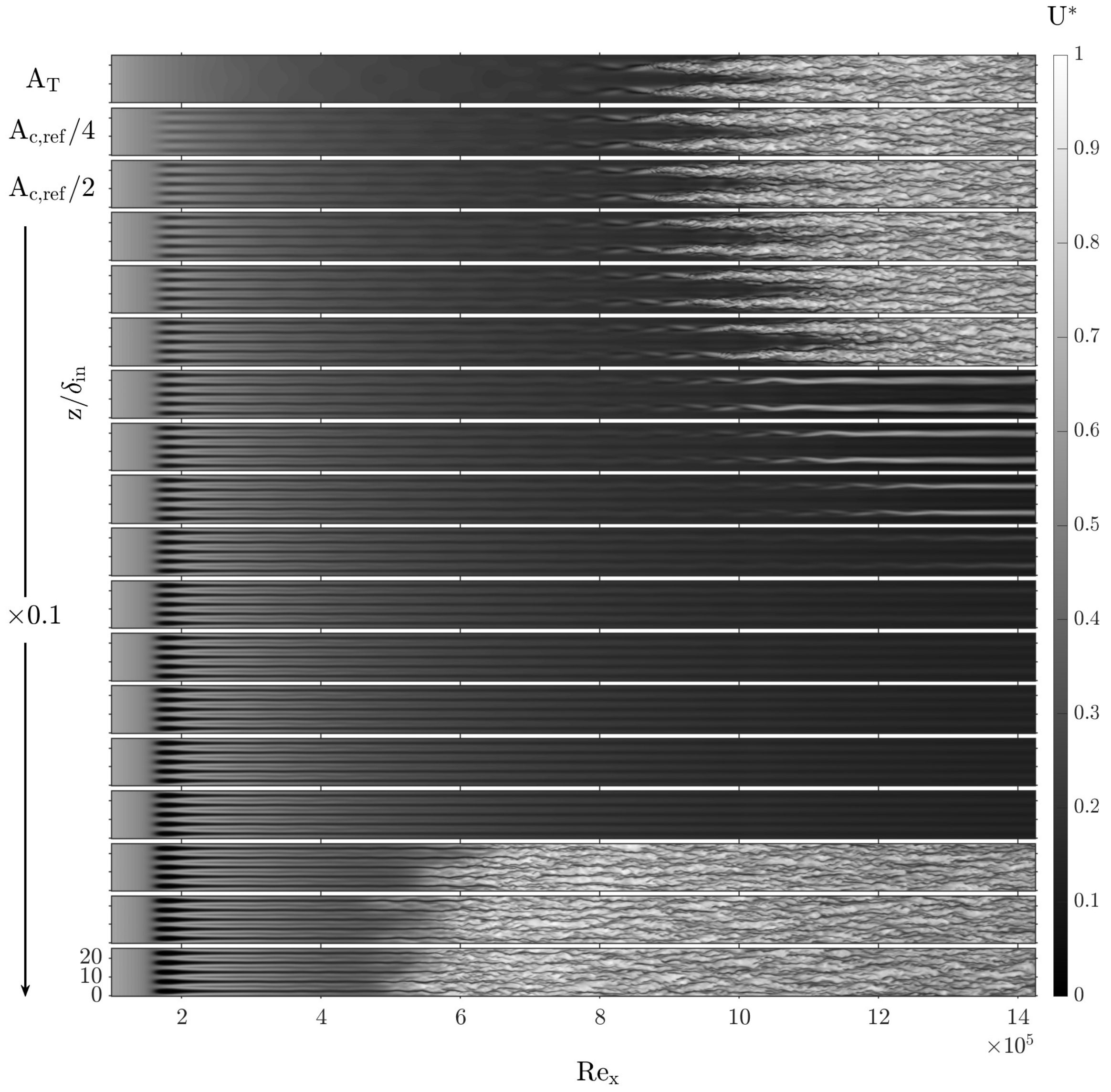

Figure 4.16: Contours of $U^* = (u - u_{min})/(u_{max} - u_{min})$ at $y/\delta_{in} = 0.517$ in an instantaneous flow-field for various control amplitudes in the adiabatic scenarios. From top-to-bottom, the first one designates $\mathrm{A_T}$ whereas the trailing two are the controlled cases with $A_c = 0.25 \times A_{c,ref}$ and $A_c = 0.5 \times A_{c,ref}$, respectively. Then, the increase of control amplitude is by 0.1 in the direction of the arrow.

amplitude ranges from $A_{c,ref} \times 0.25 \leq A_c \leq A_{c,ref} \times 2.0$ where $A_{c,ref} = 1.22 \times 10^{-2}$, identical to the control amplitude in table 4.1. We define an effective/successful transition control for cases where the transition is delayed until the end of the computational domain. Our observations reveal that below a certain threshold of the control amplitude, the transition scenario resembles the uncontrolled cases. Similar behavior was observed by Sharma, Shadloo, Hadjadj and Kloker (2019) and Kneer et al. (2022) when their control amplitude was halved although their control amplitudes were reported to be differing by a factor of 2 among each other. Furthermore, drastic changes in the flow are observed with an effective transition delay when the amplitude is increased above certain values, *i.e.* $A_c \geq 0.7 \times A_{c,ref}$ for cooled, $A_c \geq 0.9 \times A_{c,ref}$ for adiabatic, and $A_c \geq 1.2 \times A_{c,ref}$ for the heated cases. However, contrary behavior in the flow field is seen for the upper threshold amplitude. When the amplitude is increased from 1.7 to $1.8 \times A_{c,ref}$, an earlier transition onset compared to the uncontrolled scenarios is observed, regardless of the thermal boundary condition. The study of streamwise evolution of various disturbance modes revealed that the MFD (0,0), the control mode (0,5), and the integer multiples of the control mode are the only increasing modes among all. Therefore, the immediate shift in transition onset is attributed to streak instabilities that induce bypass transition according to Paredes et al. (2016*b*,*a*) when the initial streak amplitude exceeds a certain threshold. They also reported an approximate saturation of the transition onset location following a sufficiently high amplitude reached by the streaks. This phenomenon is also seen in our study once the initial streak amplitude goes 1.7 times higher than $A_{c,ref}$. However, additional simulations indicate that transition might occur immediately after the control strip in case of higher control amplitudes than those used in this study. In conclusion, cooling the boundary layer increases the range of amplitude for successful transition control, while heating has the opposite effect and reduces the range of application. Furthermore, heating has a more significant impact on modifying the control amplitude range compared to cooling. Additionally, the effectiveness of the control mode (0,4) is investigated as Sharma, Shadloo, Hadjadj and Kloker (2019) found this mode beneficial in delaying transition for an identical flow/geometry configuration with an adiabatic wall. Therefore, although the results are not presented here, a parametric study with (0,4) is carried out for the same range of control amplitudes. The results indicate that the effective range for (0,4) lies within $A_{c,ref} \times 0.7 \leq A_c \leq A_{c,ref} \times 1.2$ for the adiabatic wall condition. It is observed that the low-level threshold of (0,4) is lower than that of (0,5), and there is a significant difference in their applicable range for successful transition control. A comparison in terms of $(\rho u)'_{max}/(\rho_\infty u_\infty)$ shows 16.8-24.1% for (0,4) and 18-25.8% for (0,5), estimated at the control strip. The summary of the effective range of control amplitudes for the studied scenarios is presented in table 4.2.

Table 4.2: The range of the control streaks amplitude for effective transition control.

Cases	T_w/T_{rec}	Control Mode	$A_c/A_{c_{ref}}$ (%)	$(\rho u)'_{max}/(\rho_\infty u_\infty)$ (%)
A5C	1	(0,5)	90-170	18-25.8
A4C	1	(0,4)	70-120	16.8-24.1
C5C	0.95	(0,5)	70-170	15.8-26.5
H5C	1.05	(0,5)	120-170	20.8-25.2

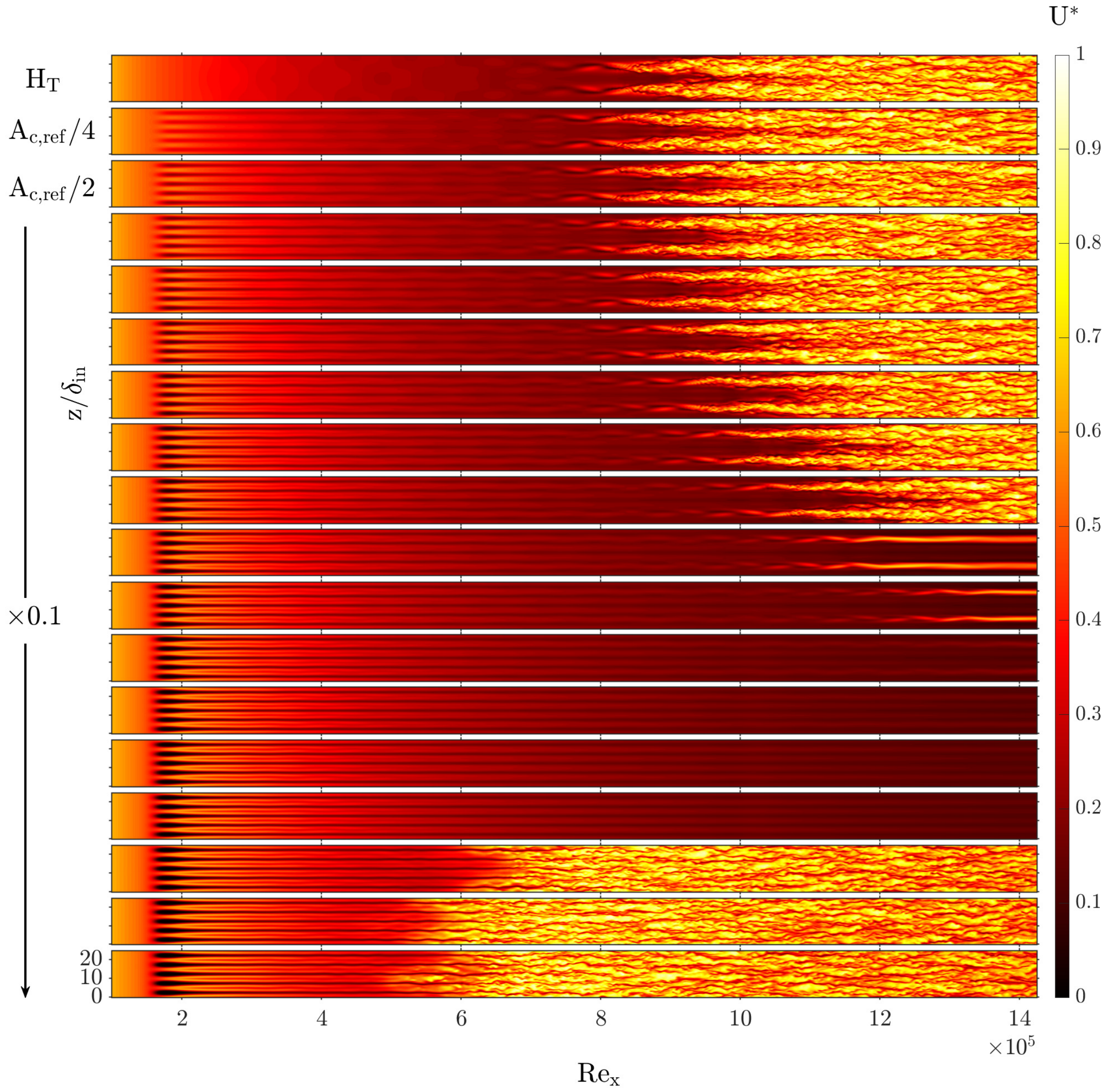

Figure 4.17: Contours of $U^* = (u - u_{min})/(u_{max} - u_{min})$ at $y/\delta_{in} = 0.517$ in an instantaneous flow-field for various control amplitudes in the heated scenarios. From top-to-bottom, the first one designates H_T whereas the trailing two are the controlled cases with $A_c = 0.25 \times A_{c,ref}$ and $A_c = 0.5 \times A_{c,ref}$, respectively. Then, the increase of control amplitude is by 0.1 in the direction of the arrow.

4.3 Conclusion

In an attempt to investigate the effectiveness of the velocity streaks in delaying boundary-layer transition under the influence of wall heat transfer, perturbed supersonic flows at $M_\infty = 2$ are investigated by means of DNS. The most amplified disturbance, determined for the adiabatic wall condition, is also considered for isothermal walls with weak heating/cooling effects to assess their isolated impact. Streaks with five times the wavenumber as that of the first-mode instability are introduced through a blowing/suction strip placed ahead of the perturbation strip. Initially, a stabilizing/destabilizing influence of cooling/heating is demonstrated in the absence of the control streaks, conforming with the linear stability theory for the still dominantly viscous instability. The parametric study revealed that to achieve successful transition delay, control amplitudes of 15.8-26.5%, 18-25.8%, and 20.8-25.2% are required for cooled, adiabatic, and heated walls, respectively. The combined effect of control mode and cooling expands the successful application range of control amplitude, while heating narrows it down.

Heating has no significant impact on the development of the control streaks, and the evolution of the disturbances in terms of their profile shape in the boundary layer. However, it strongly influences the growth rate of the disturbances, whilst dramatically reducing the application range of the once-excited control streaks, *i.e.* low control amplitudes are not as effective as for the adiabatic or cooled cases. Testing an alternative steady control mode (0,4) revealed that $(\rho u)'_{max}/(\rho_\infty u_\infty)$ of 16.8-24.1% is required for successful transition delay, indicating the higher effectiveness of (0,5) that conforms with the assertion of Sharma, Shadloo, Hadjadj and Kloker (2019).

Chapter 5

Stanton number in laminar compressible boundary layers

Contents

In this chapter, we investigate the Stanton number behavior in super-/hypersonic laminar boundary-layer flows under different wall heating/cooling rates using self-similar solutions of the compressible boundary layer (BL) equations and direct numerical simulations (DNS). The objective is to provide a detailed analysis of the observation in chapter 4, particularly in fig. 4.8, suggesting that cooled walls show a lower Stanton number than heated walls. This finding contradicts the widely accepted presentation in related textbooks, *e.g.* *Viscous fluid flow* by White and Corfield (2006) and *Hypersonic and high temperature gas dynamics* by Anderson (2000), thus necessitates an explanation.

5.1 The state of the art

Common knowledge is that the Stanton number is always higher for a cooled wall than a heated one as demonstrated in fig. 5.1 by Van Driest (1952). However, previous results of flat-plate boundary layer subjected to a low rate of heating/cooling, *i.e.* ±5% of the recovery temperature T_{rec} at $M_\infty = 2.0$ contradicted this behavior, see fig. 4.8. Here, T_{aw}

stands for the estimated wall temperature by the solution of the boundary-layer equations at adiabatic wall condition.

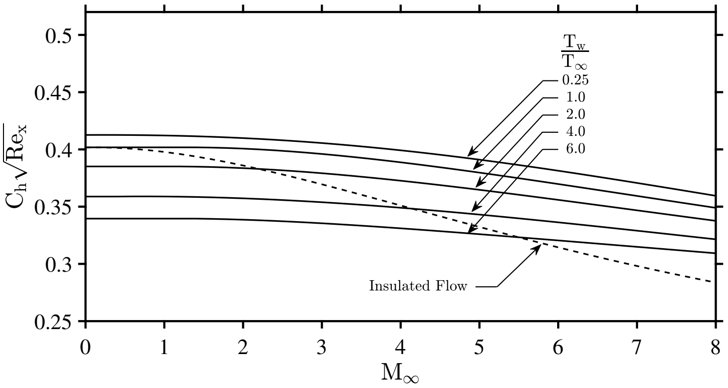

Figure 5.1: Local Stanton number for a laminar boundary layer for different wall-to-free-stream temperature ratios. The figure is regenerated from Van Driest (1952).

5.2 Results

5.2.1 Self-similar solution

In this study, the same parameters as in Van Driest (1952) are used, *i.e.* $T_\infty = 217.82$ K and $Pr = 0.75$. To analyze a broad range of isothermal wall boundary conditions and Mach numbers, self-similar solutions that are derived from the compressible boundary-layer equations and direct numerical simulations are used. BL solutions have been obtained, extending from the wall to the free stream, with $\eta_{max} = 10$ and $N_\eta = 10^4$ equidistant points in the wall-normal direction yielding converged results, *e.g.* $\eta_{\delta_e} < 5$ for $2.9 < T_w/T_\infty < 11.6$ at $M_\infty = 6$. The Stanton number in the self-similar coordinate is calculated using the heat transfer rate from the wall as

$$C_h = \frac{1}{\sqrt{2\rho_\infty u_\infty \mu_\infty x}} \frac{\lambda_w}{C_{p_w}} \frac{\rho_w}{\rho_\infty} \frac{T_\infty}{(T_{rec} - T_w)} g'(0), \tag{5.1}$$

$$C_f = \frac{2\mu_w \rho_w}{\rho_\infty \sqrt{2\rho_\infty u_\infty \mu_\infty x}} f''(0). \tag{5.2}$$

Figure 5.2 shows the local Stanton number at different Mach numbers under isothermal wall conditions, *i.e.* wall heating/cooling rates, $R_q = T_w/T_{rec} - 1$ (%). As R_q approaches zero, the Stanton number becomes asymptotic, indicating an adiabatic wall condition where C_h becomes indefinite. As in Chapter 4, T_{rec} is estimated for laminar flow where $r = \sqrt{Pr}$. Notably, fig. 5.2 displays a R_q threshold for each Mach number, above which the local Stanton number for the cooled wall surpasses that for the heated wall. The higher the Mach number the more important the behavior becomes because the threshold level increases with increasing Mach number. Considering that the associated threshold value at Mach 2.0 is $|R_q| = 13.15\%$, our earlier DNS results might be justified with the trend attributed to the interplay between thermal conductivity and the temperature gradient at the wall as: in addition to the higher thermal conductivity of the heated wall, the temperature gradient at the wall is only relatively lower than that of the cooled wall, before the R_q threshold is reached. As a result, the heated wall exhibits a larger Stanton number until the threshold is exceeded.

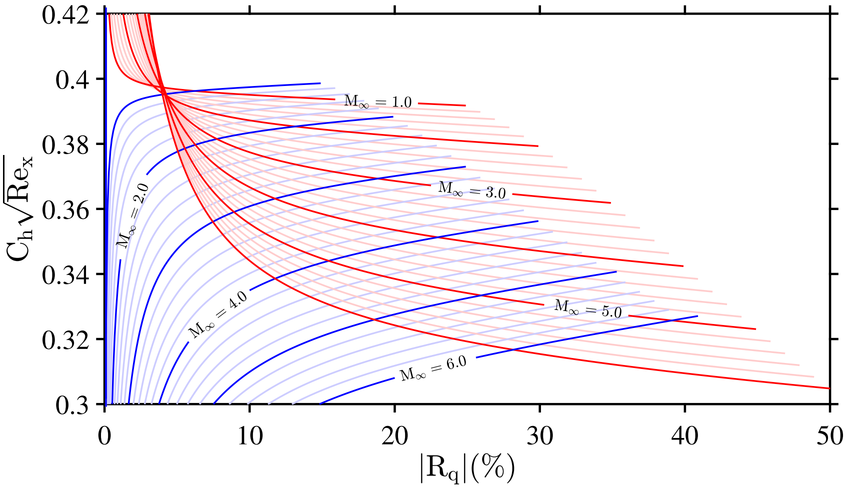

Figure 5.2: Stanton number as a function of heating/cooling rates with respect to T_{rec}. Heated (red) and cooled (blue).

While the numerical results seemingly offer an appealing physical interpretation, the crucial aspect lies in defining the adiabatic wall temperature using an approximated equation based on the recovery factor. Specifically, for the tested Pr, T_{aw} and T_{rec} exhibit accurate collapse as depicted in fig. A.8 with a discrepancy remaining below 2% up to $M_\infty = 8.0$ in case of $Pr = 0.75$. This difference increases with Mach number as follows: when $Pr < 1$ the recovery factor goes down with Mach number meaning that the recovery loss gets larger, leading to $T_{aw} < T_{rec}$. For $Pr > 1$, this effect is inversed (Lushchik and Makarova, 2016). Figure 5.2 is regenerated using T_{aw} for the definition of C_h in eq. 5.1 and results are plotted in fig. 5.3 in combination with some of those obtained with T_{rec}. For T_{aw}, it is observed that cooling consistently results in a larger C_h than heating in laminar ZPG flows. This outcome is in line with the findings of Van Driest (1952), who however used the Reynolds analogy to get the Stanton number without explicitly pointing this out, underscoring the substantial influence of the slight deviation between T_{aw} and T_{rec} on our analysis. It is also observed that the discrepancy between $C_h(T_{aw})$ and $C_h(T_{rec})$ diminishes with increasing heating/cooling.

It is of general practice to use T_{rec}, especially in engineering applications, as T_{aw} is

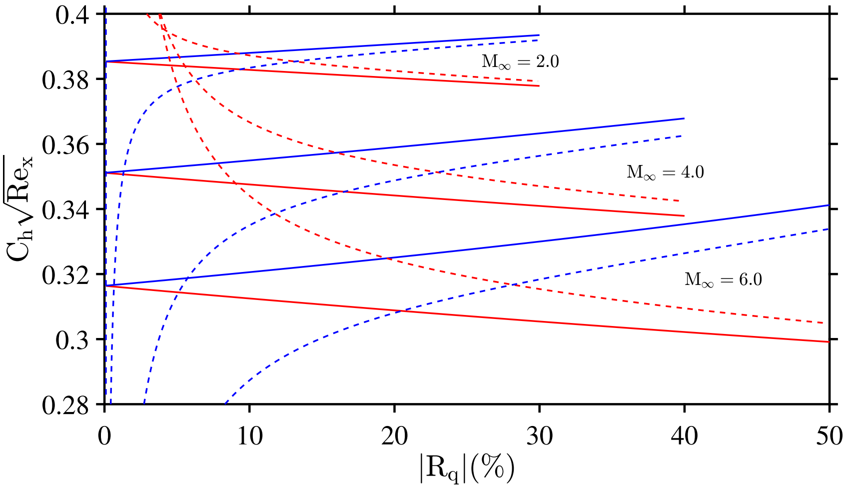

Figure 5.3: Stanton number as a function of heating/cooling rates with respect to T_{aw} (solid lines) and T_{rec} (dashed lines). Heated (red) and cooled (blue).

not always or readily available. Thus, to provide some guidance, table 5.1 presents the relative error resulting from using T_{rec} and the associated R_q values at two Pr numbers, standing for the relevant interval in compressible flows, excluding the hypersonic regime with high-temperature effects (Anderson, 2000). Due to the approximated T_{rec}, the associated R_q for the same confidence level is higher for a lower Pr, reflecting the growing discrepancy between T_{aw} and T_{rec} as Pr deviates from unity. A more accurate approximation compared to the classical $r = \sqrt{Pr}$ would decrease the required R_q level to attain desired confidence level for the evaluation of C_h using T_{rec}. The reference temperature concept where fluid properties such as ρ, μ, C_p, and λ are evaluated at some average boundary-layer temperature might be an alternative way of estimating the adiabatic wall temperature (White and Corfield, 2006). However, Pr varies with the reference temperature which itself depends on M_e, T_e, and T_w. This inter-dependency of multiple parameters would require a complex parametric analysis, diverting attention from the main discussion. Therefore, we retain the classical estimation using a constant Pr value. It is also reminded that the recovery factor is highly dependent on the pressure gradient in non-ZPG flows. It was found to be decreasing as a function of favorable-pressure-gradient (FPG) when $Pr < 1$ and increasing when $Pr > 1$ for $C = 1$ (Hokenson, 1972).

Although Sutherland's formula accurately provides the dynamic viscosity for a wide range of thermal conditions, it fails when the temperature drops below 110 K, where the dynamic viscosity becomes linearly dependent on temperature Schlichting and Gersten (2016). These low-temperature values are not observed even in the upper layers of the atmosphere, but they are common in hypersonic wind tunnels where "cold flow" experiments are conducted Lee and Chen (2019). Therefore, we repeated the same analysis as in figure 5.2, but assuming a linear dependence of the dynamic viscosity on temperature,

Table 5.1: Confidence level in employing the approximated formula for the adiabatic wall temperature with $\epsilon = (C_h(T_{rec}) - C_h(T_{aw}))/C_h(T_{aw})$ (%).

M_∞	$\epsilon = \epsilon(Pr = 0.75)$ (%)	$\pm R_q(\%)$	$\epsilon = \epsilon(Pr = 0.70)$ (%)	$\pm R_q(\%)$
1	10	0.3	10	0.3
	5	0.5	5	0.6
	2	1.0	2	1.3
2	10	1.2	10	1.5
	5	2.5	5	3.0
	2	5.9	2	7.4
3	10	3.2	10	3.9
	5	6.3	5	7.7
	2	15.5	2	18.9
4	10	5.6	10	6.8
	5	11.1	5	13.4
	2	27.1	2	32.7
5	10	8.0	10	9.7
	5	15.8	5	19.1
	2	38.2	2	45.9
6	10	10.2	10	12.3
	5	20.0	5	24.2
	2	47.9	2	57.1

i.e. $C = 1$ in eqs. B.1-B.2, while keeping all other parameters the same. The results, presented in figure 5.4, show that the C_h values converge to around 0.4 for non-small values of R_q when T_{rec} is used. The heated wall always has a higher C_h than the cooled wall regardless of the Mach number. Additionally, an increase in Mach number causes the local Stanton number to decrease for the cooled wall, while the opposite trend is observed for the heated wall. Meanwhile, although not illustrated here, the same analysis by using T_{aw} leads to a single constant which bears resemblance to the pioneering study by Cohen & Reshotko Cohen and Reshotko (1955) where $Pr = 1$ as well as $C = 1$ were assumed. They showed that, for ZPG flow, the local skin-friction coefficient and Stanton number depend neither on Mach number nor on the thermal boundary condition at the wall.

To provide a different perspective on fig. 5.1, local C_f and C_h values are evaluated using self-similar solutions and presented in a similar manner. For C_f, the trend in fig. 5.5a shows that cooling the wall decreases the boundary-layer thickness, which in turn increases the velocity gradient and the skin friction at the wall. In contrast, a more detailed explanation is required for C_h, as shown in fig. 5.5b. Employing T_{rec}, the results demonstrate a discontinuity at the respective Mach number when wall heating gets to cooling for $T_w/T_\infty > 1$. This discontinuity in a selected line of the self-similar solution corresponds to the adiabatic wall condition for the associated Mach number. For a given isothermal condition, the left side of this discontinuity represents the heated wall, while

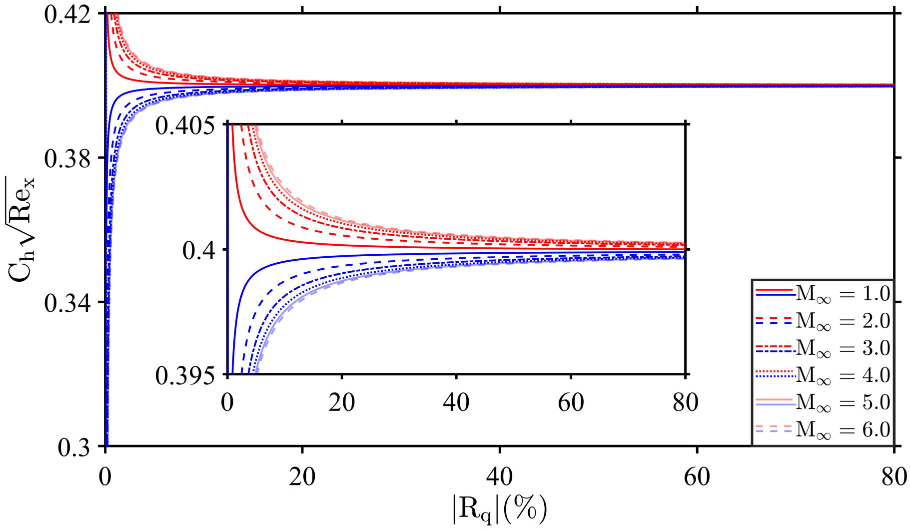

Figure 5.4: Same as figure 5.2 but for linearly dependent dynamic viscosity on temperature, $C = 1$, using T_{rec}. Heated (red) and cooled (blue).

the right side is referred to as the cooled wall. The results obtained using T_{aw} exhibits a smooth monotonous trend in C_h as in C_f, with distinct deviations from the results for T_{rec}. The discrepancy between both cases exists at all Mach numbers when $T_w/T_\infty \leq 1$, while it virtually appears only on the cooled wall, *i.e.* right side of the discontinuity for $T_w/T_\infty > 1$. Near the adiabatic case the error with the approximation formula gets tremendous, causing the exhibited spurious pole.

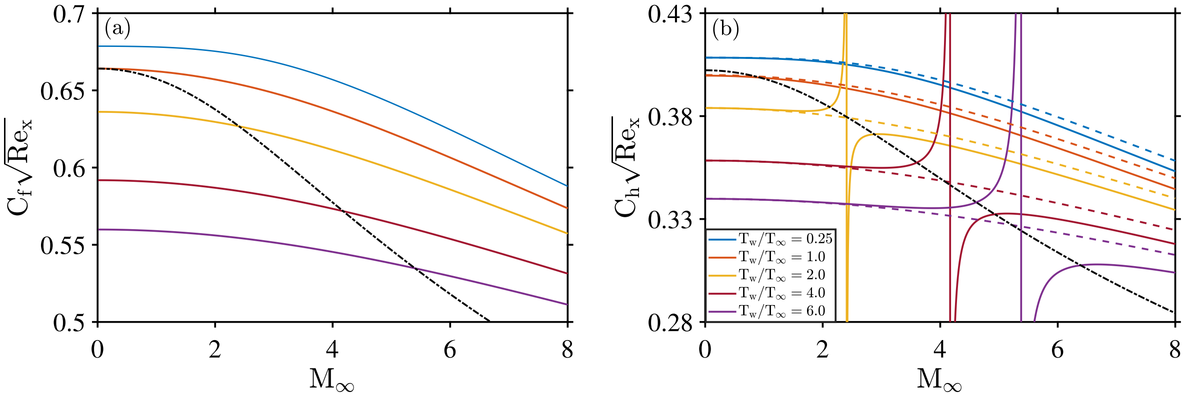

Figure 5.5: (a) Skin-friction coefficient and (b) Stanton number as a function of Mach number for different wall-to-free-stream temperature ratios. Insulated wall by the Reynolds analogy (dashed-dotted line), BL solution with T_{rec} (solid lines), and T_{aw} (dashed lines).

A similar analysis for C_h is performed using various Prandtl numbers presented in fig. 5.6. Comparing it with fig. 5.6b, we observe that as the Prandtl number approaches unity, the flattened trend of the Stanton number near the discontinuity shrinks. When $Pr = 1$, indicating about equal velocity and temperature boundary-layer thicknesses and a recovery factor of 1, the results obtained using T_{aw} and T_{rec} perfectly align. At this condition, the discontinuity for $T_w/T_\infty > 1$ becomes a singular point on the lines. However, for $Pr > 1$, the solution approaches the discontinuity with an opposite slope compared to $Pr < 1$ in case of T_{rec}.

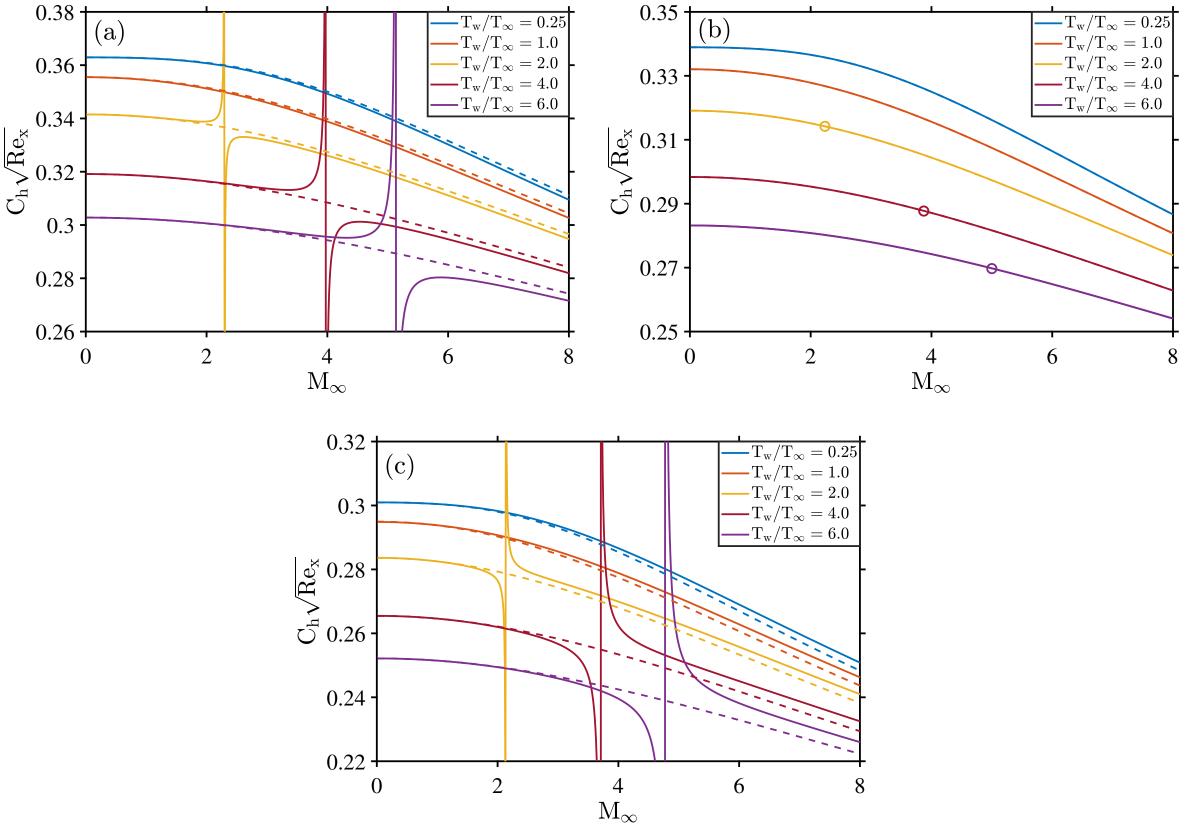

Figure 5.6: The effect of Prandtl number; (a) $Pr = 0.9$, (b) $Pr = 1.0$ with singular points (symbols), and (c) $Pr = 1.2$ on the local Stanton number as a function of Mach number for different wall-to-free-stream temperature ratios. BL solution with T_{rec} (solid lines), and T_{aw} (dashed lines).

5.2.2 Direct numerical simulation

In addition, two-dimensional DNS for Mach numbers ranging from 2.2 to 2.8 at $T_w/T_\infty = 2.0$ with the same thermodynamic parameters as with the boundary-layer solver has been conducted. A mesh convergence study is performed by examining the local values due to their high sensitivity to changes in flow parameters, as depicted in fig. 5.7a. The mesh is refined in both streamwise and wall-normal directions until reaching a deviation certainly lower than 0.5% in both the Stanton number and the skin-friction coefficient downstream of $Re_x = 10^5$, indicating a sufficient streamwise position away from the leading edge. To circumvent any numerical problem due to the singularity at the leading edge as a result of the viscous-nonviscous interaction, the equidistantly distributed mesh in the streamwise direction is refined drastically as indicated in table C.1. Here, the non-dimensional parameters are calculated in the dimensional coordinate such that $C_h = \dot{q}_w/[\rho_\infty u_\infty c_p(T_{aw} - T_w)]$

where $\dot{q}_w = -\lambda_w(\partial T/\partial y)|_w$ with T_{aw} obtained from adiabatic DNS cases. Following the mesh convergence, a comparison is made between the self-similar solution and the results of DNS in fig. 5.7b. It is seen that despite using the T_{aw} in estimating the C_h, DNS results initiated from the leading edge incidentally exhibit a similar trend to the BL solution with T_{rec}. A gradual downstream decrease of T_{aw}, as seen in fig. A.9a, results in slightly higher values on the left-side of the discontinuity, while lower values are obtained on the right-side at earlier streamwise locations. However, simulations starting at $Re_x = 10^5$ leads to C_h values between the BL solutions with T_{rec} and T_{aw} since the wall temperature in these DNS cases are closer to T_{aw} of the BL solution, see fig. A.9a. At $Re_x = 4 \times 10^5$, the maximum difference between the DNS results is observed at $M_\infty = 2.45$ and remains below 5% with a higher sensitivity around the discontinuity. Moreover, the discrepancy, which constantly reduces downstream, at any streamwise position is not higher than 10%. There are multiple factors playing a part in the observed discrepancies between the DNS results and the BL solutions: non-zero pressure gradient both in x and y- directions, see fig. A.9b, along with the alteration of the BL edge conditions in the DNS in contrast to the BL solution, slight streamwise variation of T_{aw} and its deviation from the BL value as seen in figure A.9a, adopted numerical schemes, and the finite-difference method along with the number of points used to estimate the wall temperature gradient.

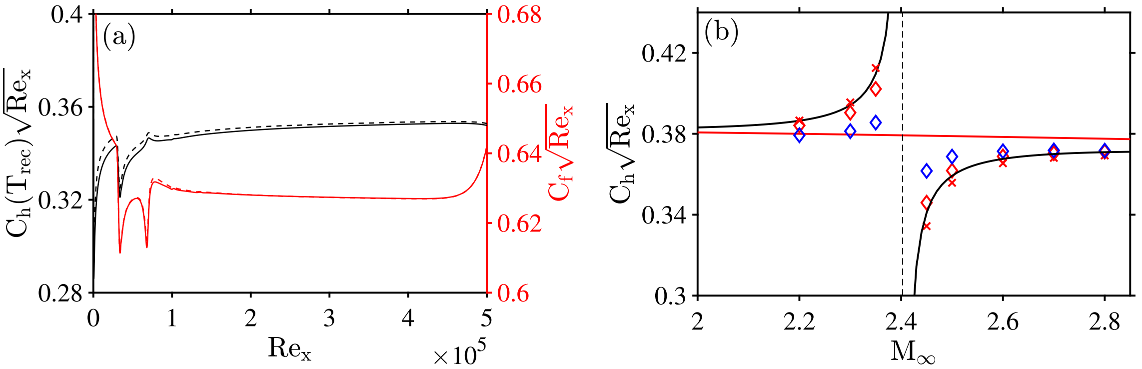

Figure 5.7: (a) Mesh resolution analysis at $M_\infty = 2.5$ through DNS with a fine (dashed line) and a coarse (solid line) mesh. (b) Streamwise evolution of C_h for $T_w/T_\infty = 2.0$, corresponding to $R_q(\%) = (T_w/T_{aw,BL} - 1) =$ +8.8, +4.38, +2.22, +0.12, -1.94, -3.96, -7.87, -11.61, and -15.18 from Mach 2.2 to 2.8 at $Re_x = 2 \times 10^5$ (cross) and $Re_x = 4 \times 10^5$ (diamond). BL solution with T_{aw} (−) and T_{rec} (−). DNS results initiated from $Re_x = 10^5$ (blue) and from the leading-edge (red). Adiabatic condition is marked with the vertical dashed line.

Returning to fig. 4.8, non-adiabatic simulations with 5% heating/cooling rates, based on T_{aw}, as well as an adiabatic case which is used to extract the wall temperature for evaluating C_h are performed. Due to slight difference between T_{rec} and T_{aw} at $M_\infty = 2.0$ and $Pr = 0.72$, using T_{rec} results in ≈ 5.1% of heating and ≈ 4.9% cooling with respect to T_{aw}. Figure 5.8 presents the results using two different mesh resolutions and the BL solution. The coarse mesh resolution, standing for the mesh used in Chapter 4, accurately captures the C_f trend and the values estimated by the BL solution, as shown in fig. 5.8b, whereas differences arise from the boundary layer in C_h, as seen in fig. 5.8a. Moreover, the boundary layer trend suggesting higher Stanton number for the cooled wall could not be captured. Further mesh refinement, beyond which the results alter only negligibly, brings the DNS results closer to the BL solution, and the concerning trend becomes evident only after around $Re_x = 10^6$, as the evolution of the heated wall slightly depends on Re_x. This contrasting trend observed in DNS before $Re_x = 10^6$ is attributed to the factors explained for fig. 5.7. It is also noted that DNS trend becomes more akin to the BL solutions for higher heating/cooling rates, indicating the high sensitivity of the Stanton number near the adiabatic condition, as illustrated in fig. 5.7.

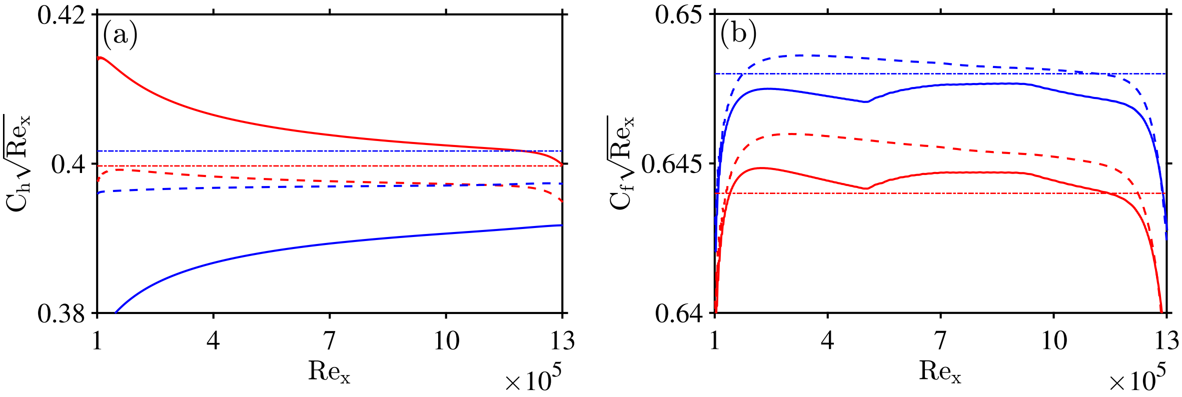

Figure 5.8: (a) Evolution of the Stanton number and (b) skin-friction coefficient in DNS environment. Coarse mesh (solid lines), refined mesh (dashed lines), and BL solutions with T_{aw} (dashed-dotted lines). Heated (red) and cooled (blue).

5.3 Conclusion

It is illustrated that there is a minor deviation between the commonly used approximative formula for the recovery temperature and the true adiabatic wall temperature obtained by the boundary-layer solution. Although this insignificant difference is usually neglected, employing both definitions results in considerably different Stanton number values for weak to mild wall cooling or heating. With the true adiabatic value, C_h for heating is always lower than for cooling, whereas the approximative T_{rec} introduces a threshold wall heating/cooling rate at a specified Mach number, below which C_h is larger for the heated wall than for the cooled wall. For practical purposes, the required heating/cooling rates for the use of T_{rec} are quantified at different confidence levels. Moreover, DNS results initiated from the leading edge present unexpected coherence with the BL solution obtained using T_{rec}, which is attributed to the streamwise alteration of the adiabatic wall temperature in the DNS environment that are inherently contradictory to the hypotheses behind BL theory. Meanwhile, the outcome for DNS initiated by excluding the leading edge at a constant T_w becomes sensitive around the adiabatic condition, with a reducing discrepancy downstream.

Chapter 6

Transition control near hypersonic regime

Contents

Having successfully postponed first-mode induced transition in Chapter 4, the current chapter employs control streaks to suppress second-mode instabilities in the high-supersonic/near-hypersonic regime. A parametric study explores control modes with varying wavenumbers and amplitudes. Additionally, the characteristics of the streaks are scrutinized in comparison with the previous analysis. Ultimately, the source of stabilization is investigated through the implementation of a non-linear disturbance formulation. Some results from this chapter were presented at the 2^{nd} European Symposium on Laminar/Turbulent Transition in the Hypersonic Regime[8].

6.1 Problem setup

Due to their higher growth rates compared to the first modes at $M_\infty > 4.0$ at adiabatic wall, second-mode instabilities are naturally expected to drive the flow towards transi-

---

[8] https://www.hyfar-ara.org/en/11-control-of-second-mode/

tion. However, these disturbances amplify within a relatively limited streamwise extent when compared to low-frequency first-mode disturbances. Earlier studies have shown that the primary instability leading to transition significantly depends on the flow/geometry configuration and boundary conditions in hypersonic flows. On a flat plate at Mach 6.0, first-mode-induced oblique breakdown was identified as the most viable transition path (Franko and Lele, 2013; Unnikrishnan and Gaitonde, 2019; Caillaud, 2022), while second-mode-induced fundamental resonance was found to be responsible over various cone-shaped geometries (Sivasubramanian and Fasel, 2015). Meanwhile, linear stability analysis on an adiabatic flat plate boundary layer revealed that the critical N-factor of 10 was reached by first-mode disturbances up to Mach 7.0 before second-mode instabilities. However, in a flight condition, reality deviates, and flight data, as depicted in fig. A.10, indicates significant wall cooling even before the terminologically accepted hypersonic regime of Mach 5.0 (Anderson, 2000). Considering the destabilizing impact of cooling on second-mode disturbances (Mack, 1969, 1984), a more substantial role is anticipated from these instabilities even before reaching the hypersonic limit (Malik, 1989). Indeed, Lysenko and Maslov (1984) emphasizes nearly complete stabilization of first-mode disturbances over a flat plate at Mach 4.0 with 54% wall cooling compared to adiabatic condition.

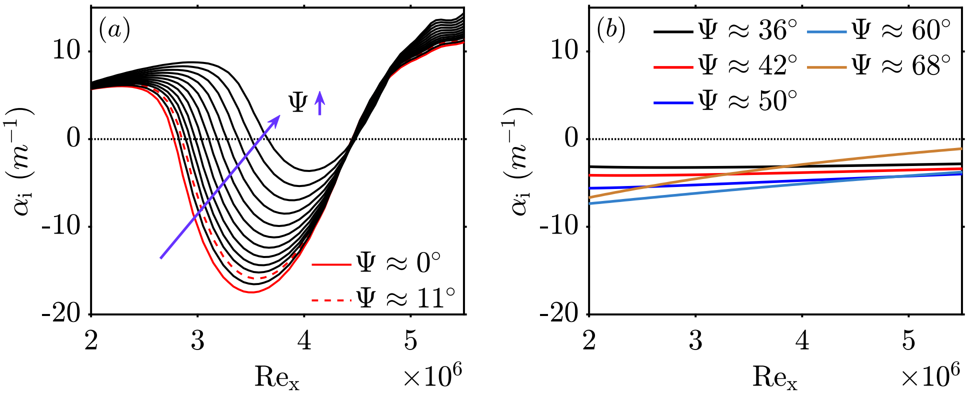

Figure 6.1: Growth rate of instabilities: (a) second-mode at $f = 91$ kHz and (b) first-mode at $f = 21$ kHz at $M_\infty = 4.5$, $T_\infty = 65.15$ K, and $T_w = 4.0 \times T_\infty \approx 0.9 \times T_{rec}$.

Recent studies on second-mode-induced transition have predominantly concentrated on the fundamental (K-type) and subharmonic (H-type) resonance mechanisms, given that the 2-D second mode amplifies more than 3-D disturbances (Chynoweth, 2018; Meersman et al., 2018; Sivasubramanian and Fasel, 2014, 2015; Hader and Fasel, 2017, 2019). However, linear stability analysis in fig. 6.1, exhibits that 3-D second-mode disturbances with low obliqueness amplify nearly as strongly as their planar counterparts. A recent direct numerical simulation (DNS) study indeed demonstrated that the 3-D second-mode instability wave can lead to oblique breakdown at Mach 4.5 (Zhou et al., 2022).

6.1.1 Simulation parameters and boundary conditions

The flow/geometry configuration and the 3-D second-mode disturbance are identical as $\mathrm{Sm_{ob}}$ in Chapter 3 and named as $\mathrm{A_T}$ in the present chapter. As indicated in fig. 6.1, the wall is cooled only slightly despite the high cooling rates indicated by the flight data in A.10. This aims to retain first-mode instabilities within the domain for later incorporation with broadband disturbances. For transition delay, inspired by the streak employment method in Chapter 4, the initial investigation employs control mode (0,5) with three streak amplitudes. Table C.2 lists the performed DNS cases. For controlled scenarios, the first letter and the digit designate the amplitude level relative to (0,5). Other control modes' streak amplitudes are adjusted to match these three reference amplitudes at the end of the perturbation strip. Before delving into the results, the evolution of the streaks upon their generation requires careful examination.

6.1.2 Generation of the streaks

Control streaks are introduced through the same blowing/suction strip as employed in Chapter 4 and is positioned between $x_{c,1} = 0.418$ m and $x_{c,2} = 0.426$ m, corresponding to $Re_{x_{c,1}} \approx 3.0 \times 10^6$ and $Re_{x_{c,2}} \approx 3.06 \times 10^6$, respectively. In this analysis, only the control strip is activated. Figure 6.2 provides a closer look at the control strip vicinity, exhibiting streaks with varying spanwise wavenumbers and amplitudes. Notably, a more prominent hump is observed in the streak evolution for lower wavenumbers. To elaborate further on this phenomenon, simulations were conducted with a shorter streamwise width (w_c) of the control strip, while maintaining the end position unchanged, as depicted in fig. 6.3. The streaks are observed to reach higher amplitudes with increasing (w_c), irrespective of the initial streak amplitudes, while the hump decreases significantly. These observations bring about two main queries.

- **Q1:** A broader width of the control strip enables a higher resolution of the wave function in the streamwise direction. Thus, is the observed hump linked to the lower resolution of the control strip in the case of the shortest strip width? **R1:** Our analysis employing a higher streamwise resolution along the control strip resulted in an identical evolution of the control modes.

- **Q2:** Is the observed "correction" of the hump in the case of a wider strip solely a consequence of the increase in streak amplitude? **R2:** This cannot be true as

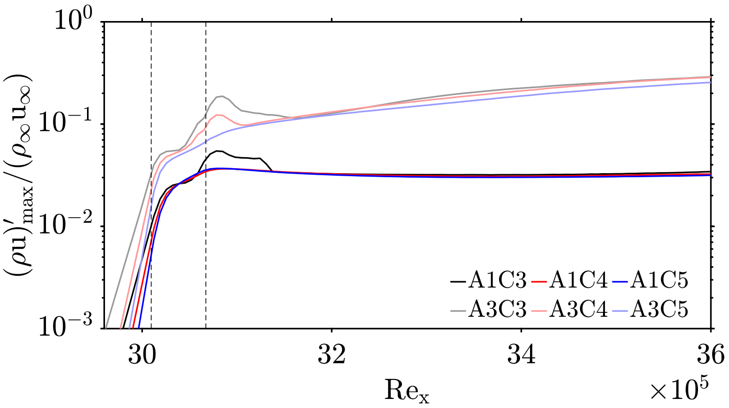

Figure 6.2: Streamwise evolution of maximum modal disturbance amplitudes for the control modes (0,3), (0,4), and (0,5) near strips. Vertical dashed lines: control strip beginning ($Re_x \approx 3 \times 10^6$) and end ($Re_x \approx 3.06 \times 10^6$) as well as the perturbation strip end ($Re_x \approx 3.16 \times 10^6$).

a comparison between figs. 6.3a and 6.3b reveals a higher hump generation with larger streak amplitudes for identical control strip widths.

What follows is the examination of two configurations where the width of the control strips are 8 *mm* and 12 *mm* while maintaining identical streamwise end positions. Upon observing that increasing w_c enhances the maximum amplitude of the streaks, the initial streak amplitude of the case with a larger strip is adjusted to match the case with the original width at the end of the perturbation strip. The analysis has been performed for two different initial streak amplitudes, as presented in fig. A.11. It is seen that when the streak amplitude is kept the same at the end of the perturbation strip (the deactivated one), near identical trends in the control mode and its first harmonic are seen.

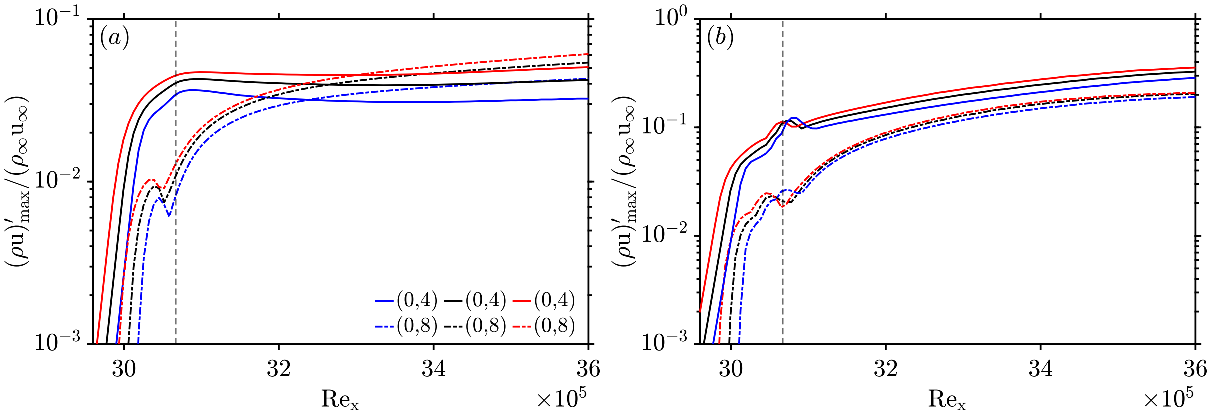

Figure 6.3: Streamwise evolution of maximum modal disturbance amplitudes for the streak amplitude of (a) $A_c \approx 1.21$ % and (b) $A_c \approx 2.42$ %. $w_c = 8$ mm (blue), $w_c = 10$ mm (black), and $w_c = 12$ mm (red). Vertical dashed line: control strip end ($Re_x \approx 3.06 \times 10^6$).

6.2 Results

The most recent study, to the best knowledge of the author, regarding 3-D 2^{nd}-mode control using streaks were conducted by Zhou et al. (2023). The researchers used identical formulations as ours to generate the control streaks[9]. Despite their encouraging outcomes, discrepancies indicated computations of under-resolved DNS which can significantly influence the results due to inaccurate resolving of the convective instabilities inside the boundary layer, particularly in the late non-linear regime and the breakdown. The boundary-layer thickness was reported to be decreasing after a certain streamwise location while delaying transition using control streaks with different spanwise wavenumbers. However, it has been shown that introducing streaks increases the momentum transfer from the wall to the boundary-layer edge and vice-versa, for which the boundary layer thickness grows, see fig. 4.11. Moreover, even if streaks decay downstream, the boundary layer should consistently grow due to momentum diffusion by the kinematic viscosity.

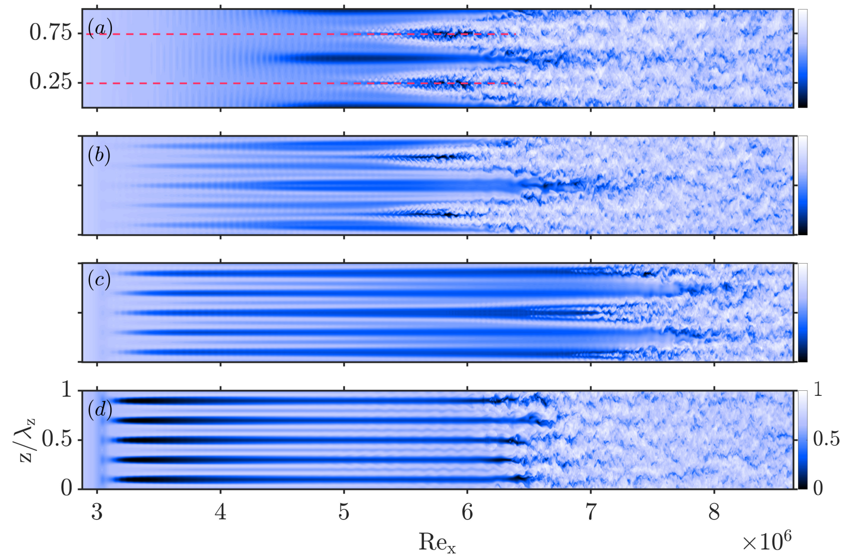

Figure 6.4: Contours of $U^* = (u - u_{min})/(u_{max} - u_{min})$ at $y/\delta_{in} = 0.75$ in an instantaneous flow-field for (a) A_T, (b) A1C5, (c) A2C5, and (d) A3C5.

Figure 6.4 illustrates the velocity contours taken inside the boundary layer proceeding the first initiatives with the control mode (0,5). The presence of the streaks with the lowest amplitude turned out to be insufficient in delaying the transition onset, exhibiting a similar breakdown scenario as in A_T. Moderate streak amplitude postpones the transition onset location somewhat downstream, without suppressing the fundamental disturbance entirely. In this case, breakdown occurs at the spanwise borders and the mid-spanwise

---

[9] The work presented in this chapter and the referenced study were conducted in parallel without the knowledge of each party.

direction contrary to $z/\lambda_z = 0.25$ and $z/\lambda_z = 0.75$ in A1C5 and $\mathrm{A_T}$. Increasing the streak amplitude further worsen the control mechanism by inducing the streak instabilities, similar to what has been observed in Chapter 4 for high-amplitude streaks.

A different series of tests is conducted using the control mode (0,4). The transition was effectively controlled with low and moderate streak amplitudes, while the application of the highest streak amplitude resulted in an earlier transition. Similar findings are obtained using the control mode (0,3), as detailed in fig. A.13. Regarding the streaks with highest amplitude, the evolution of C_f in fig. A.12 indicates that a control mode with a larger wavelength leads to an earlier transition than control modes with higher wavelengths. Besides, contrasting with our previous observation in Chapter 4, A3C5 does not induce an earlier breakdown compared to $\mathrm{A_T}$. For further insights into the stability of streaks with different wavenumbers, a 2-D linear stability analysis would be beneficial.

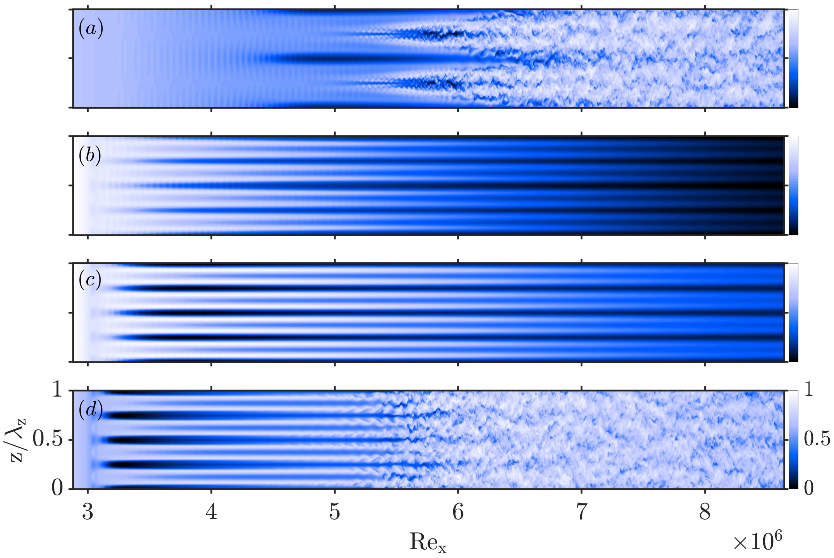

Figure 6.5: Contours of $U^* = (u - u_{min})/(u_{max} - u_{min})$ at $y/\delta_{in} = 0.75$ in an instantaneous flow-field for (a) $\mathrm{A_T}$, (b) A1C4, (c) A2C4, and (d) A3C4.

To enhance the depth of our analysis, streamwise evolution of disturbances has been traced in the presence and absence of the streaks. Figure 6.6 compares the controlled case with the moderate streak amplitude (A2C4) and $\mathrm{A_T}$. At first glance, it is seen that the presence of the streaks strongly attenuate the fundamental disturbance as well as the non-linear generated modes. Similar to the findings in the case of 1^{st}-mode induced oblique breakdown in Chapter 4, the streaks alter the receptivity of the disturbance, leading to a sudden reduction in the maximum disturbance amplitude near the injection location. Examining the control mode and the mean-flow-deformation (MFD) reveals the earlier generation of the MFD in the presence of streaks, as expected. Notably, both the control mode and the MFD reach saturation before reaching the mid-streamwise direction. The latter saturates with the steady disturbances, contrasting the findings of

Zhou et al. (2023), where the MFD was shown to reach 50% of the maximum amplitude by the end of the domain in case of complete transition control. However, unless the flow becomes turbulent, there is no reason for observing such drastic increase in the MFD (Sharma, Shadloo, Hadjadj and Kloker, 2019; Kneer et al., 2022).

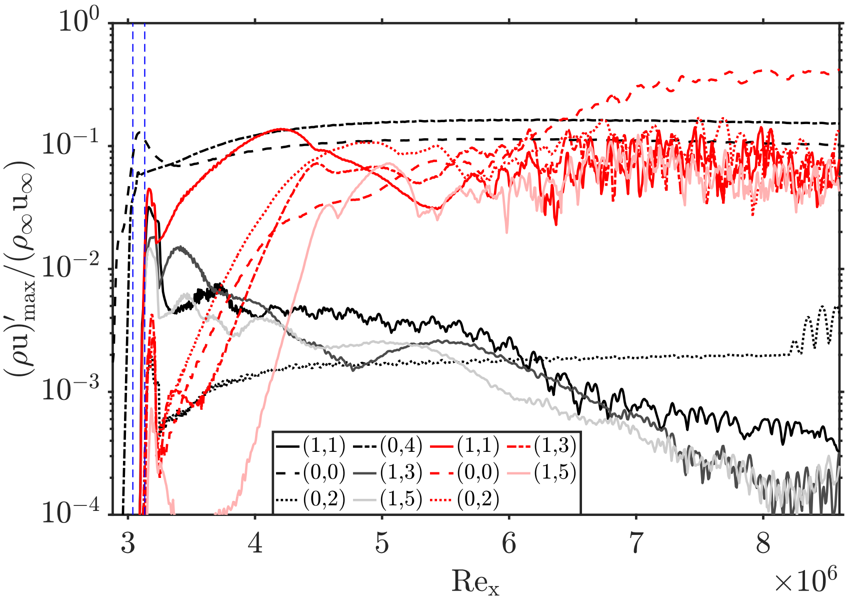

Figure 6.6: Streamwise evolution of maximum modal disturbance amplitudes for A2C4 (black) and $\mathrm{A_T}$ (red). Vertical dashed lines: control ($Re_x \approx 3.03 \times 10^6$) and the perturbation ($Re_x \approx 3.13 \times 10^6$) strip centers.

A comparison is provided for the evolution of the control streaks at two different Mach numbers for transition induced by two distinct oblique instabilities. At $M_\infty = 2.0$, the streaks exhibit immediate decay after their generation. In contrast, at $M_\infty = 4.5$, the amplification of streaks is highly contingent on the designated streak amplitude. Following their formation, they amplify transiently before reaching a plateau, until transition onset in A3C4. Furthermore, it is noted that, at $M_\infty = 4.5$, the first harmonic of the control mode may attain higher amplitudes than the control mode itself. This observation leads to questioning of the source of transition control, whether it is the designated streaks or their first harmonic. To explore this further, a comparison is made between the cases where (0,8) is chosen as the control mode, denoted as A2C8 and A2C4. Figure 6.8a depicts that the sole employment of (0,8) as control streaks has a detrimental impact on the flow field, leading to an earlier transition. A similar conclusion is drawn from the comparison of A2C6 and A2C3, as shown in fig. A.14. Thus, it is concluded that streaks should carry wavenumber four times less-and-equal to that of the fundamental disturbance, *i.e.* $\beta_z \leq 4 \times \beta_0$.

The selected amplitude range for the streaks are visualized in fig. 6.9 using the conventional definition of Andersson et al. (2001):

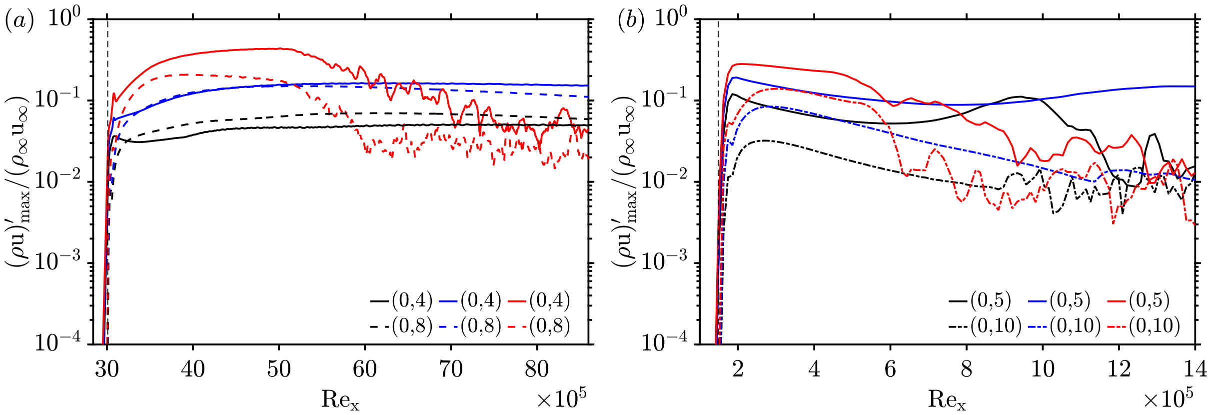

Figure 6.7: Streamwise evolution of maximum modal disturbance amplitudes for control streaks and their first harmonics. (a) 2^{nd}-mode induced OB at $M_\infty = 4.5$ and (b) 1^{st}-mode induced OB at $M_\infty = 2.0$. Vertical dashed lines: control strip centers (a) at $Re_x \approx 3.03 \times 10^6$ and (b) at $Re_x \approx 1.72 \times 10^5$.

$$A_{st} = \frac{1}{2u_\infty}\Big[max(u-u_b)_{y,z} - min(u-u_b)_{y,z}\Big]. \tag{6.1}$$

In incompressible flows, the estimated threshold value was found to be ≈ 26% of u_∞. Beyond this threshold, transiently growing streaks induce secondary inflectional instabilities, leading to turbulence breakdown (Andersson et al., 2001; Cossu and Brandt, 2002*b*; Bagheri et al., 2007; Shahinfar et al., 2012). When streaks were generated using spanwise distributed miniature vortex generators, the threshold increased to ≈ 32% of u_∞ (Fransson and Talamelli, 2012). In compressible flows, weakly nonlinear transiently growing streaks up to ≈ 20% were found to stabilize the first-mode instabilities through the nonlinear, plane-marching PSE analysis (Paredes et al., 2017). The parametric study for the control modes conducted in Chapter 4, as also illustrated in fig. A.15, shows that the threshold amplitude for the streaks lies around 42% both for the adiabatic and isothermal cases. For second-mode instabilities, successful transition delay occurs when the amplitude of transiently growing streaks remains below 35% (Paredes et al., 2019), contrasting with a limit of ≈ 21% in a recent DNS analysis using white noise disturbances (Caillaud, 2022). The present study exhibits ≈ 30% for the control mode (0,4), and extends the threshold amplitude up to ≈ 38% for (0,3) for the 3-D second-mode instability, as depicted in fig. 6.9. However, a more application-oriented conclusion requires a DNS analysis, incorporating a broad disturbance spectrum as in (Caillaud, 2022), rather than a forced transition at a single frequency/wavenumber.

In supersonic flows, an insulated flat-plate boundary layer always exhibits a generalized inflection point (GIP), meaning that the flow is subjected to inviscid disturbances (Malik, 1990). However, a sufficient amount of cooling has been shown to eliminate the GIP by stabilizing the flow against inviscid disturbances (Unnikrishnan and Gaitonde,

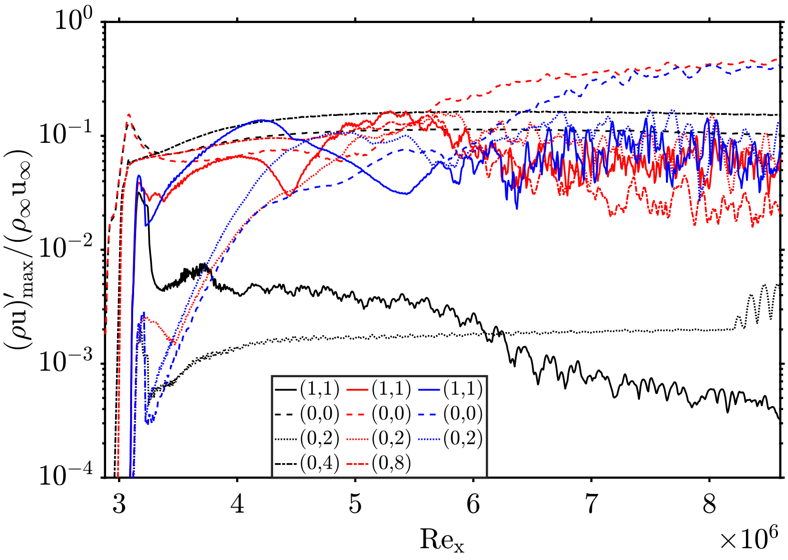

Figure 6.8: Streamwise evolution of maximum modal disturbance amplitudes for A2C4 (black), A2C8 (red), and A_T (blue).

2019). Figure 6.10a illustrates the presence of the GIP near the local boundary-layer edge in the base flow due to a relatively low wall cooling, *i.e.*, $T_w = 0.9 \times T_{rec}$. Without control, the additional two GIPs emerge at $Re_x = 4.5 \times 10^6$ in A_T, as presented in fig. 6.10b, coinciding with the point where the steady mode (0,2) reaches approximately 10% of $\rho_\infty u_\infty$. Subsequently, the profile undergoes significant distortion, with additional GIPs appearing at $Re_x = 5.5 \times 10^6$, marking the onset of the strong non-linear breakdown regime. Introducing streaks with the lowest amplitude at $Re_x = 4 \times 10^6$ has minimal impact on the GIP profile compared to A_T at $Re_x = 4 \times 10^6$, see fig. 6.10c. However, A2C4 generates two additional GIPs in the first half of the boundary layer near the wall at $Re_x = 4 \times 10^6$, despite completely suppressing the fundamental disturbance. These two points disappear further downstream but have higher values in A3C4, at $Re_x = 4 \times 10^6$ in fig. 6.10e, where transition is induced due to the breakdown of the streaks. This suggests that the moderate streak amplitude might have been chosen close to the threshold value of unsuccessful delay. Additionally, streaks do not seem to affect the pre-existing GIP in the base flow near the boundary layer edge unless their amplitude surpasses a certain threshold, causing their instabilities.

6.2.1 Non-linear disturbance formulation

In order to investigate the role of the MFD and the 3-D part of the control streaks separately, a pseudo-disturbance-formulation simulation is employed (Kurz and Kloker, 2016). As illustrated in fig. 6.11, baseflow cases only by activating the control strip are performed. Upon convergence of the flow field at t_1, the conservative variables, stored in

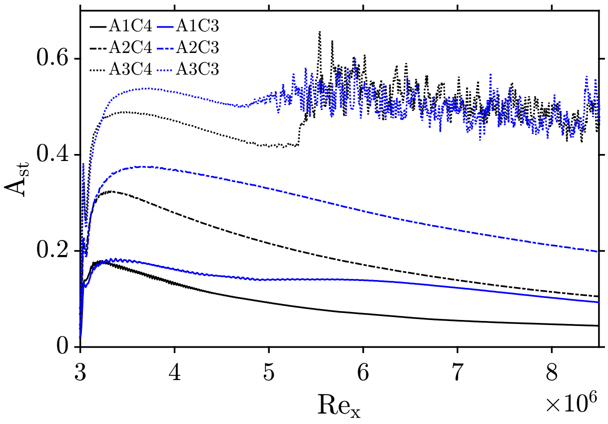

Figure 6.9: Streamwise evolution of the streak amplitude.

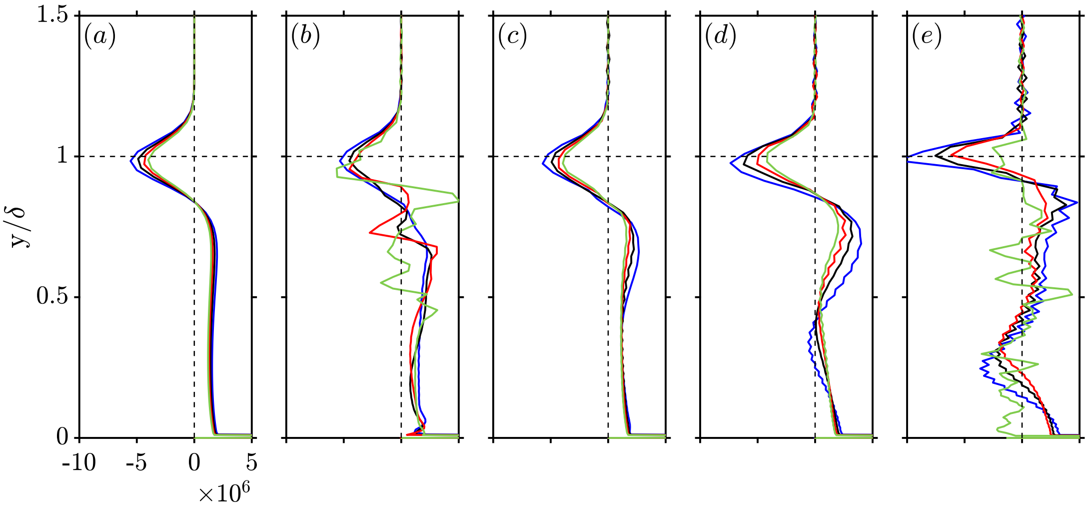

Figure 6.10: GIP distribution for (a) baseflow, (b) A_T, (c) A1C4, (d) A2C4, and (e) A3C4 at $Re_x = 4.0 \times 10^6$ (—), $Re_x = 4.5 \times 10^6$ (—), $Re_x = 5.0 \times 10^6$ (—), and $Re_x = 5.5 \times 10^6$ (—).

$\boldsymbol{Q}$ are averaged in the spanwise direction leaving only the baseflow and the MFD (0,0), referred to as modified-base-flow (MBF). Then, the control strip is deactivated and the flow field is restarted only for one time stepping. The temporal derivative of the conservative variables is calculated at every grid point and subtracted at each time step to keep the modified base flow steady. Subsequently, the perturbation strip is activated and the simulation is run for three flow through. Eventually, Fast Fourier Transformation (FFT) in time and space is performed on the flow field sampled over two fundamental period. The cases employing this pseudo-disturbance formulation is designated by subscript D as shown in table C.2. It is worth noting that the MBF may not fulfill the steady Navier-Stokes equations (Kurz and Kloker, 2016). The adopted procedure is contrary to the method used by Sharma, Shadloo, Hadjadj and Kloker (2019) where the 2-D part of the flow is purged from the flow field leaving only the three-dimensional. The inconvenience of the latter approach is that the turbulence would start to appear and the code may blow up after running for a few fundamental time periods due to the absence of the stabilizing effect provided by (0,0).

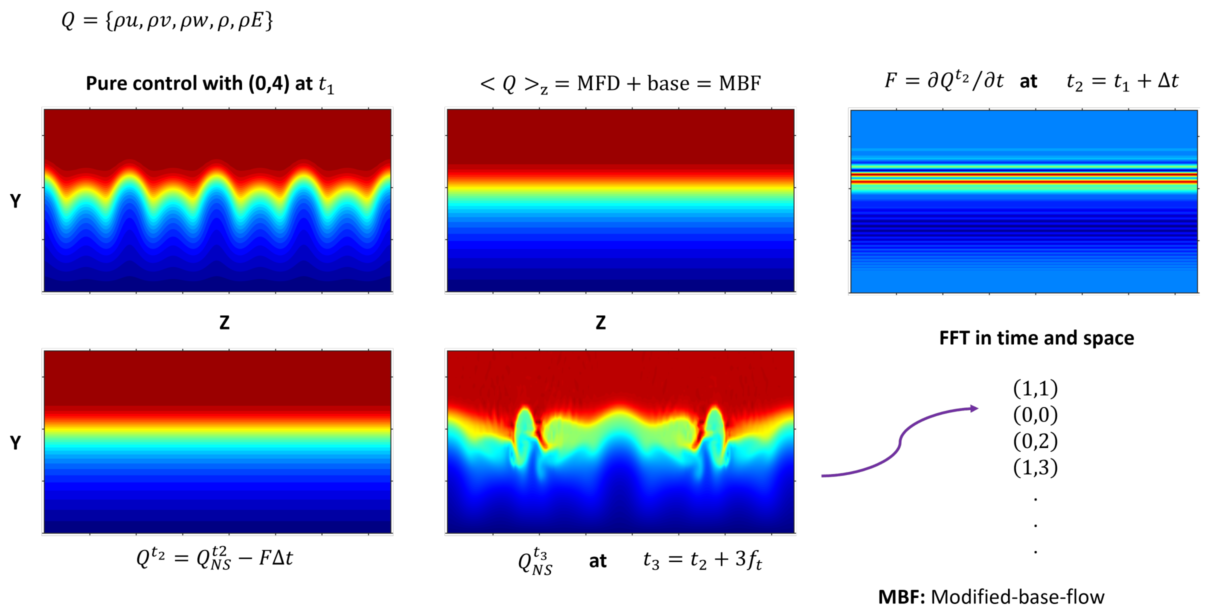

Figure 6.11: Application of nonlinear disturbance formulation.

The implementation of the aforementioned procedure to the adiabatic case (A5C) presents remarkable agreement with the reference, see fig. A.16. The mismatch in the low disturbance amplitude in (1,3) is attributed to the higher background noise of our code as aforementioned in Chapter 3. Following the successful implementation of the pseudo-disturbance formulation, the procedure is applied to our current investigation with control streaks having different spanwise wavenumbers and initial streak amplitudes. A comparison for the full-control (A2C4) is presented in fig. 6.12. Stabilizing effect of the 2-D part of the streaks (MFD) in A2C4$_\mathrm{D}$ decreases the growth rate of (1,1) while yielding a longer amplification distance in the streamwise direction, resulting a higher maximum amplitudes compared to A$_\mathrm{T}$ in the transitional flow regime. Nonetheless, breakdown to turbulence still happens at a comparable streamwise position as in A$_\mathrm{T}$, highlighting the relatively weak stabilizing contribution of the MFD in comparison with the 3-D part of the control streaks. The latter observation can be inferred from comparing the A2C4 and A2C4$_\mathrm{D}$, which conforms with the findings of Paredes et al. (2019) for 2-D Mack mode alongside with Zhou et al. (2023) regarding 3-D Mack mode. It is also seen that purging the 3-D component of the streaks causes a sudden increase in the amplitude of the fundamental mode (1,1) near the perturbation strip. This effect was attributed to localized secondary amplification mechanism induced by the streaks (Kneer, 2020). In addition to the differences in the control streaks nature, findings concerning the contribution of the MFD and 3-D part also differs from the observation at $M_\infty = 2.0$

where stabilizing contribution of the both components was comparable (Sharma, Shadloo, Hadjadj and Kloker, 2019).

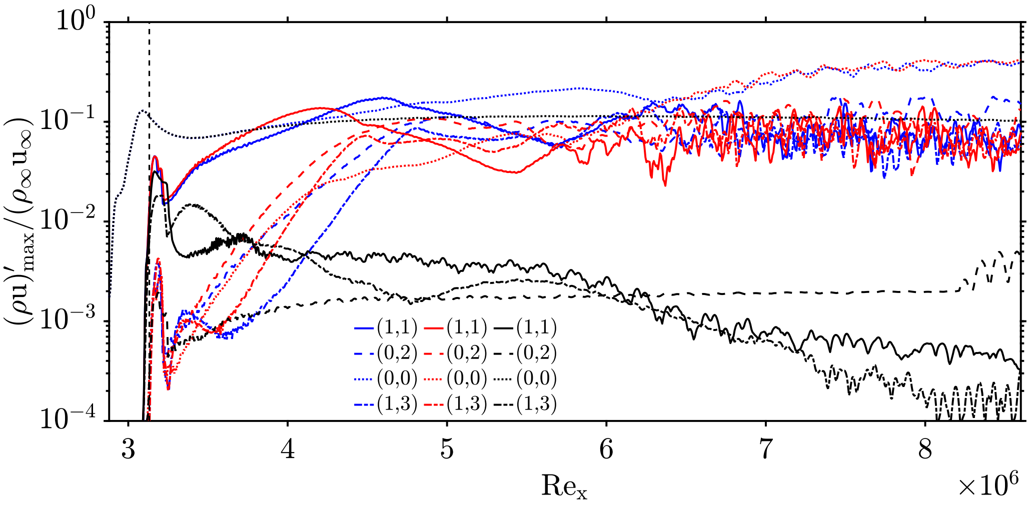

Figure 6.12: Streamwise evolution of maximum modal disturbance amplitudes for A2C4$_\mathrm{D}$ (blue), A2C4 (black), and A$_\mathrm{T}$ (red). Vertical dashed line: perturbation strip center ($Re_x \approx 3.13 \times 10^6$).

A similar analysis is also performed involving the lowest streak amplitude in fig. 6.13. The examination of A1C4$_\mathrm{D}$ indicates somewhat a destabilization of unsteady modes providing the nearly marginal amplified region of the disturbance in A1C4$_\mathrm{D}$ compared to A$_\mathrm{T}$. A similar observation was also made by Zhou et al. (2023) with the identical oblique Mack mode disturbance. The results obtained using the control mode (0,3) are provided in A.17 and A.18, lead to identical outcome regarding the stabilizing role of the MFD and the 3-D part of the control.

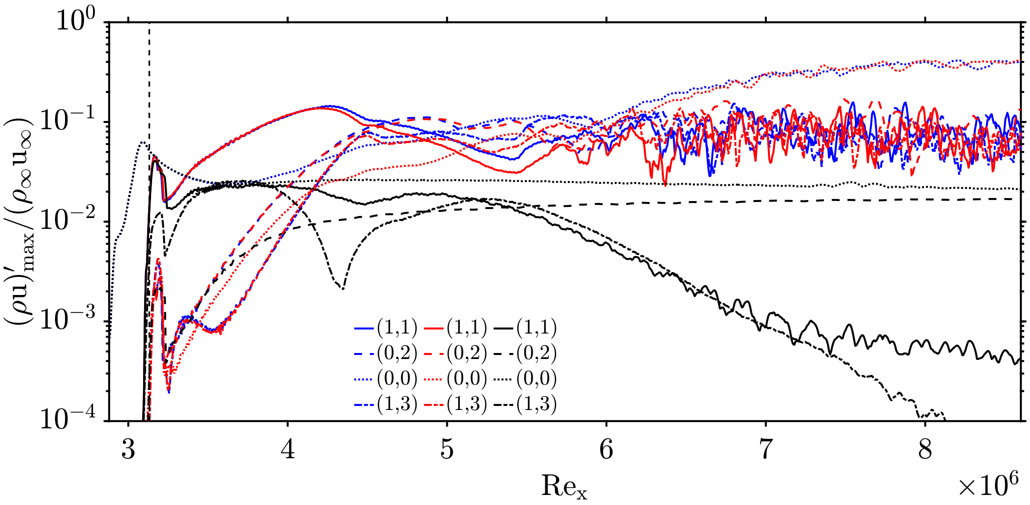

Figure 6.13: Streamwise evolution of maximum modal disturbance amplitudes for A1C4$_\mathrm{D}$ (blue), A1C4 (black), and A$_\mathrm{T}$ (red). Vertical dashed line: perturbation strip center ($Re_x \approx 3.13 \times 10^6$).

6.3 Conclusion

Streaks are employed to control the second-mode disturbance at a low oblique angle, achieving effective suppression of the fundamental disturbance for (0,3) and (0,4) modes with their lowest and moderate initial amplitudes. In contrast to the investigation at Mach 2.0, the initial amplitude is found to be the primary parameter, altering the streamwise evolution of the streaks, in addition to their stability. Notably, the maximum streak amplitude using (0,3) surpasses values reported in existing literature. Subsequently, a non-linear disturbance formulation unveils the near-sole stabilizing effect of the spanwise component of the control modes, with an almost negligible impact of the mean-flow-deformation.

Chapter 7

Conclusions and perspectives

7.1 Conclusions

The objective of this thesis was to advance our comprehension of transitional wall-bounded supersonic and near-hypersonic flows, followed by the implementation of the streak employment method to delay the transition. Initial studies on transition within our research group at CORIA have been ongoing since 2015, focusing initially on bypass transition over flat plates subjected to high wall heating/cooling in supersonic flows. Subsequently, the streak employment method, serving as a passive control technique, was explored, thereby establishing a more specialized branch in the field. The present research was conceived to deepen our understanding of control streaks, encompassing various types of instabilities under different conditions.

In the context of this work, an already existing in-house developed DNS solver has been used to perform simulations. The code uses a hybrid scheme, combining the classical WENO scheme with a locally-conservative sixth-order skew-symmetric split-centered finite-difference scheme for discretizing the convective fluxes. A fourth-order central scheme is utilized for the viscous flux while third-order TVD Runge-Kutta is applied for time integration. The solver remained largely untouched, with only short implementations made for specific purposes. The primary focus has been on the development and improvement of post-processing tools, as well as the conceptualization of the investigation.

Upon successfully validating the LST solver and the DNS code, the efficacy of transition control using narrow-spaced streamwise streaks was examined over flat plates subjected to a low rate of wall heating/cooling at Mach 2.0. This investigation represents a perspective of the preceding doctoral studies and may be regarded as a logical continuation. The parametric study revealed that streaks with a spanwise wavenumber five times that of the fundamental disturbance proved most effective in delaying transition. Cooling the wall enhanced the control method's effectiveness by expanding the range of control amplitude, whereas heating was found to be strongly detrimental *i.e.* 15.8 to 26.5%, 18 to 25.8%, and 20.8 to 25.2% for cooled, adiabatic, and heated flows, respectively. Meanwhile, isothermal wall conditions did not alter the development of the control streaks, indicating no observable changes in the hampering role of the MFD and 3-D part of the control. It is worth mentioning that performed simulations dealt with a forced transition scenario at a single frequency and wavenumber, while transition control in a realistic scenario would be affected by the broadband freestream disturbances (Chang and Malik, 1994; Laible and Fasel, 2016) and modified receptivity due to the introduction of the control devices (Kneer, 2020; Kneer et al., 2022).

DNS in Chapter 4 revealed questionable trends for the Stanton number, nonconforming with the well-established representation in related textbooks, which proposes that cooling walls always produce higher Stanton number values than heating. To address this discrepancy, a comprehensive analysis of high-speed boundary layers subjected to different wall heating/cooling conditions was conducted by employing self-similar solutions to the compressible boundary-layer equations. It is illustrated that the results obtained employing the widely used and accepted but approximative formula for the recovery temperature differ from those obtained by the true adiabatic temperature as obtained by enforcing a zero wall-normal temperature gradient in the solution, may it be a BL or DNS computation. The values of T_{rec} and T_{aw} themselves differ insignificantly, but their difference is largely magnified by calculating the Stanton number for weak to mild wall cooling or heating; the effect gets larger with a higher Mach number. With the true adiabatic value, C_h for cooling should always be larger than for heating, irrespective of the Pr number, no matter whether the wall is heated/cooled at a constant Mach number, or constant T_w/T_∞ is applied at the wall by varying the Mach number. On the other hand, using the approximative T_{rec} brings about a threshold value for the wall heating/cooling rate at a given Mach number, below which the Stanton number for the cooled wall remains lower than that for the heated wall. Additionally, it was shown that T_{rec} alters the Stanton number evolution as a function of Mach number, differing from the typical decaying trend observed in case of T_{aw}. Instead, in case of the first, Stanton number exhibits discontinuities around a Mach number corresponding to the adiabatic condition for any considered curve of $T_w/T_\infty \geq 1$. The Stanton number approaches the discontinuity at the adiabatic condition asymptotically, with the characteristic of this asymptotic behavior strongly dependent on the Prandtl and Mach numbers. Our DNS results for a constant T_w also indicate that C_h becomes highly sensitive around the adiabatic condition. Contrary to the BL solution with T_{aw}, C_h is smaller at lower Mach numbers for cooling, while higher values are obtained at higher Mach numbers for heating. This discrepancy diminishes with increasing boundary-layer thickness downstream. To minimize the possible errors due to the streamwise dependency of C_h, it is suggested to provide the wall heat flux directly for low values of wall heating or cooling, without making it non-dimensional by calculating the sensitive Stanton number.

Control streaks have also been tested at Mach 4.5, near the hypersonic limit, where second mode instability predominates. The designated 3-D disturbance, characterized by low obliqueness, strongly amplifies comparable to its 2-D counterpart. In the absence of transition control, non-linearly generated steady disturbances bear resemblance to the vortical structures observed in the fundamental resonance over differently shaped cones at Mach 6.0 in existing literature. Subsequently, control streaks that have three to five times the wavenumber of the selected 3-D disturbance are employed. Effective suppression of the fundamental disturbance is achieved for (0,3) and (0,4) with their lowest and moderate initial amplitudes, while a further increase in amplitude leads to an earlier transition. It was shown that streaks should have no more than four times the wavenumber of the fundamental disturbance for successful transition delay. Compared to the investigation at Mach 2.0, notable differences are observed in the characteristics of the control streaks. At the lower Mach number, the streaks decay after their generation, regardless of initial amplitude, whereas at Mach 4.5, their amplification depends considerably on the initial amplitude defined at the blowing/suction strip. Ultimately, a non-linear disturbance formulation, excluding the 3-D part of the control and retaining only the baseflow and the MFD, is employed to investigate the mechanism behind effective transition delay. In contrast to the Mach 2.0 findings, where the stabilizing effect of the MFD and the 3-D part of the control were comparable, at Mach 4.5, the stabilizing impact of the MFD on suppressing the 3-D second-mode instability is negligible. The modification in streak characteristics as well as the stabilizing/destabilizing roles of their spatial components requires a thorough analysis involving both types of instabilities simultaneously, as encountered in actual flight scenarios. It should also be emphasized that the performed simulations in the entire research work dealt with a forced transition scenario at a single frequency and wavenumber, while transition control in a realistic scenario would be affected by the broadband freestream disturbances (Chang and Malik, 1994; Laible and Fasel, 2016) and modified receptivity due to the introduction of the control devices (Kneer, 2020; Kneer et al., 2022).

7.2 Perspectives

In the pursuit of contributing to the understanding of transition control, a further venture may be taken up to focus on the following points:

- Streak employment method would be elaborated in the presence of broadband disturbances to more accurately approximate a “natural” transition scenario. As an initial step, a harmonic point source can be utilized to introduce second-mode disturbances with different oblique angles. If successful in delaying transition, first-mode instabilities with a selected frequency might be incorporated using a bi-harmonic point source at a chosen frequency. Ultimately, a multi-frequency mode should be activated to encompass a diverse range of disturbance spectra, that enables to assessment of the effectiveness of the control streaks. This progression can be regarded as a direct continuation of this thesis for which the road has already been paved in Chapter 6.

- The presence of roughness elements in manufacturing is an avoidable factor only to a certain extent, limited by the available technology. Previous control studies have predominantly focused on boundary-layer transition induced by relatively large roughness elements, compared to the local boundary-layer thickness, individual or equidistantly distributed in a certain direction with particular shapes. However, manufacturing processes often result in considerably varied protuberances in terms of shape and spatial distributions. The impact of “randomly” distributed roughness elements, with randomness bounded by specific statistical parameters, could be explored.

- Building upon (Wassermann and Kloker, 2002; Dörr and Kloker, 2018), control streaks might be tested on cross-flow instabilities in supersonic flows. A preliminary analysis conducted using a swept plate, progressing towards more complicated, application-oriented geometries, such as swept wings.

- Practical applications such as an aircraft at high speed mostly require the adaption of a control system to the variations, slight or abrupt, in the environment. For that aim, a dynamic system might be implemented in the solver which serves as a bridge between the control strip and the downstream flow development.

Bibliography

Aeronautics, N. and Administration, S. (2018). **URL:** *https://www.nasa.gov/wp-content/uploads/2018/07/supersonic-flight-recommendations.pdf?emrc=ae77f9* (Cited on page 2).

Alfredsson, P. and Matsubara, M. (2000), Free-stream turbulence, streaky structures and transition in boundary layer flows, *in* 'Fluids 2000 Conference and Exhibit', p. 2534. (Cited on page 12).

Anderson, J. D. (2000), *Hypersonic and high temperature gas dynamics*, Aiaa. (Cited on pages 3, 72, 75 & 83).

Andersson, P., Brandt, L., Bottaro, A. and Henningson, D. S. (2001), 'On the breakdown of boundary layer streaks', *Journal of Fluid Mechanics* **428**, 29–60. (Cited on pages 13, 88 & 89).

Bagheri, S., Fransson, J. H. and Schlatter, P. (2007), 'Research on the interaction between streamwise streaks and Tollmien–Schlichting waves at KTH', *ERCOFTAC Bulletin* **74**, 37–43. (Cited on page 89).

Bagheri, S. and Hanifi, A. (2007), 'The stabilizing effect of streaks on Tollmien-Schlichting and oblique waves: A parametric study', *Physics of fluids* **19**(7), 078103. (Cited on page 13).

Bestek, H., Thumm, A. and Kloker, M. (1994), 'Realistic Numerical Simulation of Boundary-layer Transition Experiments', *Computational Fluid Dynamics' 94* **1**, 463. (Cited on pages 10 & 65).

Bippes, H. (1999), 'Basic experiments on transition in three-dimensional boundary layers dominated by crossflow instability', *Progress in aerospace sciences* **35**(4), 363–412. (Cited on page 13).

Caillaud, C. (2022), High Fidelity Simulation of Hypersonic Boundary Layers Transition to Turbulence. Contribution to the Study of Roughness Effects and Non-Modal Structures, PhD thesis, ISAE-ENSMA Ecole Nationale Supérieure de Mécanique et d'Aérotechique-Poitiers. (Cited on pages 15, 38, 83 & 89).

Celep, M., Hadjadj, A., Shadloo, M., Sharma, S., Yildiz, M. and Kloker, M. (2022), 'Effect of streak employing control of oblique-breakdown in a supersonic boundary layer with weak wall heating/cooling', *Physical Review Fluids* **7**(5), 053904. (Cited on page 50).

Chang, C.-L. and Malik, M. R. (1994), ‘Oblique-mode breakdown and secondary instability in supersonic boundary layers’, *Journal of Fluid Mechanics* **273**, 323–360. (Cited on pages 11, 57, 96 & 97).

Chapman, D. R. and Rubesin, M. W. (1949), ‘Temperature and velocity profiles in the compressible laminar boundary layer with arbitrary distribution of surface temperature’, *Journal of the Aeronautical Sciences* **16**(9), 547–565. (Cited on page 120).

Chaudhuri, A., Hadjadj, A., Chinnayya, A. and Palerm, S. (2011), ‘Numerical study of compressible mixing layers using high-order WENO schemes’, *Journal of Scientific Computing* **47**, 170–197. (Cited on page 28).

Chynoweth, B. C. (2018), Measurements of transition dominated by the second-mode instability at Mach 6, PhD thesis, Purdue University. (Cited on pages 44 & 83).

Cohen, C. B. and Reshotko, E. (1955), Similar solutions for the compressible laminar boundary layer with heat transfer and pressure gradient, Technical report, Lewis Flight Propulsion Research Lab Cleveland, Ohio. (Cited on page 76).

Cossu, C. and Brandt, L. (2002*a*), ‘Stabilization of Tollmien–Schlichting waves by finite amplitude optimal streaks in the blasius boundary layer’, *Physics of Fluids* **14**(8), L57–L60. (Cited on page 13).

Cossu, C. and Brandt, L. (2002*b*), ‘Stabilization of Tollmien–Schlichting waves by finite amplitude optimal streaks in the Blasius boundary layer’, *Physics of Fluids* **14**(8), L57–L60. (Cited on page 89).

Cousteix, T. C. J. (2005), *Modeling and computation of boundary-layer flows*, Springer. (Cited on pages 13 & 62).

Craik, A. D. (1971), ‘Non-linear resonant instability in boundary layers’, *Journal of Fluid Mechanics* **50**(2), 393–413. (Cited on page 10).

Crippa, M., Oreggioni, G., Guizzardi, D., Muntean, M., Schaaf, E., Lo Vullo, E., Solazzo, E., Monforti-Ferrario, F., Olivier, J. G. and Vignati, E. (2019), ‘Fossil CO_2 and GHG emissions of all world countries’, *Publication Office of the European Union: Luxemburg* pp. 1–251. (Cited on page 2).

Crouch, J. (1999), Receptivity issues for laminar-flow control, *in* ‘IUTAM Symposium on Mechanics of Passive and Active Flow Control: Proceedings of the IUTAM Symposium held in Göttingen, Germany, 7–11 September 1998’, Springer, pp. 151–158. (Cited on page 64).

Dörr, P. C. and Kloker, M. J. (2018), ‘Numerical investigations on Tollmien–Schlichting wave attenuation using plasma-actuator vortex generators’, *AIAA Journal* **56**(4), 1305–1309. (Cited on pages 13 & 98).

Duan, L., Beekman, I. and Martin, M. (2010), ‘Direct numerical simulation of hypersonic turbulent boundary layers. Part 2. Effect of wall temperature’, *Journal of Fluid Mechanics* **655**, 419–445. (Cited on page 48).

Duan, L. and Martin, M. (2011), ‘Direct numerical simulation of hypersonic turbulent boundary layers. Part 4. Effect of high enthalpy’, *Journal of Fluid Mechanics* **684**, 25–59. (Cited on page 37).

Ducoin, A., Shadloo, M. S. and Roy, S. (2017), ‘Direct Numerical Simulation of flow instabilities over Savonius style wind turbine blades’, *Renewable energy* **105**, 374–385. (Cited on page 13).

Ducros, F., Ferrand, V., Nicoud, F., Weber, C., Darracq, D., Gacherieu, C. and Poinsot, T. (1999), ‘Large-eddy simulation of the shock/turbulence interaction’, *Journal of Computational Physics* **152**(2), 517–549. (Cited on page 27).

Egorov, I. V. and Novikov, A. V. (2016), ‘Direct numerical simulation of laminar–turbulent flow over a flat plate at hypersonic flow speeds’, *Computational Mathematics and Mathematical Physics* **56**(6), 1048–1064. (Cited on page 11).

Ellingsen, T. and Palm, E. (1975), ‘Stability of linear flow’, *Physics of Fluids* **18**(4), 487–488. (Cited on page 12).

Ermolaev, Y. G., Kosinov, A. and Semionov, N. (1996), Experimental investigation of laminar-turbulent transition process in supersonic boundary layer using controlled disturbances, *in* ‘IUTAM Symposium on Nonlinear Instability and Transition in Three-Dimensional Boundary Layers: Proceedings of the IUTAM Symposium held in Manchester, UK, 17–20 July 1995’, Springer, pp. 17–26. (Cited on page 11).

Exosonic (2024), In *Exosonic*.
URL: *https://exosonic.com/supersonic-jet/* (Cited on page 2).

Fan, Y., Li, W. and Pirozzoli, S. (2019), ‘Decomposition of the mean friction drag in zero-pressure-gradient turbulent boundary layers’, *Physics of Fluids* **31**(8). (Cited on page 43).

Fasel, H., Thumm, A. and Bestek, H. (1993), Direct numerical simulation of transition in supersonic boundary layers: oblique breakdown, *in* ‘Fluids Engineering Conference’, pp. 77–92. (Cited on page 10).

Fedorov, A. (2011), ‘Transition and stability of high-speed boundary layers’, *Annual review of fluid mechanics* **43**, 79–95. (Cited on pages xiii, 6 & 9).

Fezer, A. and Kloker, M. (2000), Spatial direct numerical simulation of transition phenomena in supersonic flat-plate boundary layers, *in* ‘Laminar-Turbulent Transition’, Springer, pp. 415–420. (Cited on page 10).

Fezer, A. and Kloker, M. (2002), Direct Numerical Simulation of Transition Mechanisms at Mach 6.8 on the flat plate and the cone, *in* ‘Proceedings of EuroMech Colloquium Aerodynamics and Thermochemistry of High Speed Flows’, Marseille France, pp. 1–8. (Cited on pages 11 & 12).

Franko, K. J. and Lele, S. K. (2013), ‘Breakdown mechanisms and heat transfer overshoot in hypersonic zero pressure gradient boundary layers’, *Journal of Fluid Mechanics* **730**, 491–532. (Cited on pages 11, 12, 37, 42, 43 & 83).

Fransson, J. H., Brandt, L., Talamelli, A. and Cossu, C. (2005), ‘Experimental study of the stabilization of Tollmien–Schlichting waves by finite amplitude streaks’, *Physics of Fluids* **17**(5), 054110. (Cited on page 13).

Fransson, J. H. and Talamelli, A. (2012), ‘On the generation of steady streamwise streaks in flat-plate boundary layers’, *Journal of fluid mechanics* **698**, 211–234. (Cited on page 89).

Fransson, J. H., Talamelli, A., Brandt, L. and Cossu, C. (2006), ‘Delaying transition to turbulence by a passive mechanism’, *Physical review letters* **96**(6), 064501. (Cited on page 13).

Gill, S. (1951), A process for the step-by-step integration of differential equations in an automatic digital computing machine, *in* ‘Mathematical Proceedings of the Cambridge Philosophical Society’, Vol. 47, Cambridge University Press, pp. 96–108. (Cited on page 28).

Gohd, C. (2020), In *Space.com*.
URL: *https://www.space.com/virgin-galactic-rolls-royce-mach-3-supersonic-aircraft.html* (Cited on page 2).

González, P. P. (2014), Advances in global instability computations: From incompressible to hypersonic flow, PhD thesis, Universidad Politécnica de Madrid. (Cited on pages xix & 116).

Görtler, H. (1940), *Über eine dreidimensionale Instabilität laminarer Grenzschichten an konkaven Wänden*, Vandenhoeck & Ruprecht. (Cited on page 13).

Graver, B., Mukhopadhaya, J., Zheng, X. S., Rutherford, D., Mukhopadhaya, J. and Pronk, E. (2022), 'Aligning Aviation with the Paris Agreement'. (Cited on pages xiii, 2 & 3).

Graver, B., Rutherford, D. and Zheng, S. (2020), 'CO_2 Emissions from Commercial Aviation: 2013, 2018, and 2019'. (Cited on page 2).

Groskopf, G. and Kloker, M. J. (2016), 'Instability and transition mechanisms induced by skewed roughness elements in a high-speed laminar boundary layer', *Journal of Fluid Mechanics* **805**, 262–302. (Cited on page 29).

Groskopf, G., Kloker, M. and Marxen, O. (2008), 'Bi-global secondary stability theory for high-speed boundary-layer flows', *Proceedings of the 2008 Summer Program* (1994), 55–72. (Cited on page 29).

Hader, C. and Fasel, H. F. (2017), Fundamental resonance breakdown for a flared cone at Mach 6, *in* '55th AIAA Aerospace Sciences Meeting', p. 0765. (Cited on pages 44 & 83).

Hader, C. and Fasel, H. F. (2019), 'Direct numerical simulations of hypersonic boundary-layer transition for a flared cone: Fundamental breakdown', *Journal of Fluid Mechanics* **869**, 341–384. (Cited on pages 12, 44 & 83).

Hadjadj, A., Ben-Nasr, O., Shadloo, M. and Chaudhuri, A. (2015), 'Effect of wall temperature in supersonic turbulent boundary layers: A numerical study', *International Journal of Heat and Mass Transfer* **81**, 426–438. (Cited on pages 21 & 47).

Hadjadj, A. and Kudryavtsev, A. (2005), 'Computation and flow visualization in high-speed aerodynamics', *Journal of turbulence* (6), N16. (Cited on pages xviii & 113).

Henrick, A. K., Aslam, T. D. and Powers, J. M. (2005), 'Mapped weighted essentially non-oscillatory schemes: achieving optimal order near critical points', *Journal of Computational Physics* **207**(2), 542–567. (Cited on page 22).

Herbert, T. (1988), 'Secondary instability of boundary layers', *Annual review of fluid mechanics* **20**(1), 487–526. (Cited on page 10).

Hokenson, G. J. (1972), *Hypersonic laminar heat transfer*, Naval Postgraduate School. (Cited on page 75).

Huerre, P. and Monkewitz, P. A. (1985), ‘Absolute and convective instabilities in free shear layers’, *Journal of Fluid Mechanics* **159**, 151–168. (Cited on page 6).

Hunt, J. C., Wray, A. A. and Moin, P. (1988), ‘Eddies, streams, and convergence zones in turbulent flows’, *Studying turbulence using numerical simulation databases, 2. Proceedings of the 1988 summer program* . (Cited on page 65).

Husmeier, F., Mayer, C. and Fasel, H. (2005), Investigation of transition of supersonic boundary layers at Mach 3 using DNS, *in* ‘43rd AIAA Aerospace Sciences Meeting and Exhibit’, p. 95. (Cited on page 10).

Iyer, V. (1995), Computer program BL2D for solving two-dimensional and axisymmetric boundary layers, Technical report, NASA. (Cited on pages xx & 121).

Jameson, A., Schmidt, W. and Turkel, E. (1981), Numerical solution of the Euler equations by finite volume methods using Runge Kutta time stepping schemes, *in* ‘14th fluid and plasma dynamics conference’, p. 1259. (Cited on page 27).

Jiang, G.-S. and Shu, C.-W. (1996), ‘Efficient implementation of weighted ENO schemes’, *Journal of computational physics* **126**(1), 202–228. (Cited on pages 22 & 23).

Jiang, L., Chang, C.-L., Choudhari, M. and Liu, C. (2004), ‘Instability-wave propagation in boundary-layer flows at subsonic through hypersonic Mach numbers’, *Mathematics and Computers in Simulation* **65**(4-5), 469–487. (Cited on pages xiii & 34).

Kachanov, Y. S. (1994), ‘Physical mechanisms of laminar-boundary-layer transition’, *Annual review of fluid mechanics* **26**(1), 411–482. (Cited on page 6).

Kachanov, Y. S. and Levchenko, V. Y. (1984), ‘The resonant interaction of disturbances at laminar-turbulent transition in a boundary layer’, *Journal of Fluid Mechanics* **138**, 209–247. (Cited on page 10).

Kharina, A., MacDonald, T. and Rutherford, D. (2018), Environmental performance of emerging supersonic transport aircraft, ICCT. (Cited on pages xiii & 3).

Klebanoff, P. S., Tidstrom, K. and Sargent, L. (1962), ‘The three-dimensional nature of boundary-layer instability’, *Journal of Fluid Mechanics* **12**(1), 1–34. (Cited on pages 9 & 10).

Kloker, M. (1993), Direkte numerische Simulation des laminar-turbulenten Strömungszuschlages in einer stark verzögerten Grenzschicht, PhD thesis, Fakultat Verfahrenstechnik Universitat Stuttgart. (Cited on page 38).

Kloker, M. J. (2018), ‘Mechanisms of laminar-to-turbulent transition’, *Lecture notes, Institute of Aerodynamics and Gas Dynamics, University of Stuttgart.(Cited on pages viii, 11, 15, 17, 19, 20 & 24)* . (Cited on pages xiii & 8).

Kneer, S., Guo, Z. and Kloker, M. J. (2022), ‘Control of laminar breakdown in a supersonic boundary layer employing streaks’, *Journal of Fluid Mechanics* **932**. (Cited on pages xix, 14, 68, 88, 96, 97 & 118).

Kneer, V. M. S. (2020), ‘Control of laminar breakdown in a supersonic boundary layer employing streaks’, *Master’s thesis (University of Stuttgart, 2020)* . (Cited on pages 14, 52, 62, 92, 96 & 97).

Kosinov, A., Semionov, N., Shevel?kov, S. and Zinin, O. (1994), Experiments on the nonlinear instability of supersonic boundary layers, *in* ‘Nonlinear Instability of Nonparallel Flows: IUTAM Symposium Potsdam, NY, USA July 26–31, 1993’, Springer, pp. 196–205. (Cited on page 11).

Kurz, H. B. and Kloker, M. J. (2016), ‘Mechanisms of flow tripping by discrete roughness elements in a swept-wing boundary layer’, *Journal of Fluid Mechanics* **796**, 158–194. (Cited on pages 90 & 91).

Laible, A. C. and Fasel, H. F. (2016), ‘Continuously forced transient growth in oblique breakdown for supersonic boundary layers’, *Journal of Fluid Mechanics* **804**, 323–350. (Cited on pages 11, 96 & 97).

Landahl, M. (1980), ‘A note on an algebraic instability of inviscid parallel shear flows’, *Journal of Fluid Mechanics* **98**(2), 243–251. (Cited on page 12).

Landahl, M. T. (1975), ‘Wave breakdown and turbulence’, *SIAM Journal on Applied Mathematics* **28**(4), 735–756. (Cited on page 12).

Lee, C. and Chen, S. (2019), ‘Recent progress in the study of transition in the hypersonic boundary layer’, *National Science Review* **6**(1), 155–170. (Cited on page 75).

Lee, C. and Jiang, X. (2019), ‘Flow structures in transitional and turbulent boundary layers’, *Physics of Fluids* **31**(11). (Cited on page 6).

Lees, L. (1947), The stability of the laminar boundary layer in a compressible fluid, Technical report. (Cited on page 8).

Lees, L. and Lin, C.-C. (1946), *Investigation of the stability of the laminar boundary layer in a compressible fluid*, number 1115, National Advisory Committee for Aeronautics. (Cited on page 7).

Leinemann, M., Hader, C. and Fasel, H. F. (2020), Direct Numerical Simulations of the Nonlinear Transition Regime on a Flat Plate at Mach 6, *in* 'AIAA Scitech 2020 Forum', p. 0586. (Cited on page 12).

Li, W., Fan, Y., Modesti, D. and Cheng, C. (2019), 'Decomposition of the mean skin-friction drag in compressible turbulent channel flows', *Journal of Fluid Mechanics* **875**, 101–123. (Cited on page 43).

Lushchik, V. G. and Makarova, M. S. (2016), 'Numerical Investigation of the Effect of the Prandtl Number on the Temperature Recovery and the Reynolds Analogy Factors in the Boundary Layer on a Plate', *High Temperature* **54**, 377–382. (Cited on page 74).

Lysenko, V. I. and Maslov, A. A. (1984), 'The effect of cooling on supersonic boundary-layer stability', *Journal of Fluid Mechanics* **147**, 39–52. (Cited on page 83).

Mack, L. M. (1969), *Boundary-layer stability theory*, Jet Propulsion Laboratory. (Cited on pages 7, 8 & 83).

Mack, L. M. (1984), Boundary-layer linear stability theory, Technical report, California Inst of Tech Pasadena Jet Propulsion Lab. (Cited on pages xiii, 8, 9 & 83).

Maeder, T. (2000), *Numerical investigation of supersonic turbulent boundary layers*, Vol. 394, ETH Zurich. (Cited on page 47).

Malik, M. R. (1989), 'Prediction and control of transition in supersonic and hypersonic boundary layers', *AIAA journal* **27**(11), 1487–1493. (Cited on pages 8, 12 & 83).

Malik, M. R. (1990), 'Numerical methods for hypersonic boundary layer stability', *Journal of computational physics* **86**(2), 376–413. (Cited on pages 30, 31 & 89).

Malik, M. R. (2003), 'Hypersonic flight transition data analysis using parabolized stability equations with chemistry effects', *Journal of Spacecraft and Rockets* **40**(3), 332–344. (Cited on pages 4 & 34).

Martín, M. P., Taylor, E. M., Wu, M. and Weirs, V. G. (2006), 'A bandwidth-optimized WENO scheme for the effective direct numerical simulation of compressible turbulence', *Journal of Computational Physics* **220**(1), 270–289. (Cited on page 22).

Mayer, C. S., Von Terzi, D. A. and Fasel, H. F. (2011), 'Direct numerical simulation of complete transition to turbulence via oblique breakdown at mach 3', *Journal of Fluid Mechanics* **674**, 5–42. (Cited on pages xiii, 11, 33 & 58).

Mayer, C. S., Wernz, S. and Fasel, H. F. (2011), 'Numerical investigation of the nonlinear transition regime in a Mach 2 boundary layer', *Journal of fluid mechanics* **668**, 113–149. (Cited on page 11).

Meersman, J. A., Hader, C. and Fasel, H. F. (2018), Hypersonic boundary-layer transition: comparison of the fundamental resonance breakdown for a flared and straight cone at Mach 6, p. 3851. (Cited on pages 44 & 83).

Morkovin, M. (1994), 'Transition in open flow systems-a reassessment', *Bull. Am. Phys. Soc.* **39**, 1882. (Cited on pages xiii & 6).

Morkovin, M. V. (1969), On the many faces of transition, *in* 'Viscous drag reduction', Springer, pp. 1–31. (Cited on page 6).

Nasr, O. B. (2012), Numerical simulations of supersonic turbulent wall-bounded flows, PhD thesis, INSA de Rouen. (Cited on page 22).

Newbacher, B. (2023), In *FlightGlobal*.
URL: *https://www.nasa.gov/centers-and-facilities/glenn/is-a-mach-4-passenger-jet-possible-nasa-industry-explore-idea/* (Cited on page 2).

Orr, W. M. (1907), The stability or instability of the steady motions of a perfect liquid and of a viscous liquid. Part II: A viscous liquid, *in* 'Proceedings of the Royal Irish Academy. Section A: Mathematical and Physical Sciences', Vol. 27, JSTOR, pp. 69–138. (Cited on page 7).

Oz, F. and Kara, K. (2021), 'A CFD tutorial in Julia: Introduction to compressible laminar boundary-layer flows', *Fluids* **6**(11), 400. (Cited on page 121).

Özgen, S. and Kırcalı, S. A. (2008), 'Linear stability analysis in compressible, flat-plate boundary-layers', *Theoretical and Computational Fluid Dynamics* **22**, 1–20. (Cited on pages xx & 121).

Paredes, P., Choudhari, M. M. and Li, F. (2016*a*), Transition delay in hypersonic boundary layers via optimal perturbations, Technical report. (Cited on pages 14 & 69).

Paredes, P., Choudhari, M. M. and Li, F. (2016*b*), 'Transition due to streamwise streaks in a supersonic flat plate boundary layer', *Physical Review Fluids* **1**(8), 083601. (Cited on pages 14 & 69).

Paredes, P., Choudhari, M. M. and Li, F. (2017), 'Instability wave-streak interactions in a supersonic boundary layer', *Journal of Fluid Mechanics* **831**, 524–553. (Cited on pages 14, 53, 62 & 89).

Paredes, P., Choudhari, M. M. and Li, F. (2019), 'Instability wave–streak interactions in a high Mach number boundary layer at flight conditions', *Journal of fluid mechanics* **858**, 474–499. (Cited on pages xix, 15, 89, 92 & 116).

Passiatore, D. (2021), Simulations numériques directes de couches limites turbulentes hypersoniques avec des effets thermochimiques de non-équilibre, PhD thesis, HESAM Université; Politecnico di Bari. Dipartimento di Ingegneria Meccanica e Gestionale. (Cited on page 37).

Piquet, A. (2017), Physical analysis and numerical simulation of the separation phenomenon in over-expanded nozzle flow, PhD thesis, Normandie Université; Imperial College London. (Cited on page 21).

Pirozzoli, S. (2010), 'Generalized conservative approximations of split convective derivative operators', *Journal of Computational Physics* **229**(19), 7180–7190. (Cited on pages 21, 23, 24 & 26).

Pirozzoli, S. (2011), 'Numerical methods for high-speed flows', *Annual review of fluid mechanics* **43**, 163–194. (Cited on pages xviii, 27 & 113).

Pirozzoli, S., Grasso, F. and Gatski, T. (2004), 'Direct numerical simulation and analysis of a spatially evolving supersonic turbulent boundary layer at $m = 2.25$', *Physics of fluids* **16**(3), 530–545. (Cited on pages 37 & 46).

Poggie, J., Bisek, N. J. and Gosse, R. (2015), 'Resolution effects in compressible, turbulent boundary layer simulations', *Computers & Fluids* **120**, 57–69. (Cited on pages 45 & 47).

Rayleigh, L. (1880), 'On the stability, or instability, of certain fluid motions', *Proc. London Math. Soc.* **9**, 57–70. (Cited on page 7).

Reed, H., Kimmel, R., Schneider, S., Arnal, D., Reed, H., Kimmel, R., Schneider, S. and Arnal, D. (1997), Drag prediction and transition in hypersonic flow, *in* '28th Fluid Dynamics Conference', p. 1818. (Cited on page 4).

Reed, H. L. and Saric, W. S. (1989), 'Stability of three-dimensional boundary layers', *Annual Review of Fluid Mechanics* **21**(1), 235–284. (Cited on page 6).

Ren, J., Fu, S. and Hanifi, A. (2016), 'Stabilization of the hypersonic boundary layer by finite-amplitude streaks', *Physics of Fluids* **28**(2). (Cited on pages 14 & 15).

Renard, N. and Deck, S. (2016), 'A theoretical decomposition of mean skin friction generation into physical phenomena across the boundary layer', *Journal of Fluid Mechanics* **790**, 339–367. (Cited on page 42).

Reshotko, E. (1976), ‘Boundary-layer stability and transition’, *Annual review of fluid mechanics* **8**(1), 311–349. (Cited on page 6).

Reynolds, O. (1901), ‘On the extent and action of the heating surface of steam boilers’, *Papers on Mechanical and Physical subjects* p. 81. (Cited on page 42).

Risen, T. (2019), In *FlightGlobal.*
URL: *https://www.flightglobal.com/airframers/lockheed-martin-adds-momentum-for-supersonic-travel-/133369.article* (Cited on page 1).

Ritchie, H. (2020), In *Our World in Data.*
URL: *https://ourworldindata.org/co2-emissions-from-transport* (Cited on page 2).

Saric, W. S., Carrillo, R. B. and Reibert, M. S. (1998), ‘Nonlinear Stability and Transition in 3-D Boundary Layers’, *Meccanica* **33**, 469–487. (Cited on page 13).

Saric, W. S., Reed, H. L. and Kerschen, E. J. (2002), ‘Boundary-layer receptivity to freestream disturbances’, *Annual review of fluid mechanics* **34**(1), 291–319. (Cited on pages 5 & 6).

Saric, W. S., Reed, H. L. and White, E. B. (2003), ‘Stability and transition of three-dimensional boundary layers’, *Annual review of fluid mechanics* **35**(1), 413–440. (Cited on page 6).

Sayadi, T., Hamman, C. W. and Moin, P. (2013), ‘Direct numerical simulation of complete H-type and K-type transitions with implications for the dynamics of turbulent boundary layers’, *Journal of Fluid Mechanics* **724**, 480–509. (Cited on pages xiii & 10).

Scanlan, A. (2023), In *Our World in Data.*
URL: *https://ourworldindata.org/travel-carbon-footprint* (Cited on page 2).

Scanlan, A. (2024), In *Boomsupersonic.*
URL: *https://boomsupersonic.com/press-release/boom-supersonic-announces-successful-flight-of-xb-1-demonstrator-aircraft* (Cited on page 1).

Schlichting, H. and Gersten, K. (2016), *Boundary-layer theory*, springer. (Cited on pages 61, 75 & 120).

Schmid, P. J. and Henningson, D. S. (2001), *Stability and transition in shear flow*, Springer. (Cited on pages 7, 13 & 30).

Schmidt, O. T. and Rist, U. (2014), ‘Viscid–inviscid pseudo-resonance in streamwise corner flow’, *Journal of fluid mechanics* **743**, 327–357. (Cited on pages 30 & 33).

Schneider, S. P. (1999), ‘Flight data for boundary-layer transition at hypersonic and supersonic speeds’, *Journal of Spacecraft and Rockets* **36**(1), 8–20. (Cited on pages xix & 116).

Schrader, L.-U., Brandt, L. and Zaki, T. A. (2011), ‘Receptivity, instability and breakdown of Görtler flow’, *Journal of Fluid Mechanics* **682**, 362–396. (Cited on page 13).

Schubauer, G. B. and Skramstad, H. K. (1947), ‘Laminar boundary-layer oscillations and stability of laminar flow’, *Journal of the Aeronautical Sciences* **14**(2), 69–78. (Cited on page 7).

Shadloo, M., Hadjadj, A. and Chaudhuri, A. (2014), ‘On the onset of postshock flow instabilities over concave surfaces’, *Physics of Fluids* **26**(7), 076101. (Cited on page 21).

Shadloo, M., Hadjadj, A. and Hussain, F. (2015), ‘Statistical behavior of supersonic turbulent boundary layers with heat transfer at $M_\infty = 2$’, *International Journal of Heat and Fluid Flow* **53**, 113–134. (Cited on page 47).

Shahab, M., Lehnasch, G., Gatski, T. and Comte, P. (2011), ‘Statistical characteristics of an isothermal, supersonic developing boundary layer flow from DNS data’, *Flow, turbulence and combustion* **86**, 369–397. (Cited on page 47).

Shahinfar, S., Sattarzadeh, S. S., Fransson, J. H. and Talamelli, A. (2012), ‘Revival of classical vortex generators now for transition delay’, *Physical review letters* **109**(7), 074501. (Cited on pages 13 & 89).

Shannon, C. E. (1949), ‘Communication in the presence of noise’, *Proceedings of the IRE* **37**(1), 10–21. (Cited on page 38).

Sharma, S. (2019), Laminar-to-turbulent transition in supersonic boundary layer: different scenarios and possible control, PhD thesis, Normandie Université. (Cited on pages xiii & 11).

Sharma, S., Shadloo, M. S. and Hadjadj, A. (2019), ‘Effect of thermo-mechanical nonequilibrium on the onset of transition in supersonic boundary layers’, *Heat and Mass Transfer* **55**(7), 1849–1861. (Cited on page 39).

Sharma, S., Shadloo, M. S., Hadjadj, A. and Kloker, M. J. (2019), ‘Control of oblique-type breakdown in a supersonic boundary layer employing streaks’, *Journal of Fluid Mechanics* **873**, 1072–1089. (Cited on pages 14, 21, 36, 50, 51, 68, 69, 71, 88, 91 & 93).

Shu, C.-W. and Osher, S. (1988), 'Efficient implementation of essentially non-oscillatory shock-capturing schemes', *Journal of computational physics* **77**(2), 439–471. (Cited on pages 21 & 28).

Sivasubramanian, J. and Fasel, H. F. (2014), 'Numerical investigation of the development of three-dimensional wavepackets in a sharp cone boundary layer at Mach 6', *Journal of Fluid Mechanics* **756**, 600–649. (Cited on pages 12 & 83).

Sivasubramanian, J. and Fasel, H. F. (2015), 'Direct numerical simulation of transition in a sharp cone boundary layer at Mach 6: fundamental breakdown', *Journal of Fluid Mechanics* **768**, 175–218. (Cited on pages 12, 44 & 83).

Sivasubramanian, J., Tumin, A. and Fasel, H. F. (2016), The Reynolds number effect on receptivity to a localized disturbance in a hypersonic boundary layer, *in* '8th AIAA Flow Control Conference', p. 4246. (Cited on pages xx & 121).

Sommerfield, A. (1908), 'Ein beitrag zur hydrodynamischen Erklarung der turbulenten Flussigkeisbewegung', *Atti Congr. Int. Math. 4th Rome* . (Cited on page 7).

Spalart, P. R. (1988), 'Direct simulation of a turbulent boundary layer up to R_θ= 1410', *Journal of fluid mechanics* **187**, 61–98. (Cited on page 46).

Stetson, K., Thompson, E., Donaldson, J. and Siler, L. (1989), Laminar boundary layer stability experiments on a cone at Mach 8. V-Tests with a cooled model, *in* '20th Fluid Dynamics, Plasma Dynamics and Lasers Conference', p. 1895. (Cited on page 8).

Supersonic transport (2024), In *Wikipedia.*
URL: *https://en.wikipedia.org/wiki/Supersonic˙transport* (Cited on page 1).

Sutherland, W. (1893), 'LII. The viscosity of gases and molecular force', *The London, Edinburgh, and Dublin Philosophical Magazine and Journal of Science* **36**(223), 507–531. (Cited on pages 20 & 121).

Thumm, A. (1991), Numerische Untersuchungen zum laminar-turbulenten Strömungsumschlag in transsonischen Grenzschichtströmungen, PhD thesis, University of Stuttgart. (Cited on pages 10 & 39).

Tumin, A., Wang, X. and Zhong, X. (2007), 'Direct numerical simulation and the theory of receptivity in a hypersonic boundary layer', *Physics of Fluids* **19**(1). (Cited on pages 33 & 58).

United Nations Climate Change (2024), In *United Nations Climate Change.*
URL: *https://unfccc.int/process-and-meetings/the-paris-agreement* (Cited on page 2).

Unnikrishnan, S. and Gaitonde, D. V. (2019), 'First-mode-induced nonlinear breakdown in a hypersonic boundary layer', *Computers & Fluids* **191**, 104249. (Cited on pages 8, 11, 12, 83 & 89).

Van Driest, E. (1952), Investigation of laminar boundary layer in compressible fluids using the Crocco method, Technical report. (Cited on pages xvi, 72, 73 & 74).

Vance, A. (2016), In *Bloomberg Business*.
URL: *https://www.bloomberg.com/news/articles/2016-03-21/this-aerospace-company-wants-to-bring-supersonic-civilian-travel-back* (Cited on page 1).

Walz, A. (1969), *Boundary layers of flow and temperature*, MIT press. (Cited on page 48).

Wassermann, P. and Kloker, M. (2002), 'Mechanisms and passive control of crossflow-vortex-induced transition in a three-dimensional boundary layer', *Journal of Fluid Mechanics* **456**, 49. (Cited on pages 13 & 98).

White, F. M. and Corfield, I. (2006), *Viscous fluid flow*, Vol. 3, McGraw-Hill New York. (Cited on pages xiii, xv, 4, 5, 41, 61, 72 & 75).

Whitehead, Allen, H. (1989), NASP aerodynamics, *in* 'National Aerospace Plane Conference', p. 5013. (Cited on page 4).

Wiegel, M. (1997), Experimentelle Untersuchung von kontrolliert angeregten dreidimensionalen Wellen in einer Blasius-Grenzschicht, PhD thesis. (Cited on pages xiii & 11).

Zhang, Y.-S., Bi, W.-T., Hussain, F. and She, Z.-S. (2014), 'A generalized Reynolds analogy for compressible wall-bounded turbulent flows', *Journal of Fluid Mechanics* **739**, 392–420. (Cited on page 48).

Zhou, T., Liu, Z., Lu, Y., Wang, Y. and Yan, C. (2022), 'Direct numerical simulation of complete transition to turbulence via first-and second-mode oblique breakdown at a high-speed boundary layer', *Physics of Fluids* **34**(7), 074101. (Cited on pages xiv, xx, 11, 32, 35, 39, 40, 41, 42, 83 & 121).

Zhou, T., Lu, Y., Liu, Z. and Yan, C. (2023), 'Controlling second-mode oblique breakdown in high-speed boundary layers using streak: A direct numerical simulation study', *Physics of Fluids* **35**(8). (Cited on pages 15, 86, 88, 92 & 93).

Zhu, Y., Lee, C., Chen, X., Wu, J., Chen, S. and Gad-el Hak, M. (2018), 'Newly identified principle for aerodynamic heating in hypersonic flows', *Journal of Fluid Mechanics* **855**, 152–180. (Cited on page 42).

Chapter A

Figures

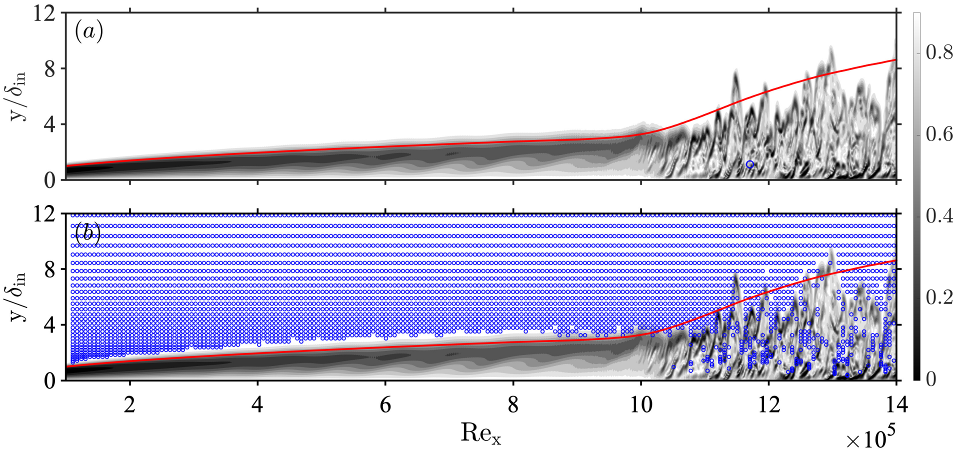

Figure A.1: Impact of the parameter ϵ in equation 2.36 on the Ducros shock sensor for $\mathrm{A_T}$ at $z = L_z/2$ in Chapter 4. (a) $\epsilon = 10^{-5}$ and (b) $\epsilon = (u_\infty/\delta_{in})^2$ as proposed in Pirozzoli (2011). Activated shock sensor locations (symbols) are indicated (a) everywhere and (b) every 4 points in the streamwise and 2 points in the wall-normal directions, respectively. Colorbar is the nonlinearly scaled numerical schileren (Hadjadj and Kudryavtsev, 2005) with the boundary-layer edge marked by the red line.

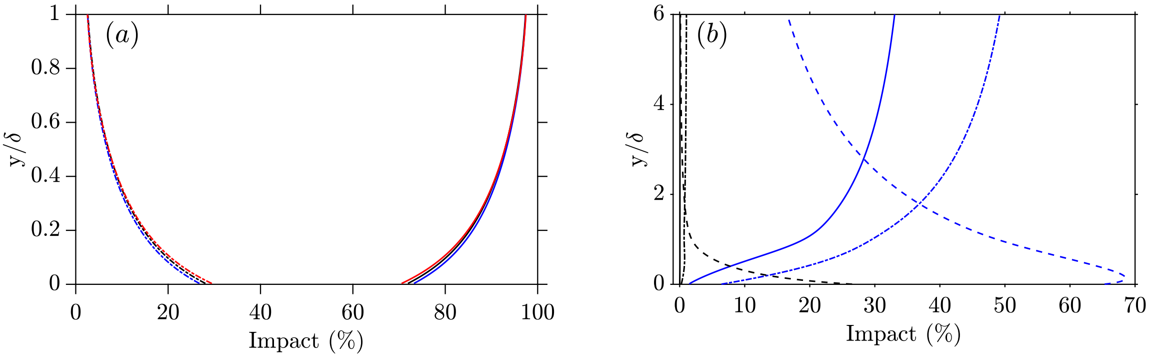

Figure A.2: Impact of the terms in equation 2.43 estimated at $Re_x = 7.1 \times 10^5$. (a) A comparison between the sum of the convective and diffusion times for the cooled wall (blue), adiabatic (black), and heated wall (red) cases with the contribution of the viscous terms (dash-dotted lines). (b) The effect of each term for the cooled wall scenario: $C_{\Delta t,c_1}$ (—), $C_{\Delta t,c_2}$ (--), $C_{\Delta t,c_3}$ (-·-), $C_{\Delta t,v_1}$ (—), $C_{\Delta t,v_2}$ (--), and $C_{\Delta t,v_3}$ (-·-).

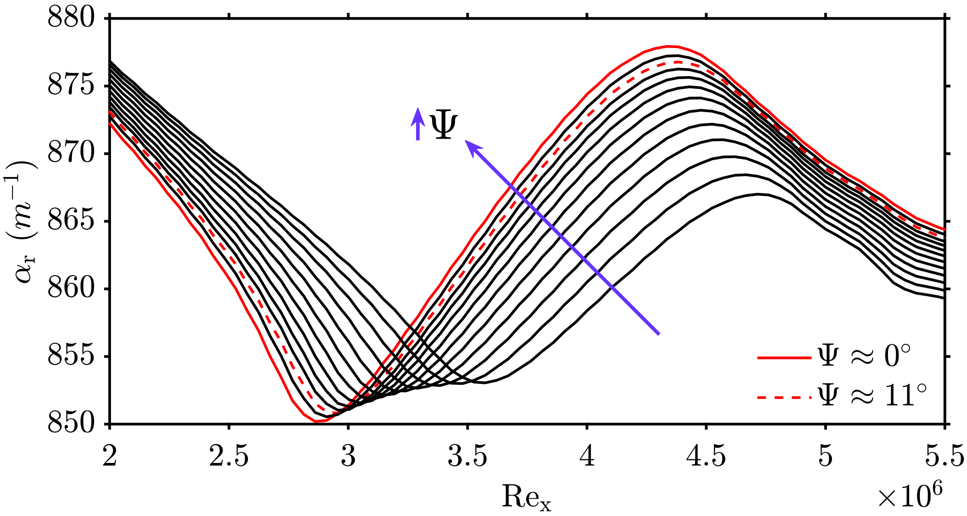

Figure A.3: Evolution of second-mode wavelengths at $f = 91$ kHz, $M_\infty = 4.5$, $T_\infty = 65.15$ K, and $T_w/T_{aw} = 0.9$.

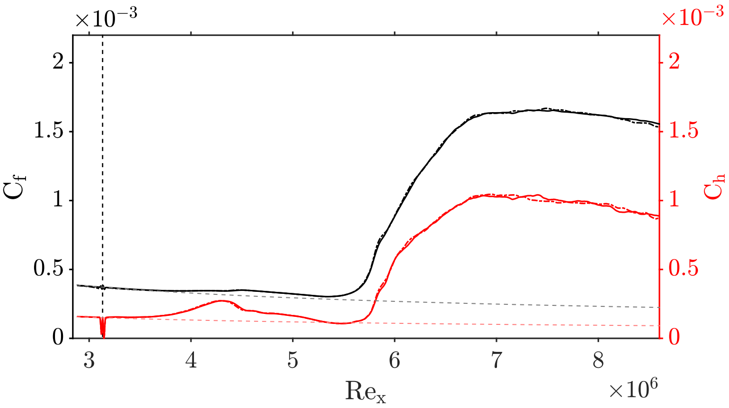

Figure A.4: Streamwise evolution of C_f and C_h in Sv$_{\text{ob}}$ (-·-) and Sm$_{\text{ob}}$ (—) with laminar boundary-layer solutions (dashed lines). Vertical dashed line: perturbation strip center ($Re_x \approx 3.13 \times 10^6$).

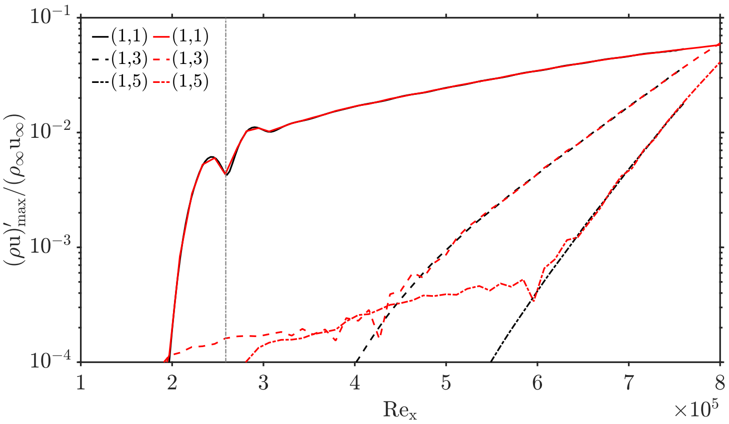

Figure A.5: Streamwise evolution of maximum modal disturbance amplitudes for A_T in Chapter 4. Doubled-streamwise resolution (black). Vertical dashed line: perturbation strip center ($Re_x \approx 2.66 \times 10^5$).

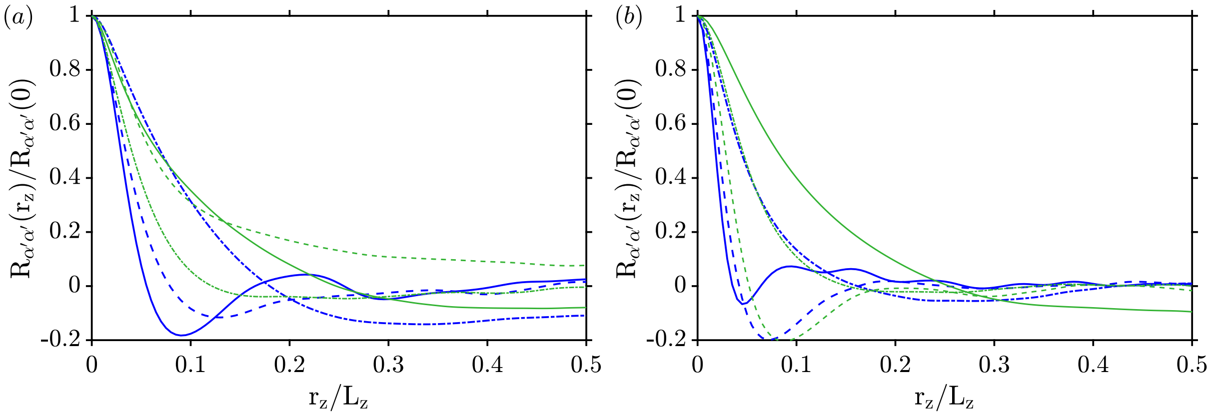

Figure A.6: Distribution of the two-point correlations in the spanwise direction for $\mathrm{Fm_{ob}}$ at $Re_x = 8 \times 10^6$ with (a) $\alpha = u$ (blue) and $\alpha = \rho$ (green) (b) $\alpha = v$ (blue) and $\alpha = w$ (green) at $y^+ = 2.9$ (solid lines), $y^+ = 25.5$ (dashed lines), and $y^+ = 133.3$ (dash-dotted lines).

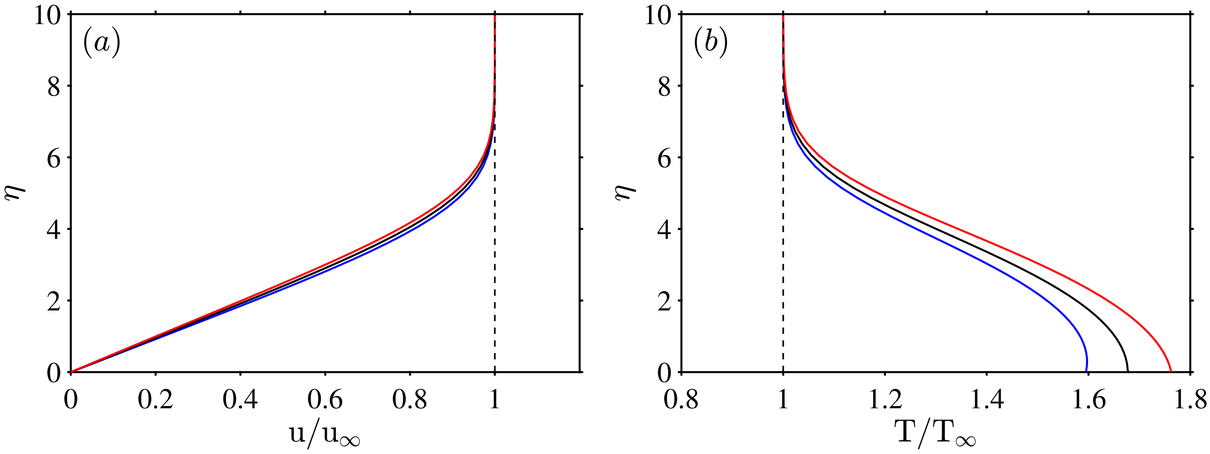

Figure A.7: (a) Velocity and (b) temperature profiles at $Re_x = 10^5$. Cooled (blue), adiabatic (black), and heated (red) cases with $\eta = y\sqrt{\frac{u_\infty}{\nu_\infty x}}$.

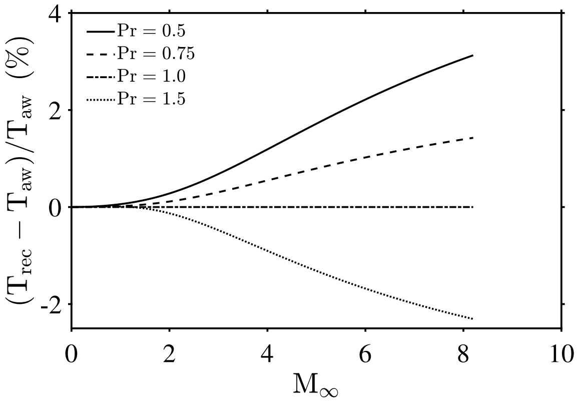

Figure A.8: The effect of Pr number on adiabatic wall temperature.

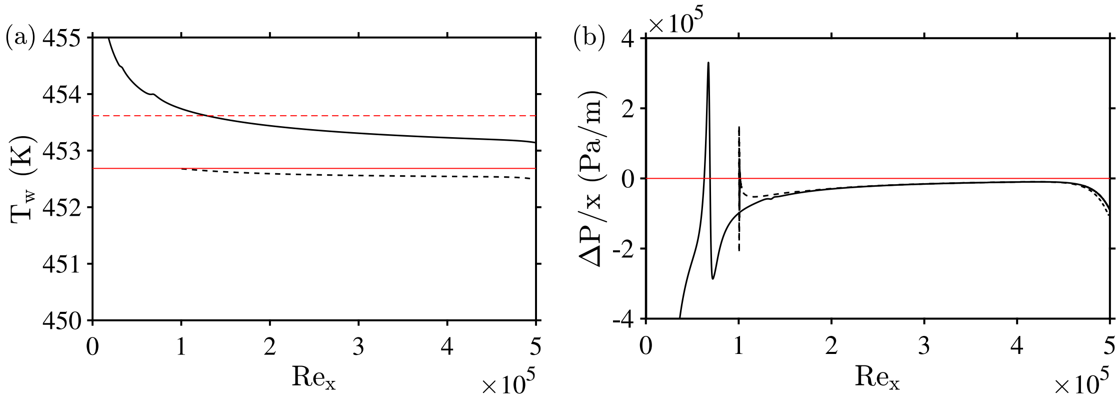

Figure A.9: Streamwise evolution of (a) adiabatic wall temperature and (b) pressure gradient at $y/\delta_{Re_x=10^5} \approx 0.12$ at Mach 2.5. DNS initiated from the leading edge (—) and at $Re_x = 10^5$ (--). BL solution with T_{aw} (—) and T_{rec} (--).

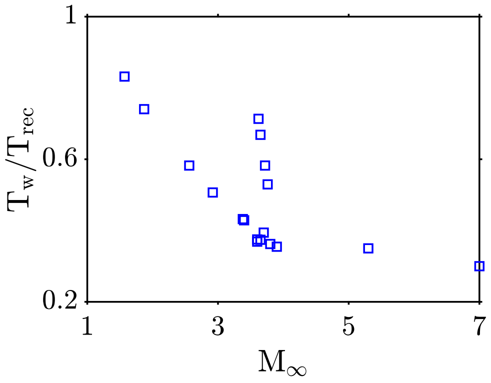

Figure A.10: Flight data (Schneider, 1999; González, 2014; Paredes et al., 2019).

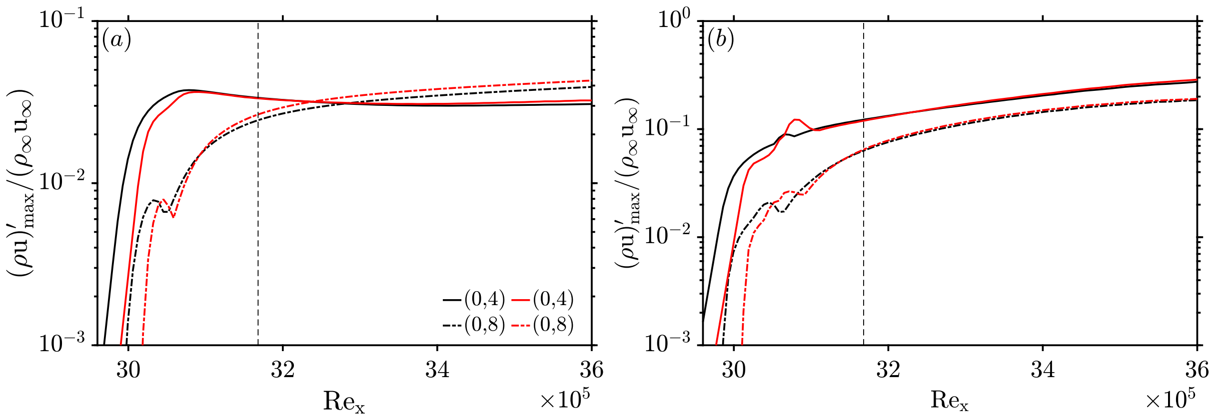

Figure A.11: The evolution of (0,4) and (0,8) with $w_c = 12$ mm (black) and $w_c = 8$ mm (red) for (a) $A_c = 4.95$ % and (b) $A_c = 19.8$ %. Vertical dashed line: perturbation strip end ($Re_x \approx 3.16 \times 10^6$).

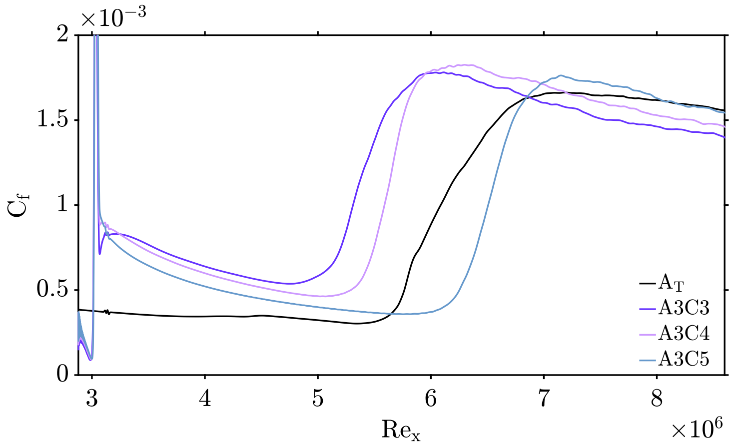

Figure A.12: Streamwise evolution of skin-friction coefficient.

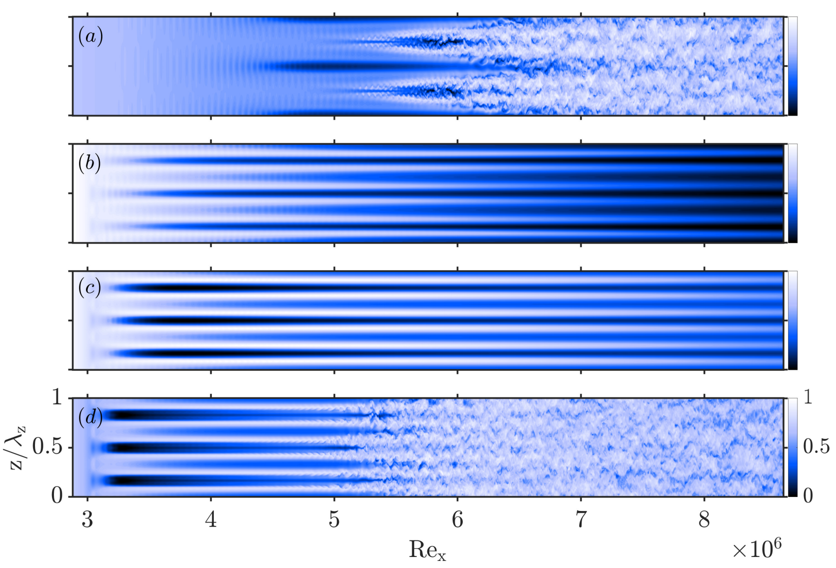

Figure A.13: Contours of $U^* = (u - u_{min})/(u_{max} - u_{min})$ at $y/\delta_{in} = 0.75$ in an instantaneous flow-field for (a) A$_\mathrm{T}$, (b) A1C3, (c) A2C3, and (d) A3C3.

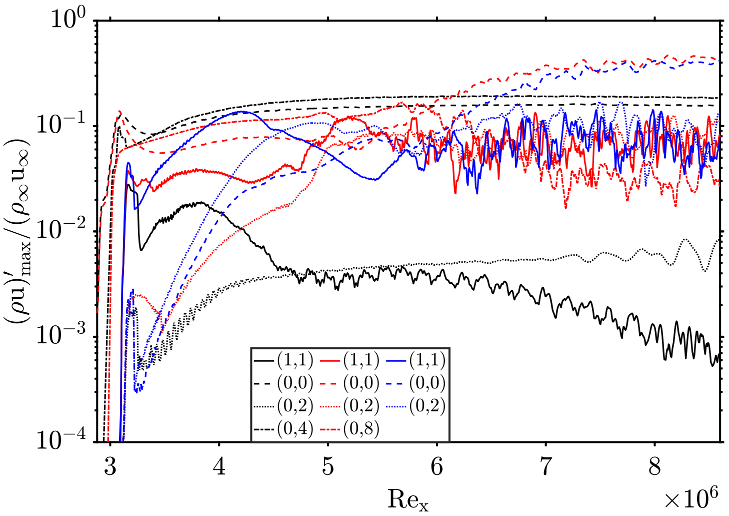

Figure A.14: Streamwise evolution of maximum modal disturbance amplitudes for A2C3 (black), A2C6 (red), and A_T (blue).

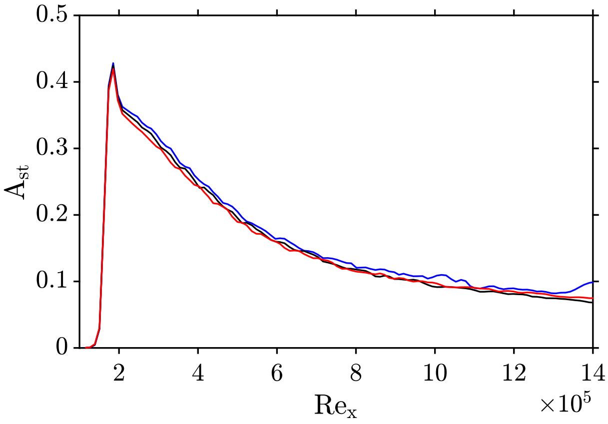

Figure A.15: Streamwise evolution of streak amplitude for C5C (—), A5C (—), and H5C (—) with $A_c/A_{c,ref} = 1.7$ in Chapter 4.

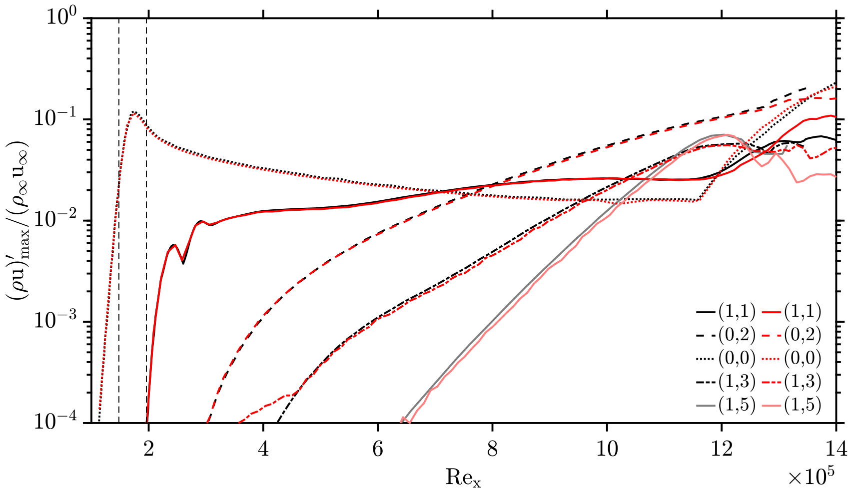

Figure A.16: Streamwise evolution of maximum modal disturbance amplitudes for the role of the MFD at $M_\infty = 2.0$ for case A5C in Chapter 4. DNS implementation (red) and (Kneer et al., 2022) (black). Vertical dashed lines: control strip beginning ($Re_x \approx 1.48 \times 10^5$) and end ($Re_x \approx 1.96 \times 10^5$).

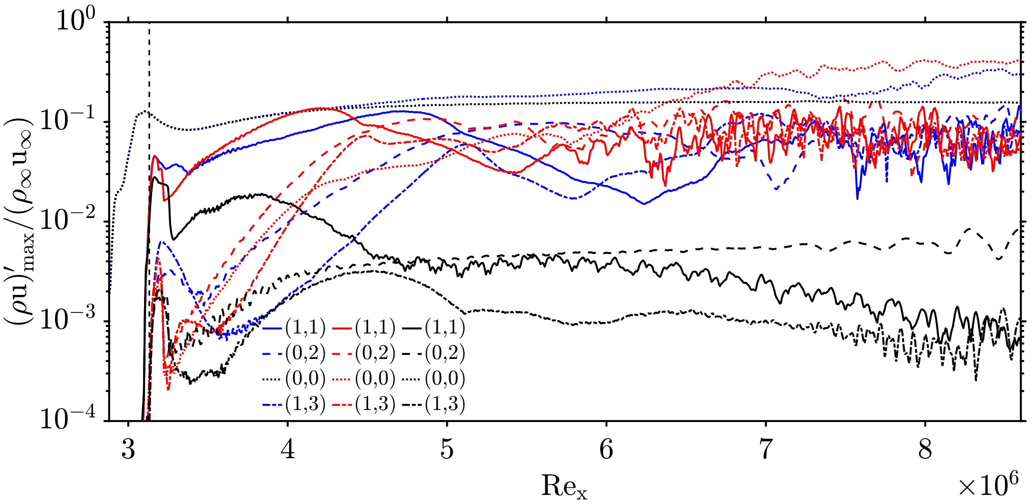

Figure A.17: Streamwise evolution of maximum modal disturbance amplitudes for A2C3$_D$ (blue), A2C3 (black), and A$_T$ (red). Vertical dashed line: perturbation strip center ($Re_x \approx 3.13 \times 10^6$).

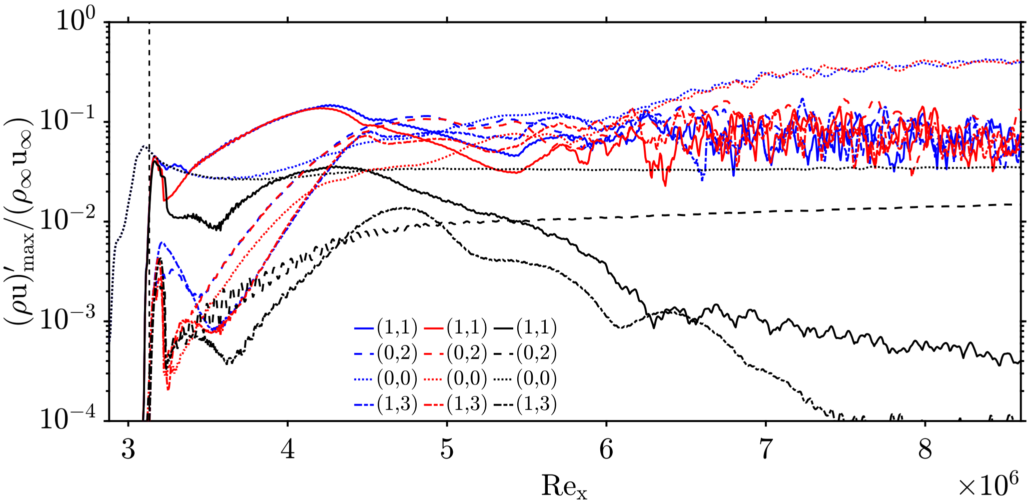

Figure A.18: Streamwise evolution of maximum modal disturbance amplitudes for A2C3$_D$ (blue), A2C3 (black), and A$_T$ (red). Vertical dashed line: perturbation strip center ($Re_x \approx 3.13 \times 10^6$).

Chapter B

Self-similar solutions for compressible boundary layers

Self-similar solutions for laminar flows are obtained by utilizing the steady, two-dimensional compressible boundary-layer equations derived from the compressible Navier-Stokes system. This is done under the assumption of a thin boundary layer and zero-pressure gradient, specifically in the non-low Reynolds-number regime. The complete derivation procedure can be found *e.g.* in Schlichting and Gersten (2016). The variables in the boundary-layer equations can be processed using proper non-dimensional variables, and the resulting system of equations can be written as:

$$(Cf'')' + ff'' = 0, \tag{B.1}$$

$$(Cg')' + Prfg' + CPrM_\infty^2(\gamma-1)f''^2 = 0, \tag{B.2}$$

where

$$g(\eta) = T/T_\infty, \quad f'(\eta) = u/u_\infty, \quad \eta = \sqrt{\frac{u_\infty}{2\mu_\infty\rho_\infty x}}\int_0^y \rho dy. \tag{B.3}$$

Here, Chapman-Rubesin parameter (Chapman and Rubesin, 1949) is designated by $C = (\rho\mu)/(\rho_\infty\mu_\infty)$. Then, the boundary conditions for an adiabatic system are given as follows:

$$\lim_{\eta\to+\infty} f'(\eta) = \lim_{\eta\to+\infty} g(\eta) = 1, \quad f(0) = f'(0) = g'(0) = 0. \tag{B.4}$$

To ensure an isothermal condition with a fixed wall temperature, indicated by T_w, the boundary conditions can be set as:

$$\lim_{\eta\to+\infty} f'(\eta) = \lim_{\eta\to+\infty} g(\eta) = 1, \quad f(0) = f'(0) = 0, \quad g(0) = \frac{T_w}{T_\infty}. \tag{B.5}$$

After the transformation and applying boundary conditions, the final system of eqs. B.1 and B.2 is reduced to a first-order ODE system. This is then solved using the fourth-order Runge-Kutta method in conjunction with Newton's iteration method. For further information regarding the solver, the reader can refer to Oz and Kara (2021).

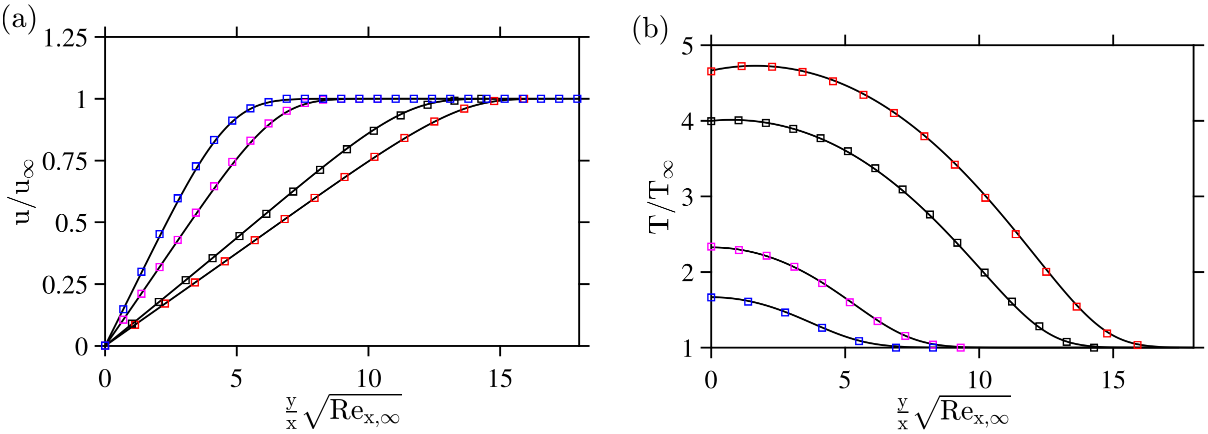

Figure B.1: Comparison of the normalized (a) velocity and (b) temperature distributions across the laminar boundary layer. Self-similar solutions (solid lines), references (symbols): $M_\infty = 5.35$, $Pr = 0.71$, $T_w/T_\infty \approx 4.66$ where $T_\infty = 64.31$ K (□) (Sivasubramanian et al., 2016), $M_\infty = 4.5$, $Pr = 0.72$, $T_w/T_\infty = 4.0$ where $T_\infty = 65.15$ K (□) (Zhou et al., 2022), $M_\infty = 2.8$, $Pr = 0.72$, $T_w/T_\infty = 4.0$ where $T_\infty = 121.11$ K (□) (Iyer, 1995), and $M_\infty = 2.0$, $Pr = Pr(T)$, $(\partial T/\partial y)_w = 0$ where $T_\infty = 288$ K (□) (Özgen and Kırcalı, 2008).

The solver uses identical constant parameters as the DNS code: Pr, $C_p = \gamma\mathcal{R}/(\gamma - 1)$, $\gamma = 1.4$, and $\mathcal{R} = 286.7$ J/(kg.K) where $\mathcal{R}$ is the gas constant for air. For the dynamic viscosity, which varies with temperature, the Sutherland (1893) formula is utilized. The thermal conductivity, λ, is obtained from the viscosity employing the constant Prandtl number. For validating the solver, a wide range of free-stream and boundary conditions has been tested (Sivasubramanian et al., 2016; Zhou et al., 2022; Iyer, 1995; Özgen and Kırcalı, 2008). Figure B.1 presents a comparison of velocity and temperature distributions within the boundary layer at four distinct free-stream Mach numbers. The self-similar solutions are compared to the reference results, revealing a significant level of agreement.

Chapter C

Tables

Table C.1: 2-D DNS cases with the mesh stretching factor κ in eq. 3.1 and $L_y = 1$ (mm).

M_∞	Re_x	N_x	N_y	κ
2.5	$0 - 10^5$	800	180	2.0
2.5	$0 - 10^5$	1600	180	2.0
2.5	$0 - 10^5$	3200	180	2.0
2.5	$0 - 5 \times 10^5$	1600	180	2.0
2.5	$0 - 10^5$	1600	180	2.2
2.5	$0 - 5 \times 10^5$	8000	180	2.2
2.2	$0 - 5 \times 10^5$	8000	180	2.0
2.3	$0 - 5 \times 10^5$	8000	180	2.0
2.35	$0 - 5 \times 10^5$	8000	180	2.0
2.4	$0 - 5 \times 10^5$	8000	180	2.0
2.45	$0 - 5 \times 10^5$	8000	180	2.0
2.5	$0 - 5 \times 10^5$	8000	180	2.0
2.6	$0 - 5 \times 10^5$	8000	180	2.0
2.7	$0 - 5 \times 10^5$	8000	180	2.0
2.8	$0 - 5 \times 10^5$	8000	180	2.0
2.2	$1 - 5 \times 10^5$	6400	180	2.0
2.3	$1 - 5 \times 10^5$	6400	180	2.0
2.35	$1 - 5 \times 10^5$	6400	180	2.0
2.4	$1 - 5 \times 10^5$	6400	180	2.0
2.45	$1 - 5 \times 10^5$	6400	180	2.0
2.5	$1 - 5 \times 10^5$	6400	180	2.0
2.6	$1 - 5 \times 10^5$	6400	180	2.0
2.7	$1 - 5 \times 10^5$	6400	180	2.0
2.8	$1 - 5 \times 10^5$	6400	180	2.0

Table C.2: Parameters for the simulations.

Cases	A_c (% of $\rho_\infty u_\infty$)	Control mode
$\mathrm{A_T}$	–	–
A1C3	1.08	(0,3)
A2C3	2.37	(0,3)
A3C3	4.62	(0,3)
A1C4	1.16	(0,4)
A2C4	2.42	(0,4)
A3C4	4.85	(0,4)
A1C5	1.23	(0,5)
A2C5	2.47	(0,5)
A3C5	4.95	(0,5)
A2C6	2.6	(0,6)
A2C8	2.92	(0,8)
$\mathrm{A1C4_D}$	1.21	(0,4)
$\mathrm{A2C4_D}$	2.42	(0,4)